MECHANICAL RELIABILITY OF THIN BARRIER FILMS FOR FLEXIBLE ELECTRONICS

A Dissertation
Presented to
The Academic Faculty

by

Kyungjin Kim

In Partial Fulfillment
of the Requirements for the Degree
Doctor of Philosophy in the
George W. Woodruff School of Mechanical Engineering

Georgia Institute of Technology
DECEMBER 2018

MECHANICAL RELIABILITY OF THIN BARRIER FILMS FOR FLEXIBLE ELECTRONICS

Approved by:

Dr. Samuel Graham, Co-Chair
(ME/MSE)
School of Mechanical Engineering
Georgia Institute of Technology

Dr. Ting Zhu (ME/MSE)
School of Mechanical Engineering
Georgia Institute of Technology

Dr. Olivier N. Pierron, Co-Chair (ME)
School of Mechanical Engineering
Georgia Institute of Technology

Dr. Mark D. Losego (MSE)
School of Materials Science Engineering
Georgia Institute of Technology

Dr. Suresh K. Sitaraman (ME)
School of Mechanical Engineering
Georgia Institute of Technology

Date Approved: October 26th, 2018

To my family

ACKNOWLEDGEMENTS

First and foremost, I would like to thank my advisors Dr. Samuel Graham and Dr. Olivier Pierron for their constant support, patience, and encouragement to explore new areas of research. You have inspired me to become a better researcher and have always spent the time to solve any obstacles that I encountered throughout my Ph.D. I have gained an enormous amount of knowledge and learned several valuable lessons.

I would also like to extend my sincere thanks to Dr. Ting Zhu, Dr. Suresh Sitaraman and Dr. Mark Losego for serving on my thesis committee. I am grateful for their time taken to carefully review my work and provide me with advice.

I next would like to thank all my friends who made my time here at Georgia Tech more enjoyable and were always available to help me when needed.

Lastly, my family has played an instrumental role throughout my Ph.D. providing me with unlimited support to achieve my goals. I cannot quantify how much thankful I am to my parents, who have ensured my success and provided me with unconditional love.

TABLE OF CONTENTS

LIST OF TABLES

LIST OF FIGURES

NOMENCLATURE

Abbreviations and Chemical formulas

COS	Crack Onset Strain
EAC	Environmentally Assisted Cracking
OPV	Organic Photovoltaics
OLED	Organic Light Emitting Diode
OTR	Oxygen Transmission Rate *(g $m^{-2}day^{-1}$ atm^{-1})*
WVTR	Water Vapor Transmission Rate *(g $m^{-2}day^{-1}$)*
PECVD	Plasma Enhanced Chemical Vapor Deposition
ALD	Atomic Layered Deposition
MLD	Molecular Layered Deposition
FEM	Finite Element Method
SEM	Scanning Electron Microscopy
FIB	Focused Ion Beam
XPS	X-ray Photoelectron Spectroscopy
PET	Poly-Ethylene Terephthalate
PEN	Poly-Ethylene Naphthalate
PI	Polyimide
CTE	Coefficient of Thermal Expansion *(K^{-1})*

Symbols

G	*Driving force / Energy release rate (J m^{-2})*
Γ	*Fracture energy / Critical energy release rate (J m^{-2})*
K	*Stress intensity factor (MPa $m^{1/2}$)*

K_c	*Fracture toughness (MPa $m^{1/2}$)*
S	*Crack spacing (μm)*
v	*Crack growth rate (m s^{-1})*
Z	*Dimensionless energy release rate (-)*
α	*Elastic mismatch (-)*
E	*Modulus of elasticity (-)*
E^*	*Plane strain elastic modulus (-)*
ν	*Poisson's ratio (-)*
σ	*Stress (GPa)*
h	*Thickness (m)*
D	*Diameter (m)*
ε	*Strain (-)*
ρ	*Crack tip radius (m)*
U	*Activation Energy (kJ mol^{-1}/ eV)*
Ω	*Activation volume (cm^3 mol^{-1})*
R	*Gas constant (kJ $K^{-1}mol^{-1}$)*
T	*Absolute temperature (K)*
k	*Boltzmann's constant (J K^{-1})*
ΔA	*Increment of crack surface area (m^2)*
$\delta(y)$	*Crack opening displacement (m)*

Subscripts

c	*Critical*

ss	*Steady-state*
app	*Applied*
res	*Residual*
eff	*Effective*
t	*Time*
f	*Film*
s	*Substrate*
y	*Yield*
a	*Atomic layered deposition layer*
m	*Molecular layered deposition layer*
ac	*Cracked atomic layered deposition layer*
mc	*Cracked molecular layered deposition layer*
i	*Inorganic layer*
o	*Organic layer*
ic	*Cracked inorganic layer*
oc	*Cracked organic layer*

SUMMARY

Flexible electronics such as OLEDs, OPVs are currently under development, especially given their potential low cost and light-weight characteristics. These electronics require packaging technologies that protect them from degradation from environmental factors (e.g., water vapor, oxygen, etc.), while also providing high reliability under mechanical deformation. In this work, mechanical failure under tensile strain has been thoroughly studied to scrutinize the integrity of mechanical reliability in brittle thin barrier films. This is because time dependent deformation can be induced especially in the flexible electronics applications such as bendable or foldable devices which are under applied strain for a period of time. Also, nanolaminates with alternative organic and inorganic layers were fabricated, tested and modeled to produce an optimized crack onset strain. Therefore, the aim of this study is to characterize the mechanical reliability using PECVD SiN_x, and using nanolaminates, ultimately to create mechanically reliable strong barriers.

CHAPTER 1. INTRODUCTION

Flexible electronics have been developed as excellent candidates for next generation devices because of their thin, lightweight features combined with low manufacturing costs, which will enable their widespread use in mobile and wearable applications. These advantages are favorable in applications such as curved, rollable and foldable organic displays, OLEDs, plastic solar cells, and conformal sensors.[3-11] In such applications, not only high efficiency and low cost but also stability and long-term functionality should be ensured. For example, OPV devices must have a lifetime (defined as the point when the initial performance has fallen by 50%) of at least 10,000 hours to be viable in the market.[12-13] Because their flexible substrates consist of thin, organic materials, which are vulnerable to gas permeation,[14-21] such devices are sensitive to permeation by oxygen and water vapor. The ability of oxygen and moisture to cross a barrier that encapsulates the functional area is represented by OTR and WVTR, respectively. It is commonly accepted that the WVTR and OTR required for organic electronics to endure beyond 10,000 hours are about 10^{-6} g·m^{-2}day^{-1} and 10^{-3} g·m^{-2}day^{-1}atm^{-1}, respectively.[22] As shown in Figure 1.1, the upper-limit requirements of WVTR and OTR for organic electronics are about six to eight orders of magnitude lower than the corresponding values of commercially available polymer films, whereas improvement by one to three orders of magnitude is considered sufficient for applications in food and pharmaceutical packaging.[23] To address this shortcoming, ultrathin barrier films consisting of inorganic brittle materials are deposited on organic substrates as barrier layers to protect the functional layer of the device from oxygen and moisture permeation. With the help of

processing methods (PECVD, ALD, etc.) developed to create the ultrabarrier films,[15, 24-28] current ultrathin barrier film technology has reached an effective WVTR of less than 10^{-4} $g \cdot m^{-2} day^{-1}$. [29-32]

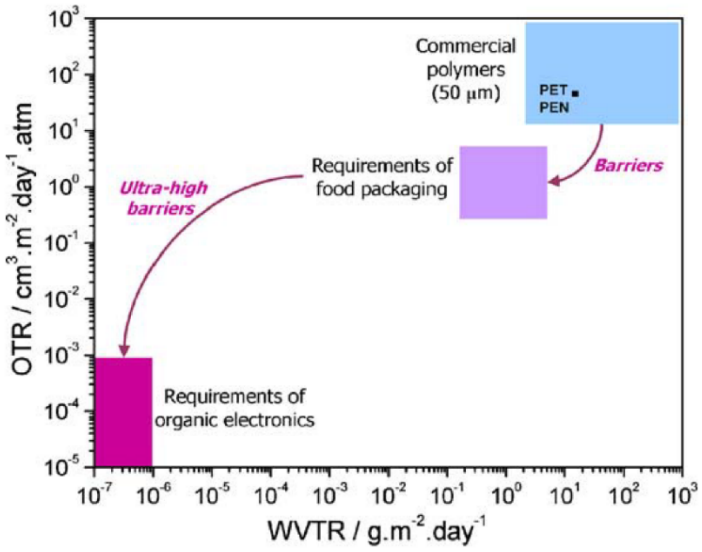

Figure 1.1: OTR and WVTR requirements for encapsulation of organic electronics compared to the values for food packaging of commercial polymer films. [23]

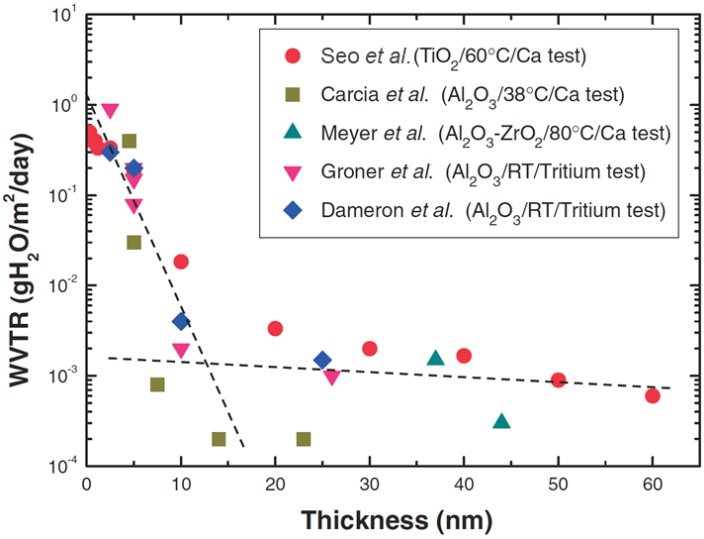

Figure 1.2: Comparison of WVTR as reported in the literature. The information in the legend represents the material/temperature/technique for the measurement. The two dashed lines are linear regressions of WVTR according to film thicknesses less than and over 15 nm, respectively, to determine the critical thickness as represented at the intersection of the two lines.[33]

The effect on WVTR of ultrathin barrier coatings deposited on PET films is shown in Figure 1.2. The thickness range of the ultrathin barrier coatings is at a submicron scale, down to a critical thickness at which the OTR and WVTR change drastically.[24, 33-37] As shown in Figure 1.2, the critical thickness is only about 15 nm. In contrast, even if the thickness of the polymer film increases to above 200 μm, the WVTR is still greater than 1 $g \cdot m^{-2} day^{-1}$.[23] While these barriers have shown excellent performance in applications involving OLEDs and thin film photovoltaics, it should be noted that flexible devices are by design meant to be subjected to deformation, which puts the mechanical reliability of the brittle barrier films into question. The maximum possible applied strains to the thin, brittle barriers are restricted to a few percent (1~3%).[2, 38] Although these brittle barriers cannot be applied to highly stretchable devices, such as tens of percent, a range of few percent can be sufficient for bendable/foldable devices. For example, bending 300μm-thick 10cm-long substrate to a complete circle radius of 1.5 cm requires only 1% of applied strain based on applied bending strain equation $\varepsilon_{app} = h/D$. Often, the mechanical reliability of these films is described in terms of metrics such as the COS, or the number of bending cycles the film can sustain without showing degradation. A typical range of COS in the barrier films and, more importantly, their thickness dependence on COS, *i.e.* higher COS in thinner film, are also shown in the plot of COS as a function of ALD Al_2O_3 films (see Figure 1.3).[38] The fracture mechanics of thin films have previously been studied, including (1) channel cracking (see Fig. 1.4), microcracks, viscous flow, warpage, and plastic deformation under good adhesion with the substrate, and (2) delamination, buckled crack under poor adhesion with the substrate.[39] In particular, channel cracking is the primary

failure mode of the brittle coating layer in flexible devices as the applied strain increases. Thus, this will be considered in the present study.

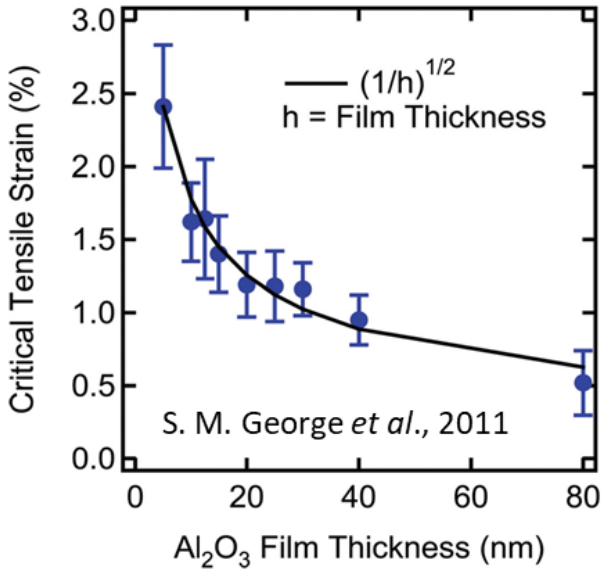

Figure 1.3: COS as a function of the thickness of ALD Al_2O_3 thin film deposited on a polymer substrate.[38]

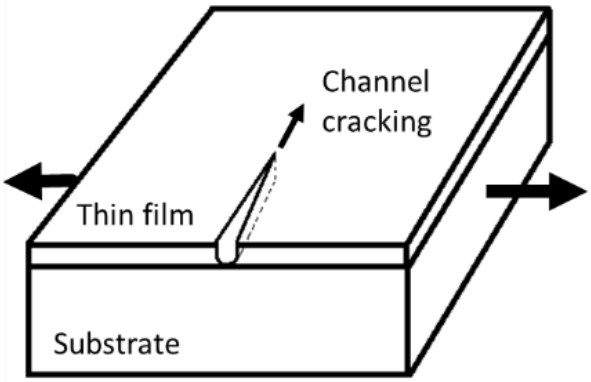

Figure 1.4: Schematic of channel cracking in a thin film on a substrate.

1.1 Research Issues

1.1.1 Subcritical Crack Growth Behavior

Typically, mechanical failure, which limits the reliability of thin brittle films under deformation by stretching or bending, has been described by the concept of COS, i.e. applied strain value that initiates crack propagation.[38, 40-43] However, the COS alone does not govern the mechanical reliability in brittle thin film since time dependent deformation can be induced especially in the flexible electronics applications such as bendable or foldable devices, which are under applied strain over a period of time.

Time dependent cracking in thin films can arise from two sources: 1) viscous deformation behavior of the underlaying substrate and 2) environmental conditions that may lead to EAC or SCC. The former case has been studied by Suo *et al.* by performing computational simulation showing crack growth in elastic film, which does not undergo EAC nor SCC.[44-45] This is because, the viscous underlayer which undergoes creep right below the thin film decreases the constraint at the crack tip, as the stress field relaxes; therefore, an increased driving force that exceeds the critical value leads additional crack extension. Again, the extended crack tip needs some time to get rid of the constraint effect of the underlayer that has not crept yet. This process repeats, and a steady-state crack propagation rate is reached. In the model presented by Suo *et al*., the viscous layer was introduced in between the elastic thin film and an elastic substrate [44-45], but a similar scenario can occur for thin barriers on polymer substrate under tension, because of the viscous properties of polymers. The latter case, *i.e.* EAC or SCC, depends on the source, which results in chemical bond breaking at the crack tip. Including silica, many brittle films have shown environmentally-assisted subcritical crack growth.[46-48] So far, there are few studies that address environmentally assisted crack growth behavior of silicon nitride (SiN_x) films.[49-51] In contrast with bulk Si_3N_4 ceramics, which are found to be immune to EAC,

recent works by Vellinga *et al.* [49] and Guan *et al.* [50] showed subcritical crack growth in SiN_x barrier films on PEN substrates caused by humidity in the surroundings using in-situ microscopy resistance measurements.

However, it is not clear, if the time dependent fracture behavior of brittle films on polymer substrates come from the relaxation of polymer substrate or EAC in SiN_x. In addition, the variation of crack growth rates as a function of driving force for channel cracking still must be investigated to understand the reliability in terms of fracture kinetics and energetics versus a simple parameter such as COS. Therefore, the aim of this study is to elucidate the origin of subcritical cracking in SiN_x barriers on polymer substrate by measuring the crack growth rate as a function of driving force along with presenting numerical models to differentiate the contribution of polymer relaxation from that of EAC. Environmental factors which can be responsible for variable crack growth rates under same amount of driving forces are moisture (or humidity), oxygen, and temperature. A simple method, which can perform crack growth rate measurements in controlled environments, is in-situ microscopy visualization combined with microtensile testing. Additionally, this method will be further developed to measure crack growth rate in an efficient way, therefore creating a standard testing method for future repeatable work, which can be applied to all thin film materials that undergo subcritical cracking.

1.1.2 Long-term Time Dependent Subcritical Cracking Behavior

Since flexible devices are under stress from their flexed state of strain, long term reliability should be examined, and resultant mechanical failure behaviors need to be investigated for proper and reliable operation of the devices. The crack growth rates

showed fluctuation after a certain period of time (0.5 ~ 1 hour), denoting the possibility of additional mechanical failures other than channel cracking in barriers. SEM was performed to confirm the crack configurations of the specimens after the tests. The specimen tested under subcritical value of COS for a short period of time (< 0.5 hour) was observed to have only channel cracks in the thin films (see Figure 1.5 (a)), which validates the channel crack equation used for an isolated crack whose front width corresponds to the film thickness. In the case of specimen tested also under the subcritical value of COS for a long period of time (> 100 hours), depth of the propagated crack in barrier layer exceeds its thickness, showing crack penetration into the polymer substrate, so called substrate cracking (see Figure 1.5 (b)).

In the previous works done by Tada *et al*. and Thouless *et al*., the effect of substrate cracking in growing crack has been shown to increase the driving force for crack propagation.[52-54] Basically, higher applied strains produce deeper depth of substrate cracking and thus an equation of driving force is built up to be the function of substrate cracking depth. However, the influence of substrate cracking on long-term transient cracking behavior has not been studied. Here the 'long term' means an extended period of time over a few days, which allows the prediction of the patterns of damage growth in barrier films under flexible deformation. Specifically, the long-term crack growth rate behavior can be collected and further analyzed to show crack configurations, single and multiple crack growth rates. Therefore, the goal of this study is to understand the physics behind the various scenarios of increasing, decreasing or constant crack velocities depending on the substrate cracking configuration and spacing to surrounding adjacent neighboring cracks.

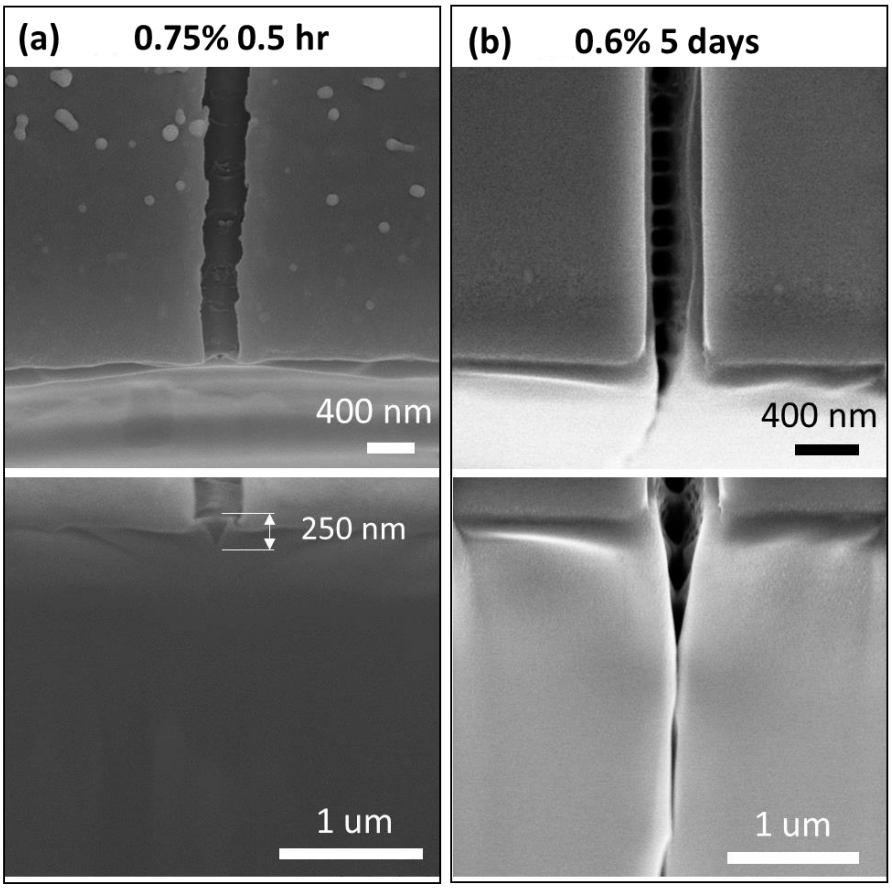

Figure 1.5: SEM images of FIB cut SiN_x / PET at the location of channel cracks, (a) strained at 0.75% of applied strain for 0.5 hour and (b) strained at 0.6% of applied strain for 5 days.

1.1.3 Protection from Both Moisture Permeation and Crack Propagation

Barrier coatings applied to encapsulate the flexible electronics devices from vapor permeation must also withstand applied strains without forming cracks. As mentioned in the beginning of introduction, substrates for flexible electronics devices are polymers while inorganic semiconductor devices consist of stiff materials as substrates such as silicon. Therefore, the driving force for crack propagation in flexible devices becomes much larger than that of microelectronics devices since mechanical constraint holding crack opening displacement substantially reduces when the substrate changes from stiff materials to

compliant materials, with everything else being equal. In most barrier coatings on polymer substrates, mechanical failures as the applied tensile strain increases start with cohesive crack propagation in the lowest fracture energy contained layer.[41, 43, 55] After the density of cohesive cracks increases until the crack spacing reaches a saturated value, the brittle thin film buckles and delaminates from the substrate.[41, 43] Consequently, for the thin film materials, which do not undergo time dependent subcritical crack growth, the primary failure mechanism can simply be defined by COS, where cohesive channel crack starts to propagate, because it begins to compromise the vapor permeation resistance of barriers.

Multilayer barriers consisting of alternating organic and inorganic layer have been suggested to be a smart method for optimizing barrier performance by producing both high COS[55-56] and high resistance to gas permeation.[22, 57-59] This is attributed to the favorable mechanical properties of organic films, *i.e.*, consisting of high COS, and favorable mass transport properties of inorganic films, *i.e.*, consisting of high resistance to gas permeation, respectively. In addition, the multilayer structure can generate a tortuous route for vapor or gas permeation potentially leading to an increased lag time effect before permeation is reached to the functional layer. To optimize the COS in multilayer barrier structures, along with the materials properties of both organic and inorganic films, the thickness of each layer becomes key factor. When the organic layer is introduced at the interface between inorganic layers, a thin organic layer cannot stop the crack propagation across the organic / inorganic interfaces, and one that is too thick removes the constraint between the two inorganic layers and therefore the channel cracks can readily form in either inorganic layer. However, there should be an optimal thickness of the inorganic / organic layers that enable a maximum in COS for the system.

Theoretical predictions made by Cordero *et al*.[55] and Rong *et al*.[56] provides basic guideline of selecting organic / inorganic layer based on material properties and designing geometry of structure, i.e. thickness and order of layers. Experimental work performed by Miller *et al.* used 3-layer nanolaminates consisting of Al_2O_3 grown by ALD and alucone grown by MLD.[41] However, the COS was not improved due to the low fracture energy of MLD alucone layer (0.8 J/m^2 compared to that of 18.6 J/m^2 in ALD Al_2O_3 layer).[41] Therefore, the aim of this study is to utilize a high fracture energy contained organic layer in a multilayer architecture to make the experimental confirmation on improved COS, guided by the numerical analysis.

1.2 Background

1.2.1 Mechanics of Thin Film

Channel cracking in brittle thin film: crack formations in brittle coatings under tensile stress / strain are described by channel cracking. The driving force for channel crack propagation, i.e. energy release rate, *G*, is given by[39]

$$G_{ss} = \frac{Z\sigma^2 h_f}{E_f^*} = \frac{Z\left(\sigma_{app} + \sigma_{res}\right)^2 h_f}{E_f^*} = ZE_f^*\left(\varepsilon_{app} + \varepsilon_{res}\right)^2 h_f \qquad (1)$$

where σ, σ_{app} and σ_{res} are the total, applied and residual stress in the film, respectively. ε_{app} and ε_{res} are the applied and residual strains in the film, E_f^* and h_f are the plane strain elastic modulus and thickness of the film, and Z is the dimensionless energy release rate which depends on the elastic mismatch, α, between the film and substrate:[60]

$$\alpha = \frac{E_f^* - E_s^*}{E_f^* + E_s^*} \tag{2}$$

where E_s^* is the plane strain substrate elastic modulus. Numerical models provide the value of Z as a function of α. It has shown that the Z is a strong function of the elastic mismatch between film and substrate.[60-62] For example, an order of magnitude larger driving force occurs in stiff films / compliant substrates arrangements (α = 0.95) than the opposite arrangements (α = 0.1) (see Figure 1.6).

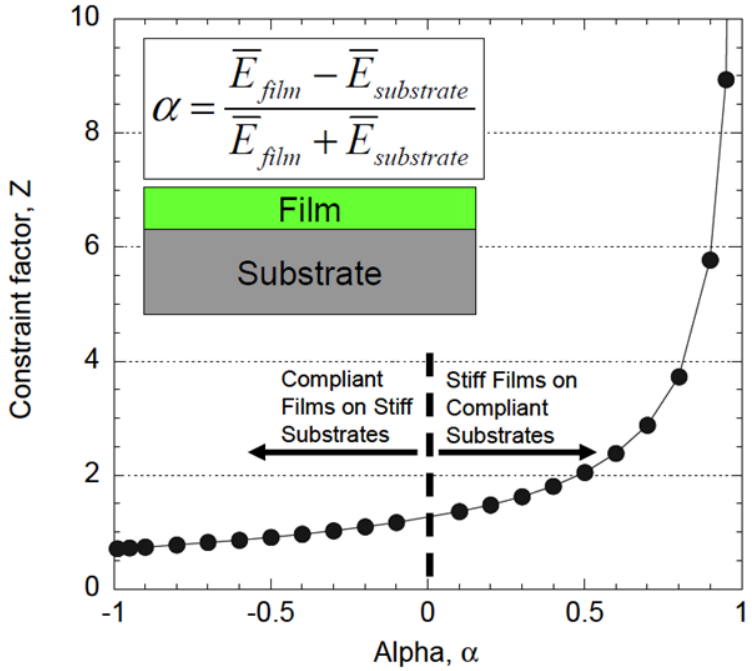

Figure 1.6: Z as a function of elastic mismatch α. [63]

Stress intensity factor, K, of the crack can be obtained by the following relationship with the energy release rate, G_{ss}:[64]

$$K = \sqrt{G_{ss} E_f^*} \tag{3}$$

It should be noted that the Eq. 1 assumes linear elastic behavior for both film and substrate, and is applicable to a crack configuration of a single and isolated crack, where the crack tip placed at the interface between film and semi-infinite substrate.[39] This equation can be modified for the case of multiple cracks, thinner substrates, delamination and buckled cracks.[61-62, 65] It can also be modified for the case of substrate cracking and plastic deformation of the film and/or substrate.[52-53]

Activation energy calculation for thin film undergoing EAC: The EAC curve contains subcritical crack growth regions placed between a threshold and a critical fracture energy. The region below the threshold, where crack growth is arrested may be present if the stress-enabled chemical reaction is not energetically favorable at driving forces below this value or steric hindrance effects prevent the reactive environmental species reaching to the strained bonds at crack tip. The driving force above the critical fracture energy generates cracking independent of the chemical environment, although temperature can still influence as the yield properties and extend of plasticity may be affected. The subcritical crack growth regions can be classified into a reaction-controlled region and transport-controlled region depending on the reaction rate, mobility and concentration of the reactive species, as well as temperature (see Figure 1.7).[51, 66] For the former region, the growth rates are represented as a function of applied driving force. The latter region where the kinetics are controlled by diffusion of the reactive species to the crack tip shows growth rates insensitive to the applied driving force, because of the high chemical reaction rate.

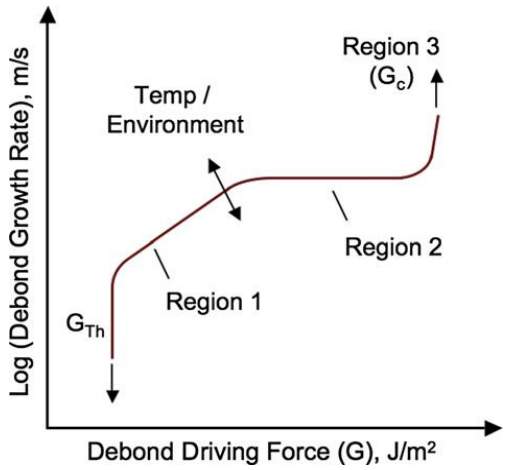

Figure 1.7: A schematic of an EAC curve illustrating different rate-controlled regions.[51]

Atomistic models have been presented to describe the reaction and transport-controlled regions in environmentally assisted cracking along with the threshold value.[47-48, 67-68] Net crack growth / debond velocity is a summation of the rate of bond rupture and bond healing at crack tip since the crack growth is not considered to be a completely thermodynamically reversible process:

$$v = v_0 a_x \left(\exp\left[-\frac{U_+(G)}{k \cdot T} \right] - \exp\left[-\frac{U_-(G)}{k \cdot T} \right] \right) \tag{4}$$

where v_o corresponds to the lattices vibration frequency (~$k \cdot T/h$), a_x is the distance which the crack advances by one atomic spacing, T is the absolute temperature, k is Boltzmann's constant, and $U_+(G)$ and $U_-(G)$ correspond to the activation energy for kink advancement and healing, respectively. When describing behavior in the region away from the threshold (where $U_-(G) - k \cdot T > U_+(G)$), the second exponential term can be neglected as the first term will dominate the growth rate. In the same sense, the reaction controlled region for most glass systems can be modeled by [69]

$$v = a \exp\left[\frac{-U_{+}(G) + bK}{R \cdot T}\right] \quad (5)$$

where R is the gas constant, T is the absolute temperature, K is the applied stress intensity, and a and b are constants used to fit the relationship to measured data. The slope b obtained from the fit directly proportional to the activation volume of reaction expressed by[69]

$$\Omega = \frac{b}{2}\sqrt{\pi\rho} \quad (6)$$

where ρ is the crack tip radius (usually ~0.5 nm for glass). The activation volume is a representation of change in molecular dimensions as the reaction undergoes an activated transition state prior to bond rupture. A larger activation volume suggests a greater extent of crack tip bond stretching before failure of the bond.

Fracture energy in multilayer thin film: The driving force initiating the channel crack propagation can be written by following criterion from thin film fracture mechanics:[64]

$$G\Delta A \geq \Gamma \Delta A \quad (7)$$

where driving force, G, is the energy release rate as explained in the previous section, the reduction of elastic energy stored in the film per unit increase in the crack surface area, Γ is the average fracture energy, and ΔA denotes an increment in the crack surface area. The energy release rate G depends on the applied tensile strain as well as the geometry and mechanical properties of the composite layers, while Γ is a material parameter. For steady-state crack propagation, the driving force G assuming linear elasticity can be calculated by

comparing the elastic energy stored in a slice of material far ahead the crack tip where the film remains intact and far behind the crack tip where the film is opened:

$$G = \frac{1}{2h_c}\int_0^h \sigma(y)\delta(y)dy \tag{8}$$

where y is a coordinate along the thickness direction of the film, $\sigma(y)$ is the tensile stress far ahead of the crack tip, i.e. multiplication of plane strain elastic modulus and applied strain of the layer, and $\delta(y)$ is the crack opening displacement of the film far behind the crack tip (see Fig. 2). Here, crack opening displacement, $\delta(y)$, can be calculated using a plane strain model in FEM software such as ABAQUS. [70]

The COS, ε_c, can be determined after obtaining the dimensionless energy release rate Z from finite element results by combining eq. 7 and eq. 8:

$$\varepsilon_c = \sqrt{\frac{\Gamma}{E_a^* h_a Z}} \tag{9}$$

For composite films, the average fracture energy Γ depends on which layers are subjected to crack propagation:

$$\Gamma = (\Gamma_a h_{ac} + \Gamma_m h_{mc}) / h_c \tag{10}$$

where Γ_a and Γ_m are fracture energy of ALD layers and MLD layers, examples of inorganic and organic films, respectively. h_{ac} and h_{mc} are the total thickness of cracked ALD layers and cracked MLD layers, respectively. Finally, the normalized COS can be derived by

$$\bar{\varepsilon}_c = \varepsilon_c \sqrt{\frac{E_a^* h_a}{\Gamma_a}} = \sqrt{\frac{1}{Z}\left(\frac{h_{ac}}{h_c} + \frac{\Gamma_m h_{mc}}{\Gamma_a h_c}\right)} \tag{11}$$

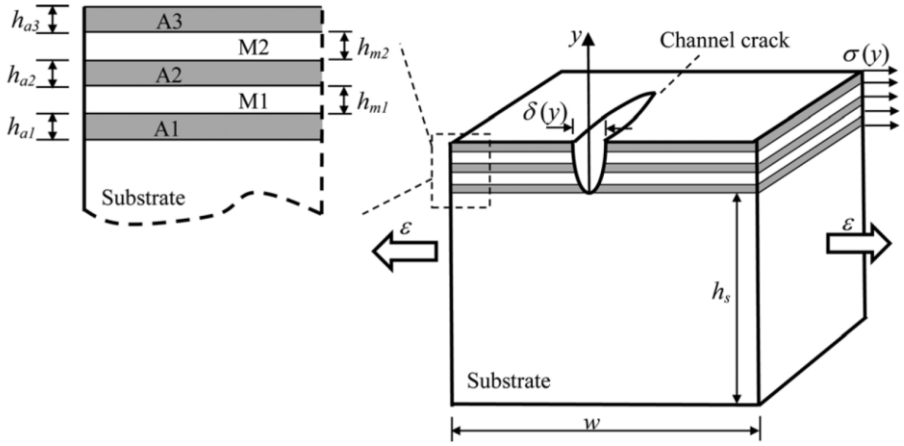

Figure 1.8: Schematic of a channel crack in 5-layer thin film consisting of 3 ALD inorganic layers and 2 MLD organic layers.[56]

1.2.2 Thin Film Fabrication and Testing Methods

Sample preparation: Polymer substrates such as PET, PEN or / and PI were cut using a laser cutter prior to thin film deposition to a size of 5 mm by 50 mm to prevent damage which can occur while cutting out samples after the deposition. Then, the thin film materials such as SiN_x, alumina (Al_2O_3) were deposited on top of the polymer substrate using PECVD method or ALD method. Similarly, MLD method can be used for the deposition of organic materials such as alucone and polyamide. In the case of subcritical crack growth study, 250 nm PECVD SiN_x (Unaxis PECVD system with radio frequency (rf) parallel plate configuration) were deposited on 125µm thick PET (Dupont Teijin Films Melinex ST505) and on PI (UPILEX-125S) at a temperature of 110°C, pressure of 1 Torr, 20W rf plasma and a rate of 10 nm/min.

Mechanical properties characterization: to quantify the driving force for channel crack propagation, mechanical properties of each layer must be known. In case of polymer substrates, a tensile test was performed to achieve the modulus value. Additionally, stress-relaxation curve can be measured to fit the viscous property of the polymer. Nanoindentation (Hysitron Triboindenter) was used to measure the modulus of thin film. Also, the residual compressive strain of thin film can be obtained using in-situ optical microscopy tensile test by straining the specimen up to the value below yield strain but over the threshold strain to form cracks and then reporting the applied strain upon unloading until cracks become closed and invisible. Figure 1.8 shows the process obtaining ε_{res} of the SiN_x thin films.

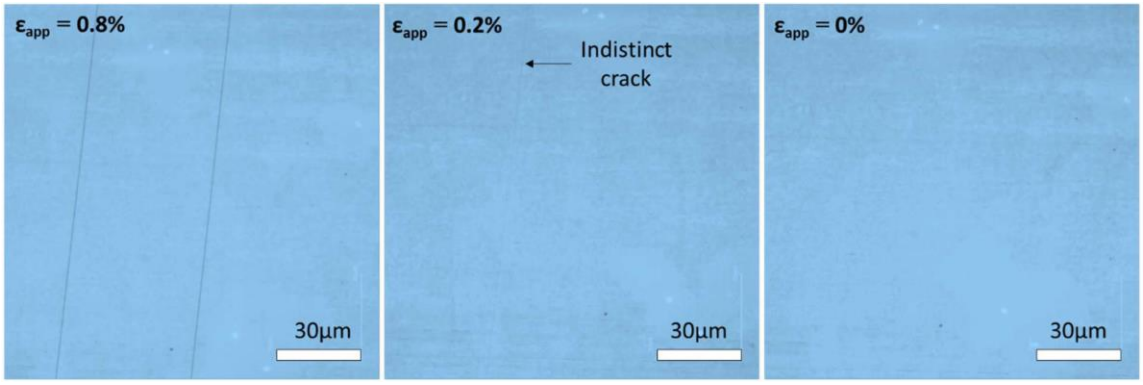

Figure 1.9: Approximation of ε_{res} in SiN_x based on optical images of cracks as a function of ε_{app}.

Microscopy and image analysis: In-situ microscopy from an optical microscope (Olympus LEXT, OLS4100) was used to observe the cracking behavior on the surface of the thin film deposited on the polymer substrate using a microtensile testing stage (Linkam

Scientific Instruments, TST350) as shown in Figure 1.9 (a). Crack extensions from the optical images were calculated (see Figure 1.9 (b)) and thus the rate of extensions are also obtained to plot subcritical crack growth rates as a function of driving force (*v*-G curve) as shown in Figure 1.9 (c). To observe the long-term crack growth behavior, samples were stretched under subcritical values of applied strain for up to a maximum of 5 days, i.e. 120 hours, so that a sufficient substrate cracking effect and the tendency of crack growth rate behavior can be observed and documented (see Figure 1.9 (d)). Environmental conditions were controlled to demonstrate the impact of environmentally assisted cracking by performing tests in dry nitrogen (*i.e.*, 2ppm) and in air (i.e., relative humidity content of 30%). For switching the environment to air from dry nitrogen, the lid was removed from

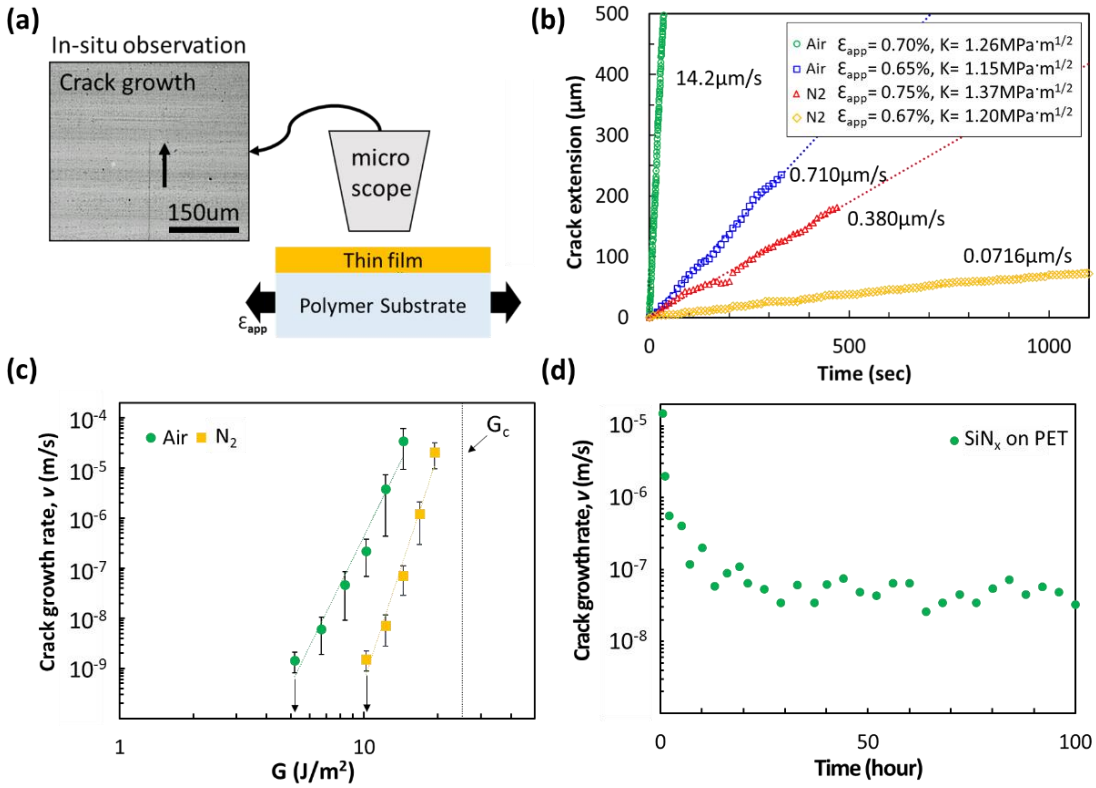

Figure 1.10: (a) Schematics of experimental setup and procedure on crack growth rate measurement. (b) crack extension observed from the optical images as a function of time (c) crack growth rate converted by the rate of crack extension as a function of driving force. (d) long term crack growth rate as a function of time.

the stage and the nitrogen supply was stopped. The density of cracks and crack were calculated by counting the number of propagated cracks in the observation area (region with a radius of 13.6mm at the center of specimen). Lastly, the crack configuration was analyzed using SEM images (Hitachi SU8230) and, if necessary, specimens were demonstrated using FIB (Nova FIB Micromanipulator) on where the channel crack is located.

1.3 Research Objectives

Based on the above discussion, the objectives of the present study can be summarized as follows:

(A) Identify the source of subcritical crack growth behavior in PECVD SiN_x barrier films. Quantify the EAC behavior using in-situ microscopy tensile tests.

(B) Quantify the crack growth rate behavior over an extended period of time to understand and analyze the effects of any additional failure modes. Explain crack configurations in chronological order and calculate their driving forces.

(C) Develop a simple and easy testing technique to quickly obtain subcritical crack growth-rate curves as a function of driving force (*v*-G curve).

(D) Quantify the *v*-G curves of various SiN_x films to develop a fabrication procedure that effectively reduces EAC compared to the one obtained in (A); perform experiments by controlling the ratio of silicon (Si) to nitrogen (N) and by encapsulating the SiN_x specimen in protective layers such as ALD.

(E) Develop a numerical model to obtain COS for specified crack configurations. Test nanolaminates and organic thin films to assess their mechanical failure properties.

(F) Develop a testing technique to calculate the high fracture energy of organic layers.
(G) Apply the calculated fracture energy from (F) to the model built in (E) and obtain an improved COS.

These objectives were constructed to ultimately develop mechanically reliable strong barriers using PECVD SiN_x, i.e., the processes described from (A) to (D), using alternative organic and inorganic nanolaminates, i.e., processes described from (E) to (G).

1.4 Dissertation Organization

This dissertation is organized in several chapters as follows:

- Chapter 2 deals with the crack growth behavior of a PECVD SiN_x film on PET substrate over a short period of time (< 0.5 hour) wherein the crack tip of these samples tested for 0.5 hour was confirmed to sit at the film / substrate interface without delamination.
- Chapter 3 presents the long-term crack growth behavior including the influence of both substrate cracking and adjacent neighboring cracks.
- Chapter 4 presents the alterations of EAC behavior in PECVD SiN_x films with ALD capping layer or with variations in stoichiometry.
- Chapter 5 presents the study for optimizing COS in composite films using organic / inorganic nanolaminates.
- Chapter 6 presents the conclusions from this investigation and recommendations for future work.

CHAPTER 2. SUBCRITICAL CHANNEL CRACK GROWTH IN PECVD SiN_x BARRIERS

2.1 Overview and Approach

Barrier layers that contain ultrathin inorganic hard coatings on polymer substrates have become indispensable in the flexible electronics industry for maintaining reliable operation of devices, with the most notable demand from OLEDs for flexible displays and thin film OPVs. For these applications, various barrier film architectures (multilayer stacks) and processing methods (PECVD, ALD, etc.) have been developed to create ultrabarrier films with an effective WVTR less than 10^{-4} to 10^{-6} $g \cdot m^{-2} \cdot day^{-1}$. Of these methods, multilayer amorphous silicon nitride (SiN_x) thin films grown by PECVD have recently found a lot of success in developing flexible ultrabarrier coatings with WVTR on the order of 10^{-6} $g \cdot m^{-2} \cdot day^{-1}$ [29, 32], and have been demonstrated on flexible displays.[30-31, 71-73] SiN_x films exhibits great barrier properties such as low porosity, and excellent transparency, while enabling low temperatures deposition (~100 °C) with high deposition rates (60 nm/min).[31, 74-76] Moreover, residual stresses can be controlled through the PECVD deposition conditions such as substrate temperature, plasma power, chamber gas pressure, and chemical composition (*i.e.*, stoichiometry effect in this case).[77-78] This allows the SiN_x films to have compressive residual stresses, which can prevent the growth of pre-existing microcracks without applied external loads.[2, 29, 60]

Many brittle films undergo environmentally assisted subcritical cracking, such as SiO_2 films.[46, 79-81] So far, there are few studies on EAC in SiN_x films available, although

environmentally assisted debonding at the interface between SiN_x and Copper layer has already been demonstrated. [51] Recently, Vellinga et al. [49] observed faster crack propagation in SiN_x barriers on PEN substrates in higher relative humidity surroundings using in-situ microscopy resistance measurements. They concluded that this environmental effect was highly unlikely due to the hygroscopic expansion of the polymer, and rather arguing EAC in SiN_x barriers. Guan et al. [50] also performed electromechanical two-point bending tests in dynamic and static loading modes to obtain the subcritical crack growth exponent *n* in SiN_x coatings on PEN substrates. Their results suggest that SiN_x thin films behaves differently from bulk Si_3N_4 ceramics that are essentially immune to EAC. [66, 82] However, these studies neither directly measured the crack growth rates as a function of driving force for channel crack propagation nor considered the aforementioned potential effects of polymer relaxation. Therefore, the goal of this study is to characterize and investigate the channel crack growth behavior of PECVD SiN_x films on a PET substrate under different environmental conditions by employing the in-situ microscopy tensile testing technique for crack extension measurement with time. Combined with numerical models, this study elucidates the origins of time-dependent subcritical crack growth behavior by differentiating the contribution of polymer creep / relaxation from that of EAC.

2.1.1 Mechanical Properties of PECVD SiN_x Thin Film

All the relevant mechanical properties for SiN_x films and PET substrate were obtained using in-situ microscopy tensile test, described in the section 1.2.2. The measured elastic modulus, E_f, of SiN_x film was 123 ± 5.8 GPa and a value of ν_f =0.253 was used, corresponding to the plane strain elastic modulus, E_f^*, of 131 ± 6.2 GPa. Residual

compressive strain of SiN_x film was found to be -0.15 ± 0.02 %. The measured elastic modulus of PET substrate, E_s, is 4.07 ± 0.12 GPa, and the 1% offset yield strength of PET, σ_y, is ~90.6 MPa. A value of $\nu_s = 0.3$ was used for PET. From the measured E_s^* and E_f^* values, the elastic mismatch $\alpha = 0.934$ and the corresponding dimensionless energy release rate $Z = 11.8$ were obtained. All these relevant mechanical properties for SiN_x films PET substrate were summarized in Table 2.1. Huang *et al*. studied the effects of substrate finite thickness and channel crack interactions on the driving forces.[62] For $\alpha = 0.95$, they showed that the semi-infinite substrate case can be approximated for $h_s / h_f > 60$ (h_s: thickness of substrate, h_f: thickness of film), a condition obtained for the 125μm thick PET / 250 nm thick films structure, *i.e.* $h_s / h_f = 500$. Driving force can be also largely unaffected by neighboring cracks as long as the normalized crack spacing, *S/h*, is larger than 150, which corresponds in this case to a crack spacing *S* of 37.5 μm. Therefore, neighboring crack interaction can easily be removed in the driving force calculation by measuring growing cracks at least 37.5 μm far from the adjacent neighboring cracks.

Table 2.1: Mechanical properties of PECVD SiN_x film and PET substrate.

Mechanical properties (units)	PECVD SiN_x film
E_f (GPa)	123 ± 5.8
ν_f	0.253
E_f^* (GPa)	131 ± 6.2
ε_{res} (%)	- 0.15 ± 0.02
E_s^* (GPa)	4.47 ± 0.25
σ_y (MPa)	90.6

As explained in the section 1.1.1, it has been shown that the creep of a viscous underlayer induces a time-dependent crack growth in the thin film.[44-45] However, in the case of 250nm film / 125μm substrate structure, a 3D viscous flow problem needs to be solved numerically to calculate the driving force, *G*, since their numerical solutions are applicable only for thin viscous sub-layers for which a shear lag model could be used. Thus, FEM was applied by collaborators Luo and Zhu using the FEM software ABAQUS 6.13 to determine the effect of viscous properties of the 125-μm-thick polymer substrate on

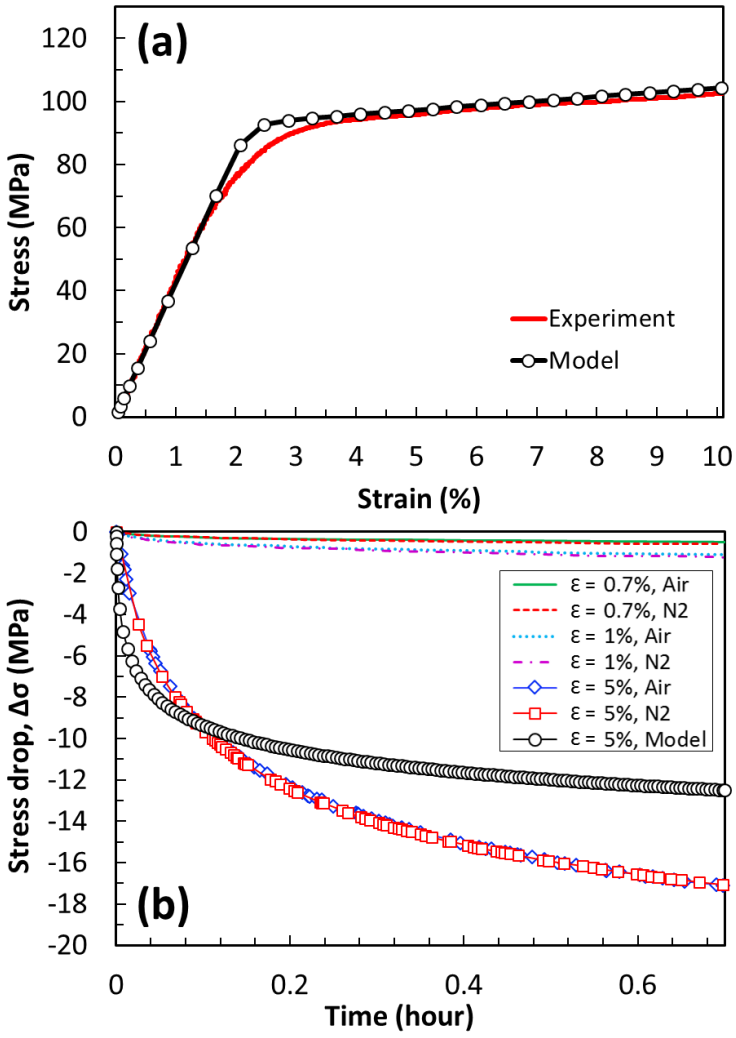

Figure 2.1: (a) Stress-strain curve of PET substrate. (b) Stress relaxation curves of PET substrate. Models are obtained by collaborators Luo and Zhu.

driving force, *G*, change.[70] PET was modeled as viscoplastic materials and SiN_x was assumed to behave elastically. The elastic strain rate is linearly proportional to the stress rate. Cowper-Symonds overstress power law was applied to calculate the plastic strain rate. The viscoplastic parameters of PET were obtained by fitting both experimental tensile stress-strain curve and stress relaxation curves (see Figure 2.1). Perfect bonding was assumed at the interface between its film and substrate. J-integral method was used for the driving force calculation at the crack tip. For the specimen kept at 0.95% applied strain, *i.e.* COS of 250nm SiN_x / PET structure, the results showed that peak stress as a function of time, which drops from 95 MPa to 82 MPa for 0.5 hour (see Figure 2.2). Such viscous stress relaxation in PET has a minor influence on the increase of driving force in SiN_x thin film; G increases from 25.2 $J \cdot m^{-2}$ to 25.4 $J \cdot m^{-2}$ for 0.5 hour. Therefore, the effect of viscous

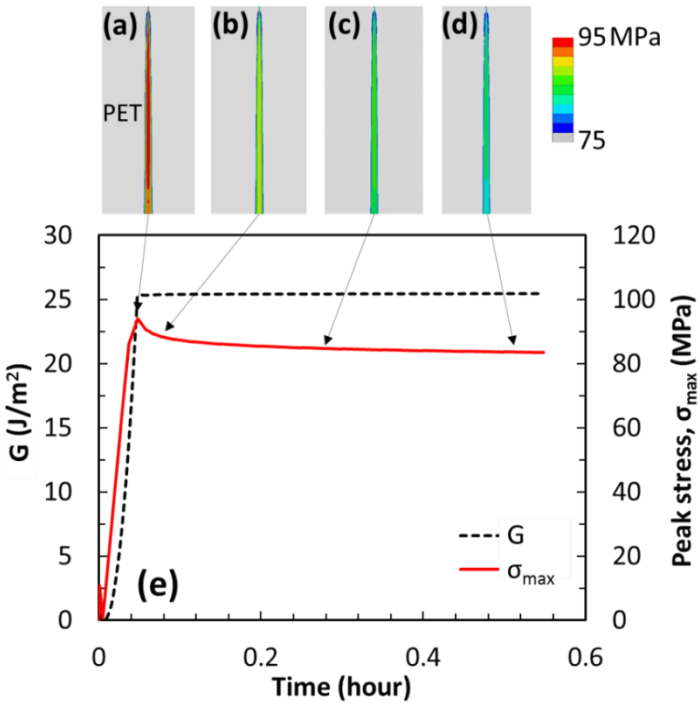

Figure 2.2: Energy release rate G with time evolution and stress beneath the crack wake in PET. (a-d) The von Mises stress contour in PET at different times as indicated in (e), showing the viscous stress relaxation effect. (e) Peak stress in PET and corresponding energy release rate for cracking in SiN_x film as a function of time. FEM performed by collaborators Luo and Zhu.

relaxation on driving force is negligible at subcritical strain within the time scale of 0.5 hour and thus the subcritical crack growth effect comes from environmental condition, *i.e.* EAC, not by viscous underlayer.

The critical energy release rate, G_c, *i.e.* driving force at COS, was also calculated to be 25.2 ± 1.26 J·m^{-2} for the 250-nm-thick coatings, which matches well with the linear elastic analytic solution (*i.e.*, G = 24.7 J·m^{-2} by use of Eq. 1), corresponding to a fracture toughness K_{Ic} value of 1.82 ± 0.03 MPa·m$^{1/2}$ by use of Eq. 3 (see Figure 2.3). K_{Ic} is equivalent to K_c in this work since samples being tested were in mode I loading. K_{Ic} values were also calculated for thinner SiN_x films based on the measured COS as a function of coating thickness by adapting the developed numerical model to thinner layers. Both COS and K_{Ic} values for the thinner SiN_x films are shown in Figure 2.4. The strain rate of 0.05%·s^{-1} were applied to measure COS, ε_c. K_{Ic} values were found to be slightly larger than the values measured with microbeams made of PECVD SiN_x, ranging from 1.54 to 1.73 MPa·m$^{1/2}$.[83] Since the tests consist of detecting cracks in a small area (258 × 258 μm^2)

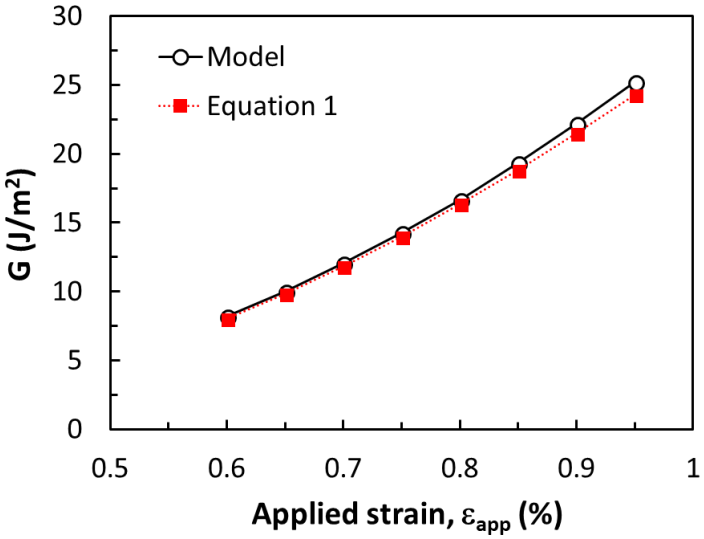

Figure 2.3: Calculated driving force, *G*, as a function of applied strain, ε_{app}, compared to the channel crack equation (Eq. 1). Model from collaborators Luo and Zhu.

within a large specimen (50 × 5 mm^2), the measured K_{Ic} values constitute upper limits on the actual K_{Ic}. Residual compressive strains were approximated as being equal to the residual strains measured for 250 nm thick SiN_x film. Fairly similar K_{Ic} values for thicknesses ranging from 50 to 200 nm to the values calculated for 250 nm thick SiN_x film show the thickness-independence of material properties, expected for a linear elastic and brittle materials.[64] For the 15 and 20 nm thick coatings, a discrepancy for the varying values are likely due to the large applied strain over 2.5%, generating a polymer substrate cracking at the crack tip, which was not considered in the model. A best power-law fit, resulting in $\varepsilon_c = 1.11h^{-0.443}$ ($R^2 = 0.995$) (see Figure 2.4), comes from the considerations: small-scale plasticity of the substrate, thickness-dependent residual strains, and absence of substrate cracking. However, a best $h^{-0.5}$ power equation also fits well ($\varepsilon_c = 1.11h^{-0.5}$ and $R^2 = 0.995$), bounded by the standard deviations of measured COS as shown in Figure 2.4, implying that Eq. 1 itself can reasonably predict the thickness dependence as observed experimentally with previous studies on ultrathin coatings.[38]

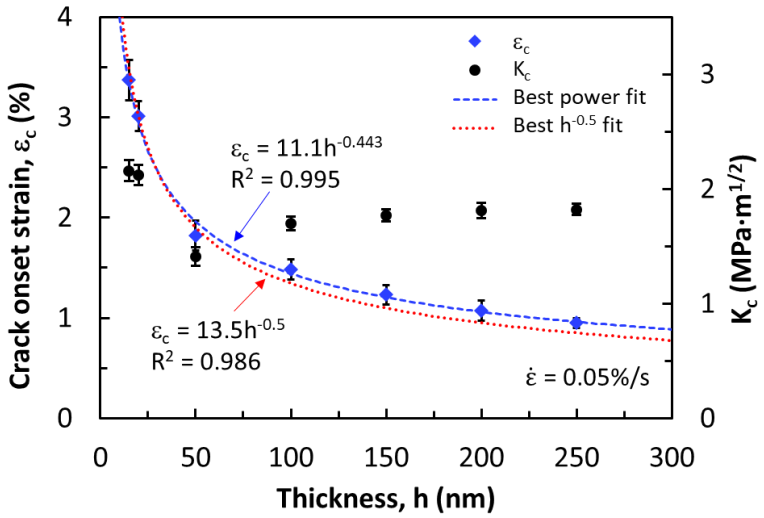

Figure 2.4: Influence of thickness on COS, ε_c, and fracture toughness, K_c, for SiN_x on PET substrate.

2.1.2 Environmentally-Assisted Cracking

The COS decreased from 0.95 ± 0.02 % to 0.75 ± 0.03 % by decreasing applied strain rate from 10^{-1} to 3 $\times 10^{-4}$ %·s^{-1}, suggesting a time-dependent crack growth in humid air.[2] In contrast, the COS in dry air decreases from 0.95 ± 0.02 % to 0.88 ± 0.03 % (see Figure 2.5).[2] The effect of strain rate on the COS is consistent with the study by Guan *et al.*[50], and the effect of humidity on time dependent crack growth is consistent with the study by Vellinga *et al.*[49] Here, the crack growth rates were further characterized as a function of applied strains from 0.6 % to 0.85 % in different environments, i.e. laboratory air, dry nitrogen, and dry air. In this work, hygroscopic expansion effect on driving force was not considered. Because the hygroscopic expansion of PET (8×10^{-6} $\%^{-1}$) in the laboratory atmosphere (~30 % relative humidity) results in an applied strain of 0.024 %, turning to a small decrease in applied stress in the case of displacement-controlled tests. The effect on

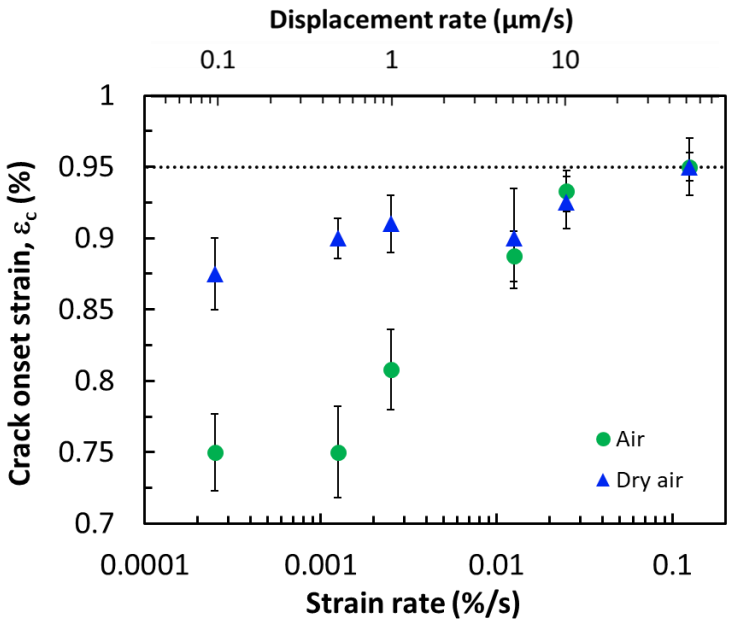

Figure 2.5: Effect of strain rate on COS of 250 nm thick SiN_x film in air and dry air at 25 °C.

driving force was deemed negligible (the elastic mismatch, $\alpha = 0.934$, increases by ~0.2% in dimensionless energy release rate Z from 0 to 30% relative humidity, same as driving force, *G*).

The in-situ observation of crack growth confirmed different behaviors as function of the humidity content. No difference was observed between dry air and dry nitrogen. First, the number of growing cracks was significantly higher in humid air compared to dry nitrogen (see Figure 2.6 (b)), with more than an order of magnitude cracks in the humid condition at both 0.6 % and 0.7 % applied strains. This suggests that the presence of water vapor affects the initiation of channel cracks. The average measured number of cracks is 43 in humid air versus 4 in dry nitrogen, while similar crack growth rates (~100 $nm \cdot s^{-1}$) are measured in humid air at 0.6 % (K = 1.0 $MPa \cdot m^{1/2}$) and in dry nitrogen at 0.7% (K = 1.3 $MPa \cdot m^{1/2}$). Since Eq. 1 applies to the growth of long channel cracks (which are initially present in the coatings), not their initiation, the environment is considered to accelerate subcritical growth of surface flaw into channel cracks, resulting in 10 times more channel cracks in humid air than in dry nitrogen for similar applied driving force. Moreover, Figure 2.6 (a) shows that the cracks also grow faster in the humid environment by an order of magnitude than in the dry environments. The average measured crack growth rates were also highly sensitive to the driving force (therefore the applied strain), explaining the aforementioned strain rate effects on COS. For example, the crack growth rate at 0.75 % of applied strain in humid air is measurable (~58.7 ± 38.4 $\mu m \cdot s^{-1}$), explaining the observed decrease in COS from 0.95 ± 0.02 % to 0.75 ± 0.03 % at an applied strain rate of 0.0003 $\% \cdot s^{-1}$, corresponding to a displacement rate of 0.1 $\mu m \cdot s^{-1}$.

The influence of humidity is further highlighted by considering the effect of specimen storage condition prior to testing, which may allow moisture to diffuse into the SiN_x coating, resulting in additional time dependent crack growth. Thus, some specimens were kept in glove box to minimize the moisture content. Also, these specimens were kept in the vacuum chamber at 110 °C for 1 hour prior to the PECVD for the same purpose. As shown in Figure 2.6 (a), crack growth rates were further decreased (solid square symbols) in the specimen kept in a dry environment (glovebox), compared to the one exposed to lab

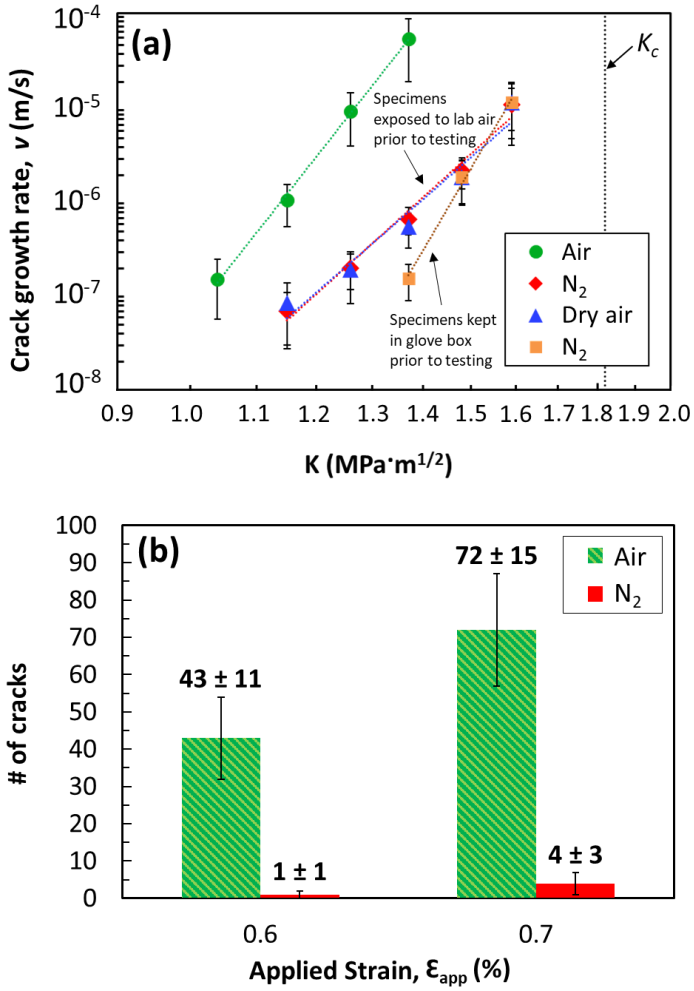

Figure 2.6: (a) Measured crack growth rates of 250 nm thick SiN_x as a function of stress intensity factor in air (green circles), nitrogen (red diamonds), and dry air (blue triangles). (b) Density of cracks in air and in nitrogen measured 30 min after first observed crack.[2]

air prior to testing (solid diamond and triangle symbols). A power law equation was used to fit the data:

$$v = C\left(\frac{K}{K_c}\right)^n \tag{12}$$

with coefficient n and C listed in Table 2.2 as a function of specimen storage and environment.

Table 2.2: n and C coefficients as a function of environment and specimen storage conditions.

Specimen storage	Environment	n (-)	C (m/s)
Specimen exposed to air	Air	21.8	2.78×10^{-2}
	N_2	15.5	6.91×10^{-5}
	Dry air	15.0	5.65×10^{-5}
Specimen kept in dry condition	N_2	29.3	6.89×10^{-4}

The crack growth rates in Figure 2.6 (a) were measured only from growing cracks that were not having particles in their path, which present on the PET substrate before SiN_x deposition. In the presence of a large densities of contaminants/particles (occurred depending on handling of the PET substrate prior to the deposition), channel crack growth behavior appeared to be different. For example, in dry air, at applied strain of 0.85 % (corresponding to stable crack growth of 11.6 ± 5.50 $\mu m \cdot s^{-1}$ in the absence of particles), cracks grew from particles at rates too large to be measured after an incubation period until they reached other particles and were arrested. After another incubation period, the cracks started again propagating from the particles at rates too large to be measured until they reached another particles in their path. This process repeated itself in the case of the tests performed in dry air, while still stable crack growth was observed in humid air from

particles to particles. The incubation period increased as applied strain decreased from ~250 ± 150 s at 0.9 % to 900 ± 650 s at 0.75 %. A possible explanation on this process is that, as the channel crack is arrested at a particle, polymer relaxation occurs at a larger rate (due to the stress concentration at the particle) and leads to an increasing stress field. The stress required for channel crack nucleation is likely to be larger than the stress required for channel crack propagation. Hence, the driving force is considered to be large enough to provide fast crack propagation. The lower applied strains would require the longer incubation periods as more time would take to intensify the stress field ahead of the particle. This reasoning holds only if the stress concentration at the particle is large enough to allow significant amount of polymer relaxation. At the same time, as opposed to the tests in dry nitrogen, environmentally assisted nucleation of channel cracks in humid air were clearly shown since the fast crack propagation from particles was not observed.

The time-dependent results shown in Figure 2.6 need to be restricted to short times (~30 minutes) after first observing channel cracking. As mentioned in section 1.1.2, FIB cross sections revealed the substrate cracking into the PET substrate. Further study on the long-term reliability of thin film barriers for flexible electronics will be addressed in the next chapter.

2.2 Testing Technique for Thin Brittle Films Deposited on Polymer Substrates

2.2.1 Current Technique for Cohesive Crack Growth Measurement

The cohesive fracture toughness, K_c, or fracture energy, G_c, of thin films are key material parameters to predict fracture failure. In addition, subcritical crack growth may

occur for instantaneous cracks, for materials that undergo EAC.[79, 84] In that case, the *v-K* (or *v-G*) curve must be characterized to predict time-dependent cracking behavior. Currently, two main techniques are used to measure the cohesive subcritical crack growth properties of thin films; the double cantilever beam test [85], and the residual-stress-driven channel crack growth technique [86-88] (see Figure 2.7 (a) and (b)).

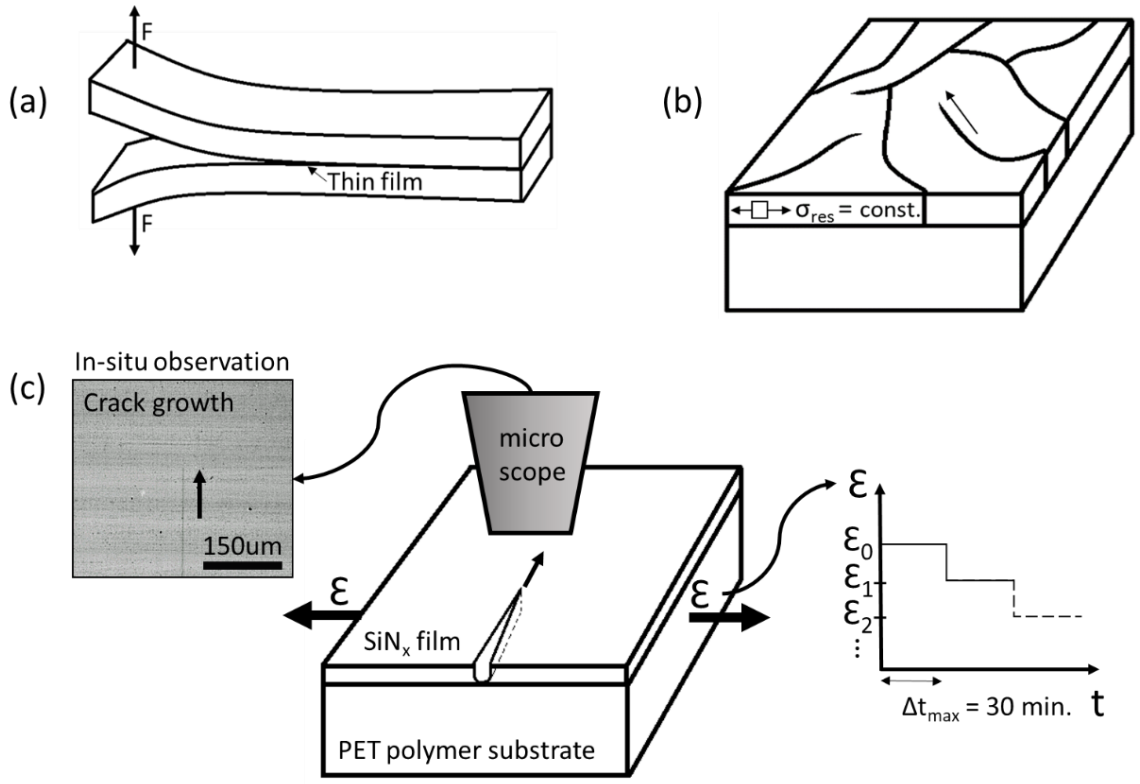

Figure 2.7: Schematics of techniques to measure the cohesive subcritical crack growth properties of thin films: (a) double cantilever beam (DCB) test, (b) residual-stress-assisted channel crack growth technique, (c) external-load-assisted channel crack growth technique.

The double cantilever beam specimen is prepared by sandwiching the thin film of interest in between two thick substrates [85, 89]. Then, the specimen is pre-cracked (for example using a dicing saw and a wedge, or by overloading), and must be performed in a

manner to have a crack propagating through the thickness of the thin film of interest to obtain a valid test. Post mortem chemical characterization of the two mating fracture surfaces can be done to validate the test. A preliminary double cantilever beam test can be done to measure G_c. Once G_c is characterized, a subcritical crack growth double cantilever beam test consists of increasing the applied load up to a value corresponding to $G \sim G_c$, at which point the crosshead displacement of the machine is fixed. As a result of subcritical crack growth, load relaxation occurs, and a full *v*-*G* curve can be obtained simply by measuring the transient load evolution over time.

In contrast, the residual-stress-driven channel crack growth technique consists of in-situ microscopy, observing under a microscope the extension of channel cracks due to EAC that develop in a thin film of interest under residual tensile stress on a substrate. Channel cracks can be introduced using indentation [86-87] or by scribing the sample surface [88, 90]. As previously mentioned, the driving force G can be calculated by knowing the residual stress in the thin film, σ_{res}, the film thickness, h_f, the thin film plane strain elastic modulus, E_f^*, and the elastic modulus mismatch between the thin film and substrate (see Eq. 1). Specimens are prepared by varying thickness and residual stress, and many specimens are required to obtain a full *v*-*G* curve in this case because each specimen can provide only one G value. Although sample preparation is much easier compared to the double cantilever beam tests, it is difficult to control the specimen to provide the applied G to be large enough (at least to exceed the threshold value for EAC, and ideally to approach G_c). This technique may not even work for ultrathin films such as ALD coatings for which residual stresses may not be large enough to obtain an appropriate G value. One solution around this issue may be to increase Z by using a compliant substrate with respect

to the thin film of interest. Or a compliant buffer layer can be added between the thin film of interest and stiff substrate as Z is low for stiff substrates [88, 90-92]. More importantly, this residual-stress-driven channel crack growth technique cannot work if the thin film is under residual compressive stresses. Residual stresses are mainly dictated by the thin film deposition conditions and thermal history, which in turn may affect also the thin film microstructure and therefore the G_c value and v-G curve. To circumvent these issues, a residual-stress-driven channel crack growth technique can be developed, which relies on applying a tensile load onto a specimen that consists of a brittle thin film onto a PET substrate. This technique is then especially well-suited for testing thin films that may be used in flexible electronics and that may be deposited at low temperatures on such polymer substrates. Especially note that substrate-relaxation-induced subcritical crack growth was negligible.[2] In this study, its feasibility was demonstrated by further improving the technique to enable the characterization of a full v-G (or v-K) curve using a single specimen.

2.2.2 External-load assisted channel crack growth technique

Thin film channel crack growth measurement technique in this study relies on the in-situ microscopy tensile testing of a 50-mm-long specimen. This consists of 125μm thick heat stabilized PET (Dupont Teijin ST-505) substrate with a thin film deposited on top using a microtensile testing stage (Linkam Scientific Instruments, TST350, with a 0.01 N load resolution, and a 10 μm displacement resolution); see Figure 2.7 (c). The stage allows testing under controlled environments by continuously flowing gas inside the chamber, as well as under controlled temperature. The crack growth observations during the tests are

performed under an optical microscope for thick enough films (typically >100 nm) for which cracks can easily be detectable, or under a laser scanning confocal microscope (Olympus LEXT, OLS4100) for films as thin as 15 nm. A test consists of loading the specimen up to a strain ε_0 at which several channel cracks develop and grow in a fast manner (corresponding to $G_0 \sim G_c$). This first step allows the nucleation of many channel cracks whose growth will be tracked throughout the rest of the test. The applied strain is then decreased to a slightly lower value $\varepsilon_1 = \varepsilon_0 - \Delta\varepsilon$ (the minimum $\Delta\varepsilon$ is 0.02 %), and the growth of several cracks is tracked for a maximum duration of 30 minutes (the choice for this value will be explained later) in order to obtain an average crack growth rate for this corresponding G_1 value. The process is then repeated to ε_2, ε_3, etc., until ε_n for which no crack growth is detected within 30 minutes. Using a resolution of ~1 μm for crack tip detection with the optical microscope at a 10X magnification, this minimum measurable crack growth rate is 5.5×10^{-10} m·s^{-1}. For a given applied strain, ε_{app}, the driving force G can be calculated using the Eq. 1. The technique presented in this specific study is an improved version of the previously employed technique [2], whereby a specimen is directly loaded to a given strain (ε_1, ε_2, … or ε_n) and crack growth rates are only measured for that given strain. The former technique therefore required a larger number of specimens to obtain a *v*-*G* curve, as only one *G* value was tested per specimen.

Crack growth tests demonstrating this new technique were performed with 250-nm-thick PECVD SiN_x films deposited at 110°C on the heat-stabilized PET substrate (exhibiting excellent dimensional stability up to 150°C), previously demonstrated susceptible to EAC.[2] Using ellipsometry, the film thickness was h_f = 254 ± 1 nm. The elastic moduli of the SiN_x film and PET substrate were measured to be E_f = 123 ± 5.8 GPa

and E_s = 4.07 ± 0.12 GPa, respectively, corresponding to plane strain elastic moduli values of E_f^* = 131 ± 6.2 GPa and E_s^* = 4.47 ± 0.25 GPa. The corresponding Z is 11.8 ± 2.2. A compressive residual strain of ε_{res} = -0.15 ± 0.02% was measured in the SiN_x film [2]. Based on a measured applied strain of 0.95 ± 0.02% at which fast channel crack propagation is observed, fracture energy, G_c, was calculated to be 25 ± 5 J/m^2 using Eq. 1, accounting for the errors associated with each term of that equation. This G_c value consists of an upper limit based on the measurement technique [2], and is in fact slightly larger than reported G_c values (ranging from 5 to 15 J/m^2)[93-94] for other PECVD SiN_x films deposited under different conditions.

Figure 2.8 shows *v*-*G* curves obtained with the developed thin film channel crack growth measurement technique for the 250-nm-thick SiN_x films for two different temperatures (25 and 85 °C) and two different environments (humid air and dry N_2). For the dry N_2 experiments, the specimens were stored in a glove box prior to the tests in order to minimize the amount of adsorbed water on the specimens. The driving force G was calculated using Eq. 1, as the previous numerical model [2] revealed that this formula is very accurate for applied strains up to 0.95 % (the small discrepancy likely results from yielding effects in the PET, and was shown to be much more negligible than the effects predicted by the Hu-Evans model). The empty symbols represent tests for which the specimens are only tested at a given strain value [2]; the error bars associated with these tests represent the standard deviation from average rates calculated over typically 20-30 measured growing cracks. These data highlight EAC in the SiN_x films [2, 49-50], which is a thermally activated phenomenon [95-97]. The solid symbols represent data from the improved technique, whereby one specimen is tested to provide a full *v*-*G* curve. Here the data are averaged over 2 or 3

tested specimens. The solid data match very well the empty data (most of the solid data points are within the error bars of the empty data points), highlighting the fact that the improved technique is a fast and sufficiently accurate way of obtaining a *v*-*G* curve with only one or two specimens. More importantly, the improved technique allows measuring crack growth rates below 10 $nm \cdot s^{-1}$, whereas the previous technique was limited to rates above 100 $nm \cdot s^{-1}$. The reason for this discrepancy is related to the number of growing cracks. By first loading the specimen at large strains at which many channel cracks nucleate, a large number of cracks can continue to grow under lower strains corresponding to lower *G* values. In contrast, if a specimen is first loaded to a low strain value, channel cracks may not nucleate, preventing crack growth measurements. Hence, the improved technique provides an entire *v*-*G* curve, including importantly the threshold regime.

This external-load-assisted channel crack growth technique provides several advantages over the two main techniques described in the Introduction. Compared to the double cantilever beam test, the sample preparation is much simpler and only requires depositing the thin film of interest onto the PET substrate. One challenge associated with the double cantilever beam test is to pre-crack the specimen such that the crack tip lies within the thickness of the thin film of interest. This may be especially challenging for ultrathin films (such as thickness below 50-100 nm) for which the interfaces (with the substrates and/or glue required for the "sandwich" preparation) would be in close proximity to the crack tip; if the crack tip deviates onto one of these interfaces, the cohesive fracture energy of the thin film of interest cannot be measured anymore. Also, this requirement can only be checked with post-mortem chemical characterization of the fracture surfaces for each test. In addition, the double cantilever beam test does not provide direct visualization

of the crack front. Instead, the crack size (and therefore crack growth rate) is approximated through an analytical model of the specimen's compliance which relies on a uniform crack front [85, 89]. In contrast, the external-load-assisted channel crack growth technique relies on simple specimen preparation and direct observations of the cracks to measure their growth rates. By applying an external load to drive crack propagation, a residual tensile stress in the thin film of interest to provide a large enough driving force is not required. For example, the SiN_x films characterized in this work have a compressive residual stress. Therefore, this technique increases significantly the range of thin films for which the crack growth rates can be characterized, including ultrathin films and films with compressive residual stresses. It was also demonstrated that a full *v*-*G* curve can be obtained by varying the applied strain during a single test, similar to what is done with the double cantilever beam

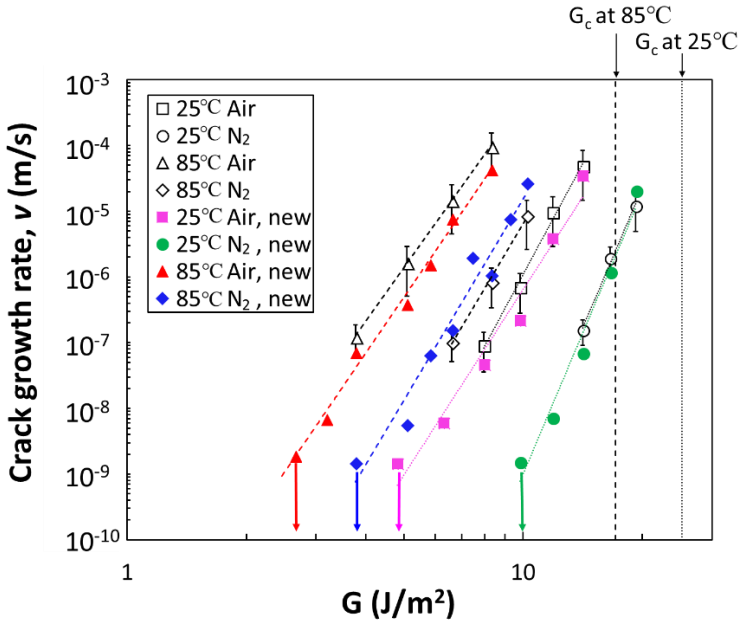

Figure 2.8: *v*-*G* curves obtained for 250nm SiN_x films on 125µm PET in various environmental conditions. The empty symbols represent tests for which the specimens are only tested at a given strain value, and the solid symbols represent data from the developed technique, whereby one specimen is tested to provide a full *v*-*G* curve.[1]

test and unlike the residual-stress-driven channel crack growth technique which requires as many specimens as data points of the *v*-*G* curve.

2.2.3 Limitations of external-load assisted channel crack growth technique

The main particularity of the external-load-assisted channel crack growth technique is that it requires a polymer substrate to allow loading to large strains (up to 1% for the present tests) without substrate fracture. In comparison, the residual stress driven channel crack growth technique typically uses stiff substrates such as silicon [86-87, 90], and the double cantilever beam specimens are typically made of a stiff substrate (such as glass or silicon wafer) [85, 98]. Hence there are several restrictions associated with this technique (in addition to the ones already existing for the channel crack growth technique [12]) that relate to the plastic and/or viscoplastic deformation of the substrate. First, the driving force for channel crack growth must be properly evaluated, for example using finite element models, as Eq. 1 may be inaccurate in the case of local yielding in the substrate. The previous finite element model of the SiN_x / PET system revealed that Eq. 1 is reasonably accurate (within 3.6%) for an applied strain of 1% [2], whereas the shear lag model of Hu and Evans [99] significantly overestimated the effect of local yielding on *G*. Second, the viscoplastic behavior of the polymer substrate must be such that it does not induce significant time-dependent crack growth. Indeed, Suo and co-workers demonstrated that time-dependent cracking of an elastic film made of a material that does not undergo any subcritical cracking can still occur if a viscous underlayer or substrate is present [100-102]. Finite element models can also be used to quantify the amount of increase in *G* as a result of stress relaxation in the polymer substrate. The model showed that for an applied strain of 0.95%, the increase

in *G* due to substrate relaxation over a period of 30 minutes is only 0.8% (from 25.2 at t = 0 to 25.4 $J \cdot m^{-2}$ at t = 30 min) [2], and therefore plays a negligible role in the fast crack growth behavior observed in Figure 2.8. The results therefore demonstrates the feasibility of the technique on PET for applied strains up to 1%. If larger strains are required (for example, for thinner films (per Eq. 1), or if a different polymer substrate / testing temperature is used, finite element models should be performed as well to address this issue and further validate the technique. Last but not least, the driving force calculation (Eq. 1) is only accurate for a channel crack lying at the thin film / substrate interface [103]. It is often the case for a thin film on a stiffer substrate, as the driving force *G* decreases as a crack reaches the interface [104-105]. However, for a stiff thin film on a compliant substrate, the driving force increases as a crack reaches the interface [104-105], which may lead to some amount of substrate cracking depending on the fracture energy or time dependent fracture properties of the substrate. For example, substrate cracking of the PET (several micrometers deep) was observed for a specimen held at 0.6% for 5 days, also shown in the Figure 1.5 [2]. However, no cracking of the PET was observed when held for 30 minutes, which is the reason why the specimens were only held for a maximum duration of 30 minutes at a given strain to measure the crack growth rates. It is therefore important to perform post-mortem examination (in this case, cross-section SEM imaging) to ensure the proper cracking configuration.

2.3 Kinetics of Environmentally Assisted Cracking in PECVD SiN_x Films

EAC in SiN_x barrier films was described in the previous sections. Experimentally measured crack growth rates in laboratory air were an order of magnitude higher than those in dry environments (dry air and dry nitrogen), while the crack growth rates in dry air and

dry nitrogen had no visible difference. This means that water molecules are the chemically active species for EAC in SiN_x film. In the case of silica (SiO_2), the reaction-controlled region in the *v*-*K* curve (or *v*-*G*) is a strong function of water concentration, which relies on a stress-enhanced chemical reaction between water and glass at the highly stressed crack tip.[69, 95, 106] Similarly, at crack tips in SiN_x films, the Si-N bond-breaking rate can be increased via the stress-assisted chemical reaction with water molecules, similar to the surface dissolution of Si_3N_4: $Si_3N_4 + 6H_2O \rightarrow 3SiO_2 + 4NH_3$.[107]

To further understand the kinetics and chemistry of EAC in SiN_x, a combination of experiments and atomic modeling was used. The first step is to determine the kinetic coefficients, *i.e.* the activation energy and activation volume. The experiments were performed by measuring crack growth rates under different loading and environmental conditions, *i.e.*, strains and temperatures. A widely used model was applied to calculate the activation energy and activation volume, described in detail in section 1.2.1. Based on previous results at 25 °C, polymer relaxation in this temperature range is unlikely to play a significant role on subcritical crack growth.[2]

The measured crack growth rates in SiN_x films in humid air and in dry nitrogen at both 25 and 85 °C are shown in Figure 2.8. Using the power law equation (Eq. 12) and relation between energy release rate (driving force), G_{ss}, and stress intensity factor, K_c, (Eq. 3), the values of *n* were found to be ranged from 17 to 28, that are consistent with typical values of reaction-controlled region.[51, 66] There are several models addressing the kinetics of subcritical crack growth in the reaction-controlled region.[108-110] The most widely accepted one was promoted by Wiederhorn and Bolz,[108] derived by the theory of Hilling and Charles[111] based on the chemical reaction rate theory. As mentioned in section 1.2.1,

The crack growth rate (in terms of external load and thermodynamic quantities) has an Arrhenius type relationship (Eq. 5).

By applying Eq. 5 to the fitted curves of measured data (Figure 2.8), the coefficients, *b*, were obtained, and then used to calculate the activation volume, Ω, using Eq. 6. Table 2.3 summarizes the coefficients, b, and the corresponding activation volumes, Ω, as a function of environment and temperature. Results show that the activation volume is temperature-dependent. Due to the lack of studies on the kinetics of subcritical crack growth in SiN_x, the activation volumes for SiN_x obtained in this study were compared with values of soda-lime-silica reported in the literature, considering that SiO_2 also undergoes stress corrosion by water and is widely studied. Dauskardt *et al*. reported that the activation volume of soda-lime is 1.57 $cm^3 \cdot mol^{-1}$ in both moist air and dry N_2[66] and Wiederhorn et al. showed that the value is 1.46 $cm^3 \cdot mol^{-1}$ in moist air.[69, 112] These values for soda-lime are very close to the activation volumes for SiN_x obtained in this study, although the materials are different.

Another significant parameter controlling the kinetics of crack growth behavior, activation energy, *U*, was also experimentally determined. Figure 2.9 shows the crack growth rates measured as a function of reciprocal temperature in air. The applied driving force was kept to be 8.65 $J \cdot m^{-2}$ by controlling the applied strains (in Eq. 1) to produce equal driving forces at varying temperatures. Here, three temperatures are considered, 25°C, 55 °C, and 85 °C. The fitted slope shown in Figure 2.9 is equal to the slope in Eq. 4 and Eq. 5. U = 0.89 eV (=85.7 $kJ \cdot mol^{-1}$) was obtained using Eq. 4. Assuming that the *b* is

temperature-independent, average value b = 0.049 $m^{5/2}\cdot mol^{-1}$ can be used in Eq. 5, and then U = 1.43 eV (=138 $kJ\cdot mol^{-1}$) was obtained.

Table 2.3: Coefficient *b* and activation volume Ω as a function of temperature and environment.

Temperature	Environment	b ($m^{5/2}$/mol)	Ω (cm^3/mol)
85 °C	Air	0.056	1.11
85 °C	N_2	0.056	1.11
25 °C	Air	0.042	0.83
25 °C	N_2	0.046	0.91

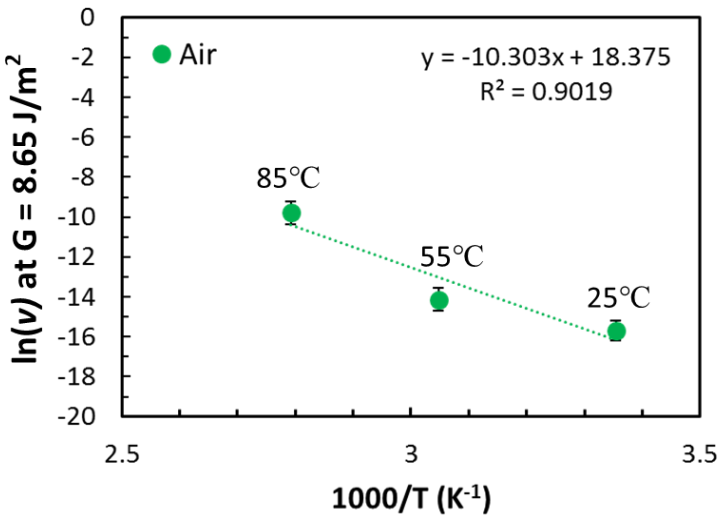

Figure 2.9: Dependence of logarithmic crack growth rate on reciprocal temperature for a channel crack in a 250 nm-thick SiN_x film in air.

Collaborators Luo and Zhu performed atomic simulations on models consisted of a water molecule and a cluster of silicon nitride to understand the mechanism of the stress-enhanced hydrolysis reaction in molecular level. Both the activation volume and activation energy were obtained from the minimum energy paths. The selected attacked bond was found to be the most energy-favored broken spot (Figure 2.10). The calculated activation

volume was 4.6 $cm^3 \cdot mol^{-1}$. The activation energy U was found to be 1.45 eV without loading and 0.95 eV with loading to 10% strain. The values were in the comparable range with experimentally obtained values (0.89 - 1.43 eV).

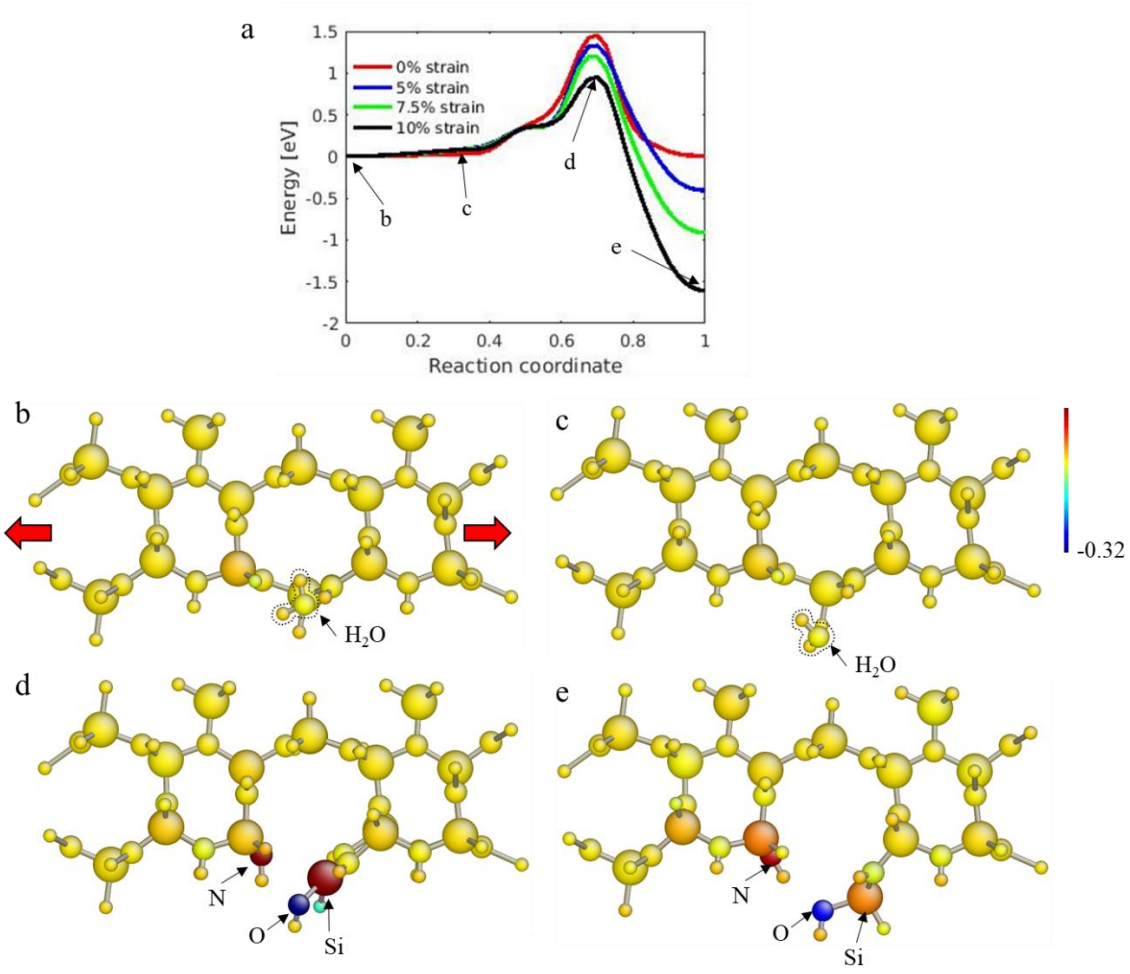

Figure 2.10: Simulation results for model II. (a) Minimum energy paths of hydrolysis at different stresses. Energy variation was plotted relative to the initial state as a function of the normalized reaction coordinate. (b)-(e) Atomic configurations along the transition pathway of hydrolysis under 10% strain: (b) initial state, (c) a state after reaction, (d) saddle-point configuration, and (e) final reacted state. Atoms are color-coded by charge variation relative to the initial configuration (a). The red arrows show the direction of loading.

2.4 Summary and Conclusions

The use of COS, ε_c, at high strain rates was found to be insufficient to define the safe operating envelope against channel cracking for SiN_x barrier films on PET substrates, due to time-dependent crack growth. Specifically, it was shown that the channel crack growth in SiN_x barrier films can occur at strain levels 35% below the apparent ε_c due to environmentally assisted crack growth. This behavior likely results from moisture-assisted cracking, with a measured power law exponent of ~22 in laboratory air and ~29 in dry N_2 for specimens stored in a dry environment prior to testing. As such, the environmentally dependent crack growth behavior has been appropriately characterized for the first time in barrier films on flexible substrates to better define the reliability of hermetic coatings for flexible devices. This approach of testing can be widely used for other thin barrier films since the state-of-the-art technology adopted allows for in situ visualizations down to 15 nm in thickness.

The external-load-assisted thin film channel crack growth technique was developed to measure the subcritical crack growth properties of thin films (*i.e.*, crack velocity, *v*, versus the strain energy release rate, *G*), and demonstrated using 250-nm-thick SiN_x films on PET substrates. The main particularity of this technique is that it requires a polymer substrate to allow loading to large strains (in order to induce channel cracking) without substrate fracture. Its main advantages are to provide a full *v*-*G* curve with a single specimen while relying on a simple specimen preparation and straightforward crack growth characterization. Importantly, the technique can be employed for a much larger range of thin films compared to the residual-stress-driven, thin film channel crack growth tests, including ultrathin films and thin film with residual compressive stresses. The restrictions

to a proper use of this technique, related to the viscoplastic deformation of the substrate, were also discussed.

Lastly, the kinetics of EAC in SiN_x thin film was investigated experimentally by applying experimental data to the crack-tip interaction model. As a result, activation volume of 0.83 - 1.11 $cm^3 \cdot mol^{-1}$ and activation energy of 0.89 - 1.43 eV were obtained, similar to the values obtained in the simulations conducted by collaborators Luo and Zhu. Therefore, the observed EAC in SiN_x could be explained by thermodynamically favorable mechanism of the water molecules reaction with hydrogen-passivated SiN_x barrier films.

CHAPTER 3. SUBSTRATE CRACKING EFFECT ON TIME DEPENDENT CRACKING IN SiN_x BARRIERS

3.1 Overview and Approach

Previous work has already quantified the effect of substrate cracking on the driving force for channel cracks [52-53], interaction with neighboring cracks by crack spacing[113-114], and their application as sensors[115]. However, the influence of substrate cracking on the long-term time-dependent subcritical cracking has not been studied. In this work, further investigation was made on the time-dependent EAC in PECVD SiN_x barrier films by testing over extended periods of time (*i.e.* days versus minutes in contrast to the chapter 2).[2] Experimental and numerical results help elucidate the effects of substrate cracking on the driving force (and therefore velocity) of channel cracks in PECVD SiN_x barrier layers, which is key to predicting long term damage growth in barrier films under deformation. Specifically, results in this study highlight various scenarios of increasing, decreasing, or constant crack velocities depending on the substrate cracking configuration and distance to surrounding cracks (*i.e.* crack density). Details of the experiments and results are described in the following sections.

3.1.1 Experimental details

In addition to the basic sample preparation and experimental information explained in section 1.2.2, the crack growth rates were measured after confirming the required crack

spacing that involves or eliminates the interaction from neighboring cracks while optical imaging tracked the observation area (region with a radius of 13.6 mm). Specifically, 0.58% applied strain was required to isolate the crack growth not to interact with neighboring cracks and not to increase the density of cracks. The external-load-assisted channel crack growth technique was applied to accomplish this without difficulty (see section 2.2.2). Some of tested specimens were further investigated for imaging (with 30 kV 1-3 nA for FIB on the area of 30 by 30 μm^2 etching up to 10 μm deep and 5 kV 0.4 nA for SEM) on the location of channel crack. Au/Pd was sputtered (10-20 nm) on the tested specimen before FIB to reduce charging effects.

3.1.2 Crack Configuration

As mentioned in section 1.1.2, the SEM images revealed an absence of substrate cracking for the specimen held at 0.75 % applied strain for 0.5 hour (see Figure 1.5 (a)). This is consistent with the analysis in the previous work on the *v*-*G* curve of SiN_x films experimented within 0.5 hour.[1-2] In contrast, SiN_x/PET specimen exposed to atmospheric condition for 5 days revealed the substrate cracking into PET directly under the SiN_x channel crack (see Figure 1.5 (b)). The depth of substrate cracking from the interface with SiN_x layer was found to be ~8 μm, 32 times of the film thickness. Thus, the PET substrate undergoes crazing or micro-yielding at the highly stressed channel crack line of the SiN_x coating, which results in substrate cracking evolving with time. This process is known as static fatigue or creep rupture.[116] As will be shown in the later section in Figure 3.5, SEM images of a SiN_x/PI specimen held for 2 days at 0.75 % revealed very little damage in the substrate, while a SiN_x/PET tested under the same conditions revealed again the significant

amount of substrate cracking. Here, fairly constant crack growth rates were observed for SiN_x/PI, while substantial changes in crack growth rates were observed for SiN_x/PET. It is likely that the substrate damage is responsible for the observed changes in crack velocities, presumably via changing the driving force for crack propagation, influencing its crack growth rate. To explain the observed crack growth rate behaviors over time, finite element models were used to quantify the substrate cracking effect on the driving force for crack propagation through the J-integral approach. Channel cracks in the thin film layer, including various depth of substrate cracking and spacings between a growing crack and neighboring cracks, was set up in the model to create appropriate crack geometries. The calculated driving force was used to predict the crack growth rate using the *v*-*G* relationship (see Figure 3.1).

3.2 Quantification of Subcritical Crack Growth Rate Behavior

3.2.1 Single Crack Growth Rate Behavior

As mentioned previously, substrate cracking in PET has been observed in the specimen tested for a long period of time. Accordingly, crack growth rate / density of cracks (*i.e.*, crack spacing) were measured for a long period of time to capture the combined effects of neighboring cracks and substrate cracking on the crack growth rate evolution in the film. First, change in crack growth rate was studied for an isolated propagating crack with substrate cracking. Finite element modeling result by Luo *et al*. showed that the change of driving force of crack growth is less than 1 % if the crack spacing is greater than 135 μm (Figure 3.2 (c)) and therefore a crack spacing of at least 135 μm was ensured for a crack to be isolated. The external-load-assisted channel crack growth technique was

applied to easily capture the crack growth at low strain and thus measurement can be started from the beginning of test.[1] Based on modeling results (Figure 3.2 (b)), the development of substrate cracking in the presence of an isolated crack increases the driving force due to loss of mechanical constraint to crack opening displacement, and therefore the crack growth rate increases. Figure 3.2 (a) shows that, for low applied strains of 0.5 % and 0.55 %, constant growth rates were observed, which is an indication of no substrate cracking. However, at 0.58 % applied strain, the growth rate increased from 8.3 $nm \cdot s^{-1}$ to 100 $nm \cdot s^{-1}$ over a period of 30 hours (see Figure 3.2 (a)), corresponding to increase in driving force of 33.7 % from 7.03 to 9.40 $J \cdot m^{-2}$ from its characterized *v*-G curve (see Figure 3.1). Substrate cracking of 50-100 nm would be required to increase that much based on Figure 3.2 (b), reasonable in the sense that no damage was observed for 0.5 and 0.55%, and substrate cracking was observed at 0.6 % for 5 days.

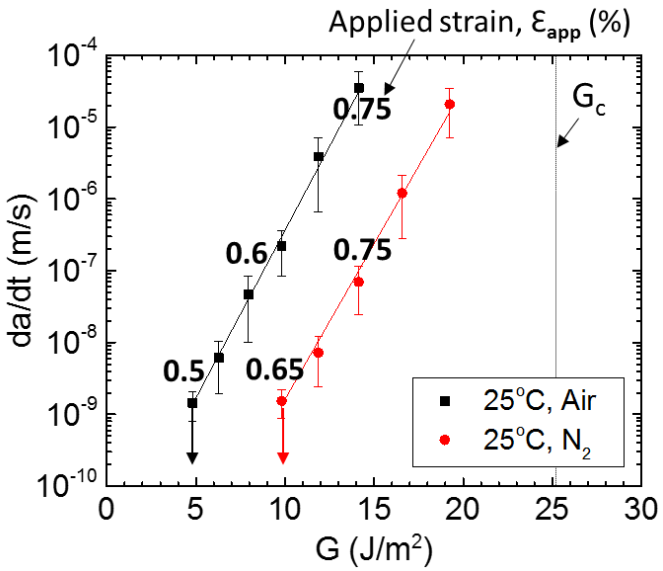

Figure 3.1: *v-G* curve of 250nm SiN_x on 125µm PET.

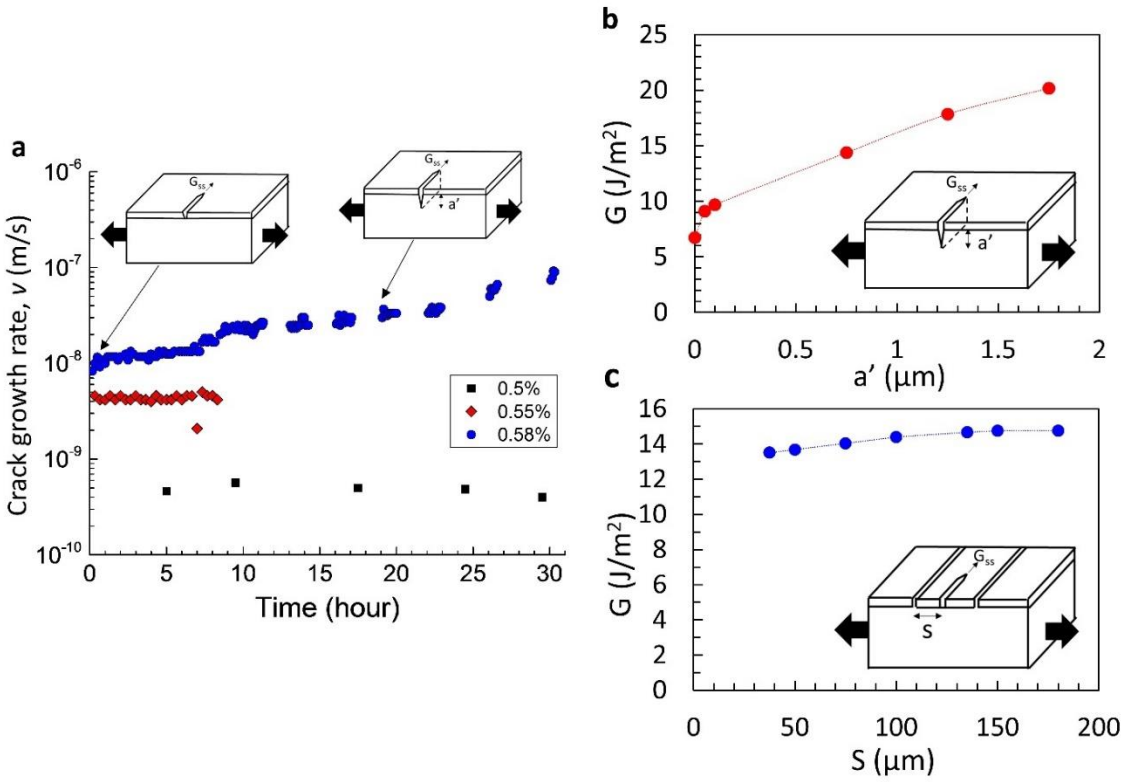

Figure 3.2: (a) Measured crack growth rate in SiN_x / PET at the applied strain of 0.5, 0.55 and 0.58 % in air. (b) Calculated driving force of an isolated crack as a function of substrate cracking depth a', when the applied strain is 0.58 %. (c) Calculated driving force of a crack with spacing S to the neighboring crack on its either side, when the applied strain is 0.75 %.

3.2.2 Multiple Crack Growth Rate Behavior

Finite element analysis was conducted by collaborators Luo and Zhu. to elucidate the neighboring cracks' and growing crack's substrate cracking impact on crack driving forces. Results showed that substrate cracking in the two adjacent cracks reduced the driving force in the growing crack, as the depth into the substrate increased. The driving force decreased by 40 % with the increase of substrate cracking depth in the neighboring cracks up to 4 μm (Figure 3.3 (a)). This is due to the loss of mechanical constraint in the neighboring cracks as the substrate crack grows in the PET. This has the equivalent effect

of closing the growing crack and reducing the energy dissipated for channel crack growth. Figure 3.3 (b) shows the effect of substrate cracking on the growing crack when the neighboring cracks also induce substrate cracking. While substrate cracking depth in the neighboring cracks was kept at 4 μm, the crack driving force increased up to 65 % when the substrate cracking under the growing crack was introduced up to 1 μm in depth. This is consistent with the results shown in the previous section (Figure 3.2 (b)), *i.e.* increase in driving force with substrate cracking evolution in growing crack.

Figure 3.3 (d) shows the results of crack growth rate behavior over a long period of time, involved with substrate damage impact. Initial crack growth rates of 15010 ± 8560 $nm \cdot s^{-1}$, 159 ± 68 $nm \cdot s^{-1}$, 14.1 ± 7.5 $nm \cdot s^{-1}$ and 1.6 ± 0.35 $nm \cdot s^{-1}$ were measured for samples held at applied strain 0.75 %, 0.6 %, 0.55 % and 0.5 %, respectively. For the larger rates, at 0.75 % and 0.6 % applied strains, the cracks grow and quickly reach the edges of the specimen (width: 5 mm), thus the growth rates of different cracks are measured over 100 hours. These rates decreased over the first ~30 - 40 hours until they reached steady-state values of 50.0 ± 13.9 $nm \cdot s^{-1}$, 15.5 ± 5.93 $nm \cdot s^{-1}$, 3.74 ± 1.86 $nm \cdot s^{-1}$ and 1.163 ± 0.394 $nm \cdot s^{-1}$, respectively. In the case of applied strain of 0.5 %, the growth rate is fairly constant. The initial crack growth rates at each applied strain are in the range of the subcritical crack growth rates in *v*-*G* curve (Figure 3.1). Substrate damage keeps developing under channel cracks that have already propagated through the specimen's width, hence varying amount of substrate damage can be present in neighboring cracks.

A possible scenario for the observed long-term crack growth rates can be presented with four cases for samples held at 0.75% (Figure 3.3 (c.1) ~ (c.4)). The crack driving force value was extracted from modeling and the corresponding growth rate was calculated from

the *v*-*G* curve in Figure 3.1. First, a single channel crack develops in SiN_x, *G* value of 14.8 $J \cdot m^{-2}$ was extracted (Figure 3.3 (c.1)), corresponding to a crack growth rate of ~75$\mu m \cdot s^{-1}$. The beginning growth rates in Figure 3.3 (d) are on the same order of magnitude, *i.e.* 15 ± 8.6 $\mu m \cdot s^{-1}$. Since cracks traverse the full width of the specimen in less than a few minutes,

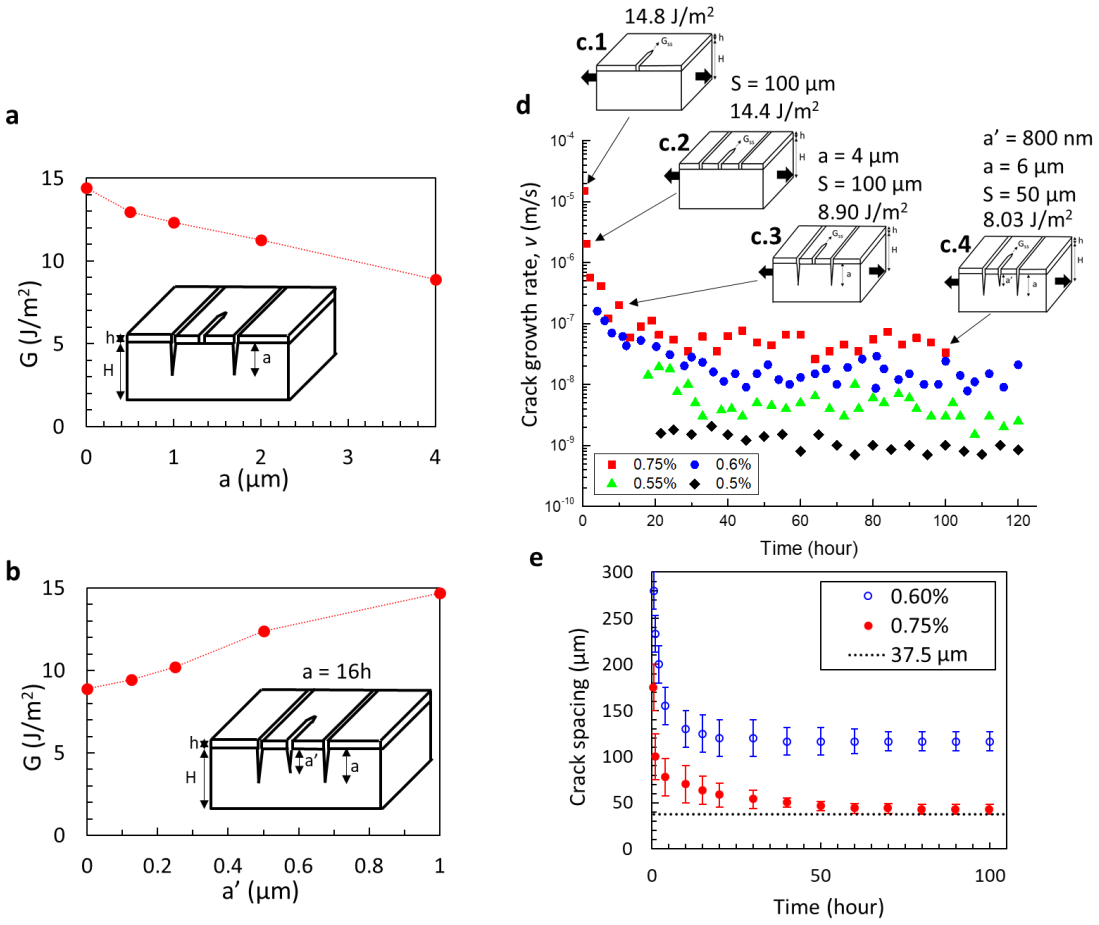

Figure 3.3: (a) Calculated driving force of a crack as a function substrate cracking depth of neighboring cracks. (b) Calculated driving force of a crack as a function of substrate cracking depth a' in the presence of neighboring cracks with a fixed substrate cracking depth a". Both (a) and (b) were calculated under applied strain 0.75%, residual strain -0.15%, cracking spacing 100μm. (c) Schematics of different cracking modes in the SiN_x film and PET substrate, marked with the associated driving force. Crack spacing S, substrate cracking depth in neighboring cracks a", and in growing crack a' are chosen for each case. (d) Measured time dependent crack growth rate of SiN_x/PET in air at 0.5, 0.55, 0.6 and 0.75% applied strain, respectively. The last data point of 0.6% applied strain at 120 hours corresponds to the sample in Fig. 1.c. (e) Crack spacing as a function of time at 0.75% and 0.6%, respectively.

for example, 1 ~ 5 mins for 15 ~ 75 μm·s^{-1}, multiple interacting cracks are observed. So, after 1 hour, channel crack growth with reduced crack spacing was expected to be the second case (Figure 3.3 (c.2)), the driving force was reduced to 14.4 J·m^{-2} with adding two adjacent cracks, corresponding to a slight decrease in crack growth rates ~50 μm·s^{-1}. Until the second case was analyzed, substrate damage was not observed in the PET as shown in the SEM image at strain 0.75% in Figure 1.5 (a). However, over time, substrate cracking develops first in the existing cracks, and the new growing cracks have a lower driving force due to the effect of substrate cracking in the neighboring cracks (Figure 3.3 (a)), corresponding to the third case in Figure 3.3 (c.3). For example, the crack driving force was further reduced to 8.9 J·m^{-2} when a 4 μm crack was present in the PET under the neighboring cracks (Figure 3.3 (c.3), crack spacing, S, of 100 μm), corresponding to the growth rate of ~119 nm·s^{-1} which is commensurate with the measured rate after 10 hours (see Figure 3.3 (d)). Last scenario is when a steady-state growth rate (~50 - 100 nm·s^{-1}) is observed (Figure 3.3 (d)) after ~30 - 40 hours. Since it took more than 20 hours for cracks to traverse the specimen's width, growing cracks also undergo substrate cracking (Figure 3.3 (c.4)). Now the driving force is the result of a balance between additional substrate cracking in the growing crack, *i.e.* increase of driving force (Figure 3.3 (b)), and in the adjacent cracks, *i.e.* decrease of driving force (Figure 3.3 (a)). For example, with 800 nm substrate cracking underneath the growing crack and 6 μm neighboring penetration into PET, the driving force is calculated to be 8.03 J·m^{-2}, similar to the value achieved in the third case.

3.2.3 Impact of Environmental Conditions on Growth Rate for Interacting Cracks

The effect of environmental condition on the long-term crack growth rate behavior was studied by performing experiments in dry nitrogen for long periods of time and then switching to laboratory air. Figure 10 shows that crack growth rate evolution for a specimen tested in air at ε_{app} = 0.75% along with the specimens tested at the same applied strain in dry nitrogen before switching to laboratory air after either 20 or 60 hours.

In dry N_2, the initial crack growth rate is two orders of magnitude lower than in the humid air, highlighting environmentally-assisted cracking. Also, the magnitude of decrease in growth rates until reaching to steady-state value after ~20 hours is much less than in air. This is attributed to the fact that the density of cracks in N_2 is two orders of magnitude lower than in air and therefore the lack of interacting cracks can be expected. Because of the very low density of cracks that formed in N_2, after switching to humid air, a large increase in the crack growth rate was observed due to the impact of environmentally-assisted cracking, rising in both cases to rates similar to the initial rates for samples tested in humid air, behaving like a fresh specimen tested in air. Lastly, Figure 3.4 shows that the steady state rates in N_2 are only one order of magnitude lower than that in air, while the initial rates were two orders of magnitude lower. The lower relative decrease in nitrogen is expected either due to the lower density of cracks in that environment leading to lower decreases in driving force or the humid environment induces more substrate damage that could lead to larger relative decreases in air.

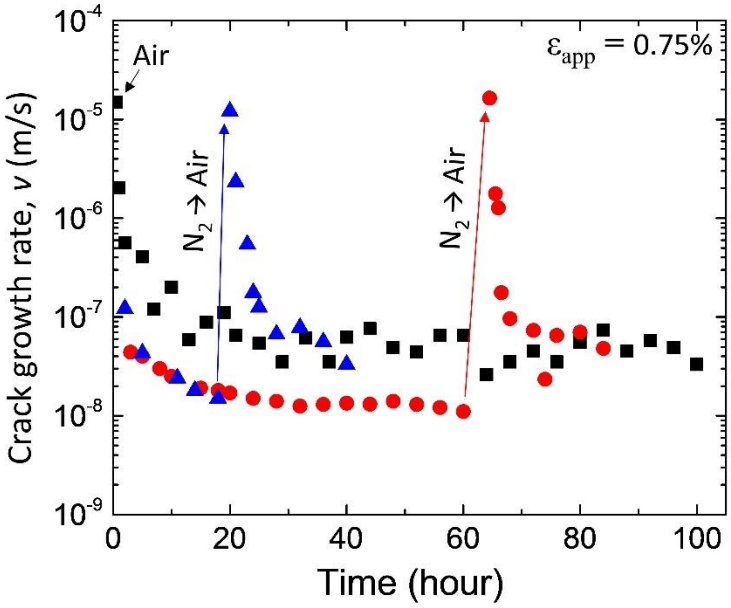

Figure 3.4: Crack growth rate behavior of SiN_x / PET at 0.75% applied strain in environmental condition change.

3.2.4 Crack Growth Rate Behavior Comparison between PET vs. PI

Polyimide (PI) substrate has a higher tensile strength (PI: 340 MPa, PET: 170 MPa by ASTM D882) than PET substrate and resistance to hydrolysis and thus should have greater resistance to substrate damage. The long-term crack growth rates in SiN_x on PI are expected to be different from that of PET, under same initial channel crack driving force. The moduli of elasticity of SiN_x and polymer substrates were determined by nanoindentation and uniaxial tensile testing, respectively (PI was found to be 7.6 ± 0.17 GPa, higher than PET which has found to be 4.07 ± 0.12 GPa). The elastic mismatch between SiN_x and PI was $\alpha = 0.880$ and between SiN_x and PET was $\alpha = 0.934$, corresponding to dimensionless energy release rates Z of 8.62 and 11.8, respectively. Residual strains were found to be -0.15% for both PI and PET. To test a SiN_x specimen on

PI with the same initial G value with that of PET, a higher applied strain, *i.e.* 0.1%, was required for PI samples, *i.e.* 0.85%, to match the crack driving forces between PI (13.8 $J \cdot m^{-2}$) and PET (14.4 $J \cdot m^{-2}$), less than 5% difference in the initial driving force. Figure 3.5 (a) shows that the decrease in crack growth rate with time for SiN_x / PI is much less than that of SiN_x / PET. In SEM images (Figure 3.5 (b)), substrate cracking was not detected in both of PI and PET after one hour. However, after 2 days, substrate cracking was observed in the PET as expected, whereas PI was still free from substrate damage. A little decrease in crack growth rate of SiN_x / PI presumably came from inherent damage on the top surface of the substrate. When both of the substrates are under the same value of applied strain, the number of cracks in SiN_x / PI is greatly less than that of SiN_x / PET (after 2 days of testing, 255 ± 32 cracks accumulated in SiN_x / PET while 21 ± 5 cracks were accumulated in SiN_x / PI). This certainly demonstrates that depositing barriers on substrates with high tensile strength and resistance to hydrolysis effectively improve the reliability of barrier films under long-term mechanical loading.

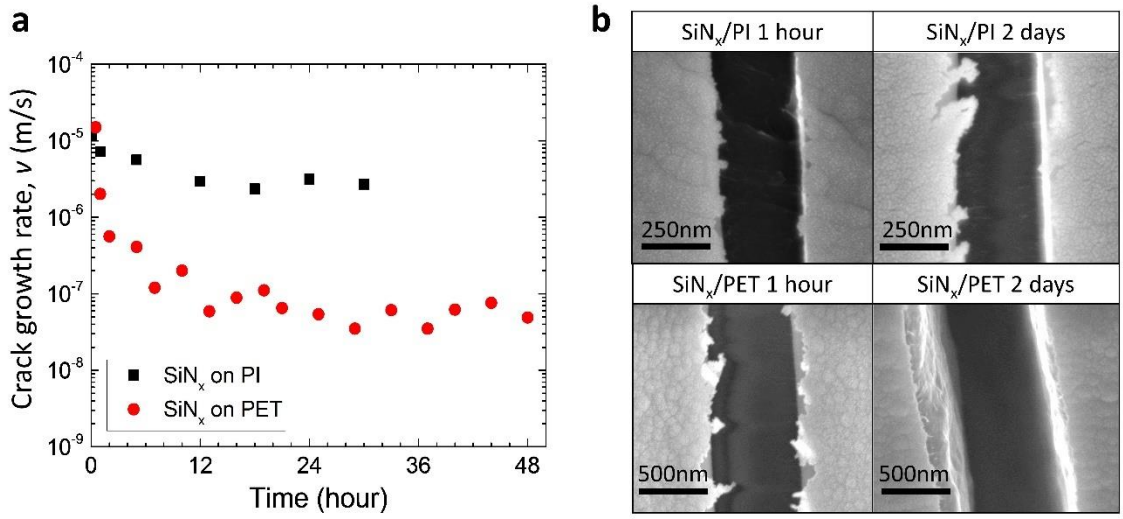

Figure 3.5: (a) Time dependent crack growth rate behavior of SiN_x deposited on PET at the applied strain 0.75% versus on PI at the applied strain 0.85%. (b) SEM images of SiN_x / PET and SiN_x / PI after 1 hour and 2 days passed, respectively.

3.3 Summary and Conclusions

Long-term behavior of environmentally-assisted subcritical cracking of PECVD SiN_x barrier films on PET and PI substrates was investigated by measuring the evolution of crack growth rates under fixed strain as a function of time using in-situ microscopy. While channel cracking in SiN_x are observed over short periods of time (< 1 hour), longer straining experiments are associated with a regime where cracking also developed in the substrate. This study highlights the combined effects of neighboring cracks and substrate cracking on the resulting crack growth rate evolution. In most cases, the subcritical crack growth rates decrease over time by up to 2 orders of magnitude until steady-state rates are reached. However, increases in growth rate with time can be obtained in certain conditions (isolated cracks with increasing substrate damage). For SiN_x on PI, crack growth rates were found to be more stable over time due to the lack of crack growth in the substrate as compared to SiN_x on PET. These results provide a guideline to effectively improving the long-term reliability of thin film barriers for flexible electronics applications by a substrate possessing high strength with limits substrate damage.

CHAPTER 4. ALD CAPPING LAYER AND STOICHIOMETRY EFFECT ON EAC IN PECVD SiN_x BARRIER FILMS

4.1 ALD Capping Layer Effect on Environmentally Assisted Cracking in PECVD SiN_x Barriers

A strong impact of environmental exposure from water vapor was seen on the growth of cracks in the SiN_x films.[1-2] This previous study revealed that, as a result of EAC in the SiN_x films, extensive channel cracks can be developed at strain levels 35% below the COS.[2] Thus, EAC is central to the failure of ultrabarrier films exposed to mechanical deformation. This leaves the question as to whether or not the fracture behavior of PECVD SiN_x films can be improved through the use of methods that may limit its exposure to moisture and oxygen?

This section focuses on a specific issue: the impact of capping layers on the fracture behavior of PECVD SiN_x ultrabarrier films. The purpose of the capping layer is to limit the exposure of the underlying SiN_x to environmental oxygen and moisture. To reduce the impact of the environment of the SiN_x barriers, Al_2O_3 capping layers produced by atomic layer deposition (ALD) and immune to EAC (as demonstrated below) were used on top of the SiN_x film. It should be noted that ALD Al_2O_3 degrades in moist conditions, but EAC was not observed in the air; therefore, it is applicable in this study. The ALD Al_2O_3 investigated thicknesses, 2 and 10 nm, are more than one order of magnitude less than the 250-nm SiN_x layer, such that their COS on PET is higher than that of the SiN_x layer (the COS of 10-nm-thick Al_2O_3 on PET is 1.48% while the COS of 250-nm-thick SiN_x on PET

is 0.95%). However, as will be shown below, the effect of the capping layer, having larger COS, does *not* necessarily mean an increase in the COS of the bilayer film.

4.1.1 Sample Preparation and Experimental Procedure

To create the samples, heat-stabilized 125 μm thick PET (Dupont Teijin Films Melinex ST505) substrates used for the barrier films. The PET substrates were laser cut prior to deposition to a size of 5 mm by 50 mm. Then, 250 nm PECVD SiN_x films (Unaxis PECVD system with radio frequency (rf) parallel plate configuration) were deposited on the PET at a temperature of 110 °C, pressure of 1 Torr, 20 W rf plasma and a rate of 10 nm/min. ALD films were deposited in a Cambridge Fiji Plasma ALD system from Cambridge Nanotech Inc. Trimethyl aluminum (TMA) and oxygen plasma were used as precursors for Al_2O_3 with nitrogen (N_2) as the purge gas. In each deposition cycle, the pulse and purge times for TMA were 0.06 s and 60 s, respectively, and oxygen plasma was used for 20 s with the plasma power of 300 W. The N_2 flow rate was maintained at 20 sccm throughout the deposition. The growth rate for Al_2O_3 was ~1.2 Å per cycle. The deposition was performed at 100 °C, for two thicknesses of 2 nm and 10 nm.

In-situ optical and laser confocal microscopy (Olympus LEXT, OLS4100) was used to observe the subcritical crack growth on the surface of PECVD SiN_x film with and without the ALD Al_2O_3 capping layer using a microtensile testing stage (Linkam Scientific Instruments, TST350). The external-load assisted technique (see section 2.2.2) was applied for channel crack growth rate measurement by pulling the samples to a strain of 0.75% to nucleate cracks, followed by a quick strain reduction to obtain full *v*-*G* curve. The threshold driving force, G_{th}, for EAC was obtained by determining the strain at which no crack

extension (within the ~1μm detection resolution) could be observed within 30 minutes, corresponding to v less than 0.55 nm.s^{-1}. Tests were performed in a controlled environment consisting of dry nitrogen (moisture content of 2 ppm), as well as laboratory air in room temperature.

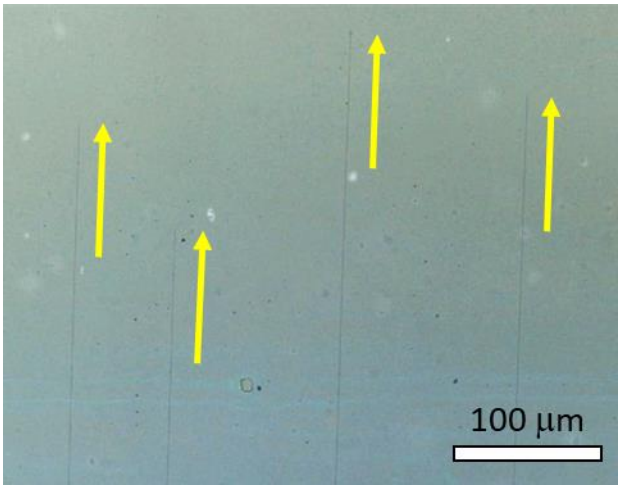

Figure 4.1: Optical images during tensile test, straining in the horizontal direction and thus subcritical channel crack growths appeared in the vertical direction.

4.1.2 Effect of Thickness and Residual Stress of ALD Capping Layer on Z and Crack Onset Strain

To calculate the driving force, G, in a two-layered structure, *i.e.*, Al_2O_3 / SiN_x / PET, the modeling method created by Long *et al.* was reproduced.[56] 2D plane strain linear elastic finite element models were used in ABAQUS 6.13.[70] Identical dimensions of the specimens tested in experiment were used to create the model geometry. Materials were assumed to behave linear elastically, and the crack opening displacement, δ, was extracted in order to numerically integrate the stress and obtain the value of G in Eq. 8. Three different channel cracking modes were numerically investigated (cracking only in the SiN_x

layer, cracking only in the Al_2O_3 surface layer, and cracking of the bi-layer). In the case of cracking only in the SiN_x layer, COS was calculated as 1.62% and 1.80% for a 2nm and 10 nm Al_2O_3 capping layer, respectively. In the case of cracking only in the Al_2O_3 surface layer, COS was calculated as 8.91% and 4.36% for a 2nm and 10nm Al_2O_3 capping layer, respectively. These large strain values are due to the presence of the SiN_x underneath (much thicker than Al_2O_3) that leads to a large decrease in Z for this cracking mode. Therefore, the channel cracking of the bi-layer corresponds to the lowest COS values and is the expected cracking mode corresponding to the crack observations in Figure 4.1.

The experimentally measured mechanical parameters outlined by Herrmann *et al.*[117], Ylivaara *et al.*[118] were used in addition to the previously measured parameters in section 2.1.1.[2] Young's modulus and Poisson's ratio were taken to be E_a = 150 GPa, ν = 0.23 for Al_2O_3 layer[117], E_f = 123 GPa, ν = 0.253 for the SiN_x layer[2], and E_s = 4.07 GPa, ν = 0.3 for the PET substrate.[2] Nanoindentation was used to measure the modulus of the SiN_x film E_f. The uniaxial tensile properties of the PET substrates were obtained using the microtensile stage. The residual stress of Al_2O_3 film is taken to be σ_a = 385 MPa, the summation of intrinsic residual tensile stress, *i.e.,* 550 MPa[29, 118], and the residual compressive stress from the CTE mismatch, *i.e.,* 165 MPa. CTE values of 4.2×10^{-6} K^{-1} for Al_2O_3 films[38] and 19×10^{-6} K^{-1} for PET substrates were used. The residual stress of the SiN_x film was taken to be σ_f = -185 MPa.[2] Figure 4.2 shows the effective Z value, Z_{eff}, calculated based on the numerical G values (Eq. 8) and using Eq. 1 that only considers the SiN_x layer, as a function of capping layer thickness, with and without including the residual stresses. This graph highlights the importance of considering residual stresses for accurately calculating G. More specifically, it shows an increase in Z_{eff} (and therefore G)

of 10% (from 12 to 13.2) when adding the 10-nm Al_2O_3 capping layer and considering residual stresses, whereas it would only be 6% (from 10.4 to 11) if ignoring residual stresses.

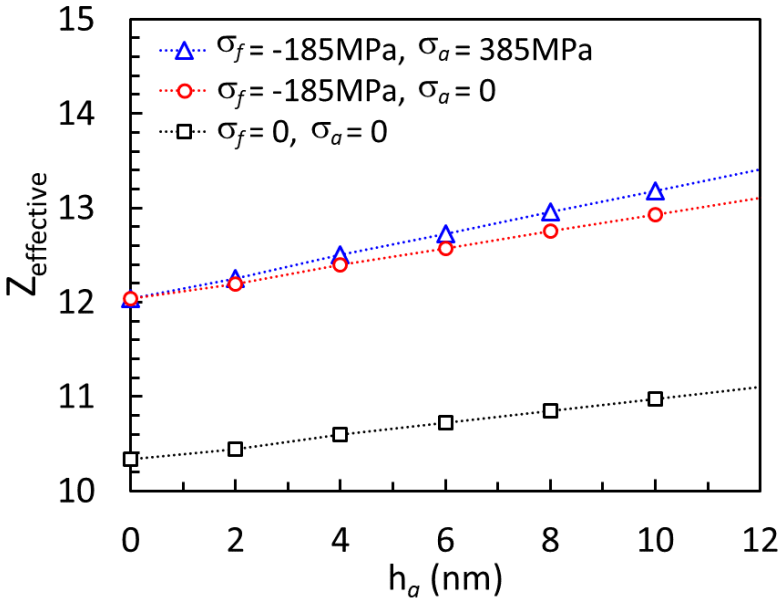

Figure 4.2: Z as a function of capping layer thickness in an all-through crack failure mode. Residual stresses are included in order to compare their effect on Z.

Figure 4.3 shows the experimental measurements of COS (corresponding to the applied strain, ε_{app}, in Eq. 1 at the onset of channel cracking) as a function of capping layer thickness, h_a. The presence of a 10 nm capping layer results in a 5% decrease in COS (from 0.95 to 0.9%), while there is no noticeable decrease with the 2 nm layer. Figure 4.3 also shows the predicted COS for the bilayer film, as a function of h_a. These predictions were based on Eq. 1 (with Z_{eff} shown in Figure 4.2) and the calculated fracture energies for SiN_x and Al_2O_3, Γ_f and Γ_a, respectively. Based on a COS of 1.48% for 10 nm Al_2O_3 on the PET, Γ_a was calculated to be 6.4 $J \cdot m^{-2}$ (using similar finite element models), corresponding to a fracture toughness, K_{Ic}, value of 1.01 $MPa \cdot m^{1/2}$. Γ_f was previously found to be 25.2 $J \cdot m^{-2}$,

corresponding to a K_{Ic} value of 1.82 MPa·m$^{1/2}$.[2] The fracture energy of the bilayer film can be calculated as an average fracture energy:[56]

$$G_c = (\Gamma_f h_f + \Gamma_a h_a)/(h_f + h_a) \quad (13)$$

The model is consistent with the experimental results, predicting a 5-6 % decrease in COS with the presence of the 10 nm capping layer, which is the combined result of a 10 % increase in Z_{eff} (See Figure 4.2) and a 3 % decrease in G_c (24.5 J·m^{-2} for h_a = 10 nm vs 25.2 J·m^{-2} for h_a = 0). This decrease in COS may appear counterintuitive given that the COS of 10 nm Al_2O_3 on PET is much higher (1.48%, *i.e.*, a stronger capping layer). In fact, the actual decrease implies that the presence of the capping layer does not affect the nucleation of channel cracks from pre-existing defects in the SiN_x layer; once a defect grows into a channel crack in the SiN_x, the presence of the capping layer does not prevent its propagation (it actually makes it easier due to the increase in G shown in Figure 4.2).

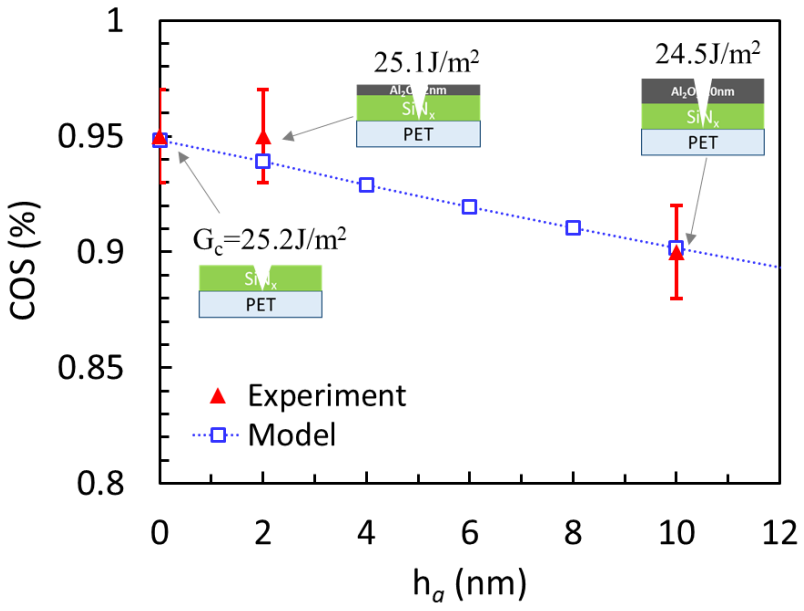

Figure 4.3: COS as a function of capping layer thickness.

4.1.3 *Effect of ALD Capping Layer on Environmentally Assisted Cracking*

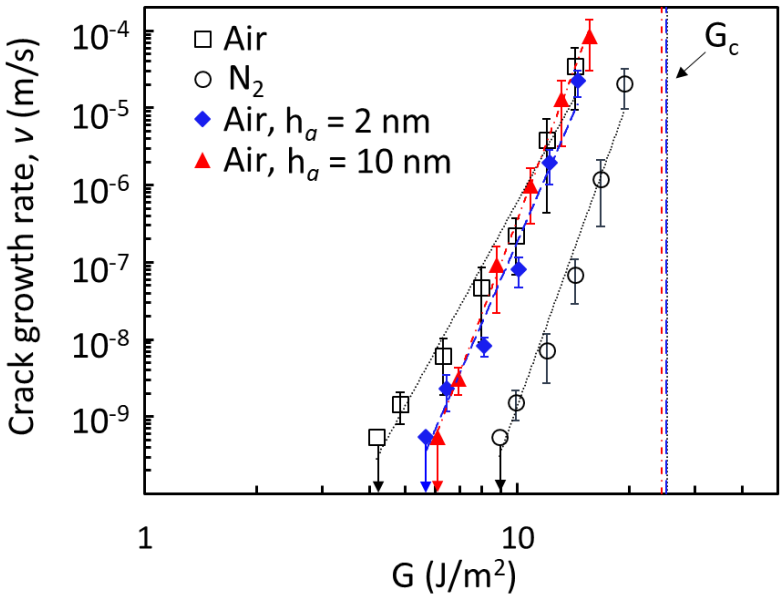

Figure 4.4: The measured crack growth rate as a function of the driving force *G* (*v*-*G* curve) for a channel crack in a 250 nm thick SiN_x film in both the air and dry N_2, and a 2 nm and 10 nm Al_2O_3 capping layer deposited on the 250 nm SiN_x film surface.

Figure 4.4 displays the *v*-*G* curves for 250-nm-thick SiN_x films on PET at room temperature in air and dry N_2 environments. The difference in the two data sets indicates EAC in the SiN_x films.[1-2] The graph also shows the *v*-*G* curves in air for the SiN_x films with the 2 and 10 nm Al_2O_3 capping layers. The error bars of empty and solid symbols represent the standard deviation from average rates calculated over 10 and 5 measured growing cracks, respectively.[1] Most of the solid data points are within the error bars of the empty square data points. Hence, the capping layer is not much effective in preventing EAC of the underlying SiN_x, even though EAC was not observed on ALD Al_2O_3 deposited on PET. (Specifically, the external-load assisted technique[1] was applied for 10-nm-thick Al_2O_3 on PET from COS of 1.48% to an applied strain of 1.3% in air, corresponding to $G = 5.1\ J{\cdot}m^{-2}$ and thus $G/G_c = 0.8$. No further growth of channel cracks was observed in the

Al_2O_3 films, corresponding to crack growth rates below 0.55 nm·s^{-1}, while crack growth rates of > 50 μm·s^{-1} were measured in SiN_x on PET at the same value of G/G_c.) One possible explanation is that, since the failure mode is through-thickness cracking of the bilayer, the cracked capping layer does not prevent water and oxygen molecules from reaching the crack tip in SiN_x at large driving forces. However, Figure 4.4 reveals for the capped SiN_x larger threshold driving force values G_{th}, below which no EAC is observed within the resolution of the technique (< 1 μm crack growth in 30 minutes, corresponding to v < 0.55 nm·s^{-1}). For SiN_x alone, G_{th} = 0.17 G_c (or, in term of stress intensity factor, K_{th} = 0.41 K_c), whereas for SiN_x with the 2 nm (resp. 10 nm) Al_2O_3 capping layer, G_{th} = 0.225 G_c (resp. G_{th} = 0.25 G_c), or equivalently, K_{th} = 0.47 K_c (resp. K_{th} = 0.5 K_c). Given that the threshold regime is often associated with steric hindrance of the environmental species, it is possible that the 30-50% improvement in G_{th} is related to a beneficial effect of the capping layer in further preventing access of water molecules to the crack tip in SiN_x at these low applied driving forces. This comes from the increase of threshold strain ε_{th} from 0.5% (*i.e.* ε_{th} of SiN_x films) to 0.55% (*i.e.* ε_{th} of both 2 nm and 10 nm Al_2O_3 layers on SiN_x films) measured in the experiment.

The main reason for the lack of significant effect of the alumina capping layer on reducing EAC in SiN_x is the fact that the dominant failure mode is cracking of the bi-layer. This is confirmed in Figure 4.5 showing the lowest predicted COS for this failure mode over the other two possible modes for the whole investigated capping layer thickness regime. In order to have an effective capping layer preventing exposure of SiN_x to the environment, the lowest COS needs to be associated with the cracking of the SiN_x only. A parametric study showed that this is only the case by considering an organic capping layer

with a low modulus (E_a = 1.5 GPa) and high fracture energy (Γ_a = 100 J·m^{-2}). With these parameters an increased Z (due to the increase in elastic mismatch) between the capping layer and SiN_x results in decreased COS for cracking only in the SiN_x layer. At the same time, as the thickness of capping layer increases, the high fracture energy of the capping layer increases the average fracture energy. Thus, the COS of the bi-layer increases while COS for cracking only in the SiN_x layer stays unchanged. As a result, cracking only in SiN_x layer becomes the dominant failure mode at ~1.35 % when the thickness of capping layer, h_a, is larger than 95nm (see Figure 4.6). Given the large Γ_a, cracking of the capping layer only is the dominant failure mode for capping layers thicker than ~200 μm. Although organic films have typically poor WVTR on the order of 1 g·m^{-2}·day^{-1}[14, 19] (*e.g.*, PET substrate used in this work shows 4, 2.9, and 0.86 g·m^{-2}·day^{-1} for 125, 175, and 250 μm thick films at 38 °C / 90% rh, respectively), thick (*e.g.* up to 200 μm) capping layers could be used in reducing EAC in SiN_x by delayed exposure of SiN_x to the environment.

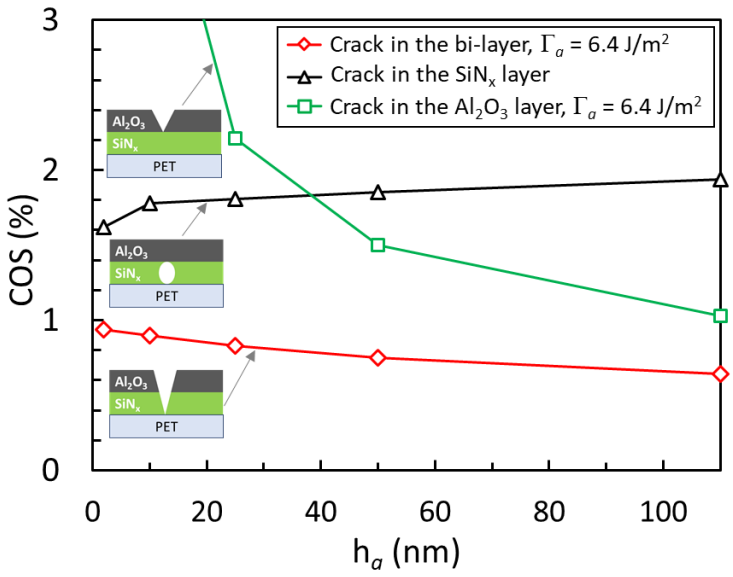

Figure 4.5: COS of all possible channel cracking modes in Al_2O_3 / SiN_x / PET as a function of capping layer thickness. SiN_x thickness is 250 nm.

Additionally, these thick layers may act as a protective layer from mechanical abrasion for the hard barrier layer underneath.

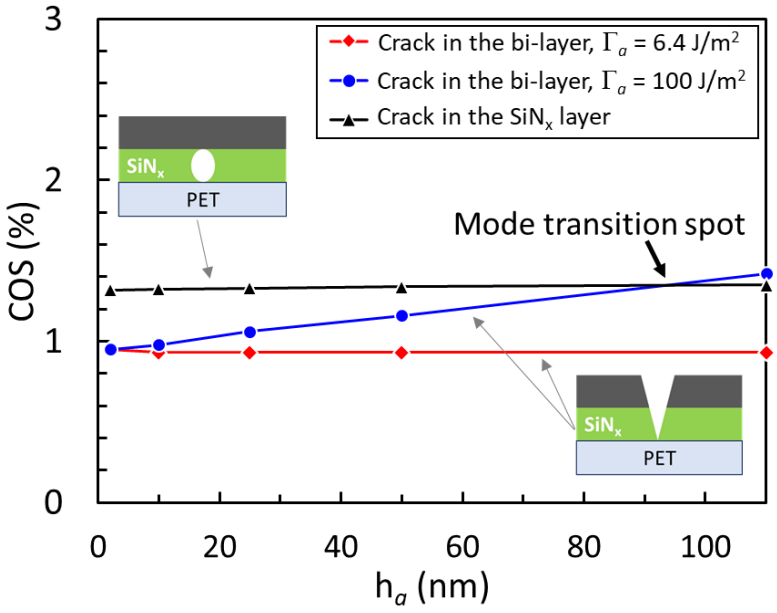

Figure 4.6: COS of all possible channel cracking modes in SiN_x / PET with an organic capping layer on top surface as a function of the capping layer thickness. E_a = 1.5 GPa and Γ_a = 100 J·m^{-2} were applied.

4.2 Stoichiometry Effect on Environmentally Assisted Cracking in PECVD SiN_x Barriers

In this section, various ratios of silicon (Si) to nitrogen (N) were developed and fabricated by controlling the ratio of SiH_4 to NH_3. According to a study by Huang *et al.*,[78] deposition conditions can significantly influence a Si:N ratio and the mechanical properties of low-temperature PECVD SiN_x films. The strong relationship between the modulus of elasticity and the density of films, in addition to the relationship between Si:N ratios and the density of films that was illustrated in Huang *et al.*'s work,[78] suggests that the

mechanical properties of each and every type of SiN_x sample requires characterization. Tests should therefore be performed to obtain subcritical crack growth rates (*e.g., v-G* curves) and to determine the stoichiometry effect on EAC in PECVD SiN_x barriers. Ultimately, this study aims to assess PECVD SiN_x and to create mechanically reliable barrier films that can effectively broaden usability under harsher mechanical and environmental conditions.

4.2.1 Experimental Characterization on Mechanical Properties

PECVD SiN_x films of several ratios between Si and N were fabricated by varying the flow rates of an ammonia (NH_3) gas pump to 1, 6, 10, 14, 18, and 22 sccm and by fixing the flow rate of a silane (SiH_4) gas pump to 10 sccm. Every other processing condition was set to the same parameters (*e.g.*, 250 nm of PECVD SiN_x; Unaxis PECVD system with radio frequency (rf) parallel plate configuration) at a temperature of 110 °C, a pressure of 1 Torr, 20 W rf of plasma, and a rate of 10 $nm \cdot min^{-1}$ on laser-cut prior heat-stabilized 125 μm thick PET (Dupont Teijin Films Melinex ST505) substrates.[2]

The XPS characterization, which was performed to find the chemical composition and atomic percentage of the fabricated SiN_x, is shown in Figure 4.7 and in Table 4.1. As an example, SiH_4:NH_3 ratio of 10:14 in Table 4.1 illustrates that through the XPS spectra, the total atomic percentage of Si was 44.56%. In addition, while 95.6% of this Si was bonded to N, 4.4% was bonded to hydrogen (H). Oxygen (O) was also found in the bulk SiN_x film and was suspected to be incorporated via the diffusion of O and water vapor through pores upon exposure to the atmosphere during the deposition process. The atomic percentages of N and O were 53.32 % and 3.12%, respectively. The ratio of Si: N (1:1.228)

and the refractive index that was determined for the SiN_x with ellipsometry were similar to those that have been calculated in existing literature.[120-121] The NIST reference binding energies were used to determine the composition of PECVD SiN_x. As a result, ratios of N to Si were obtained in PECVD SiN_x films that ranged from 1:1.495 to 1.1.098 (Figure 4.8).

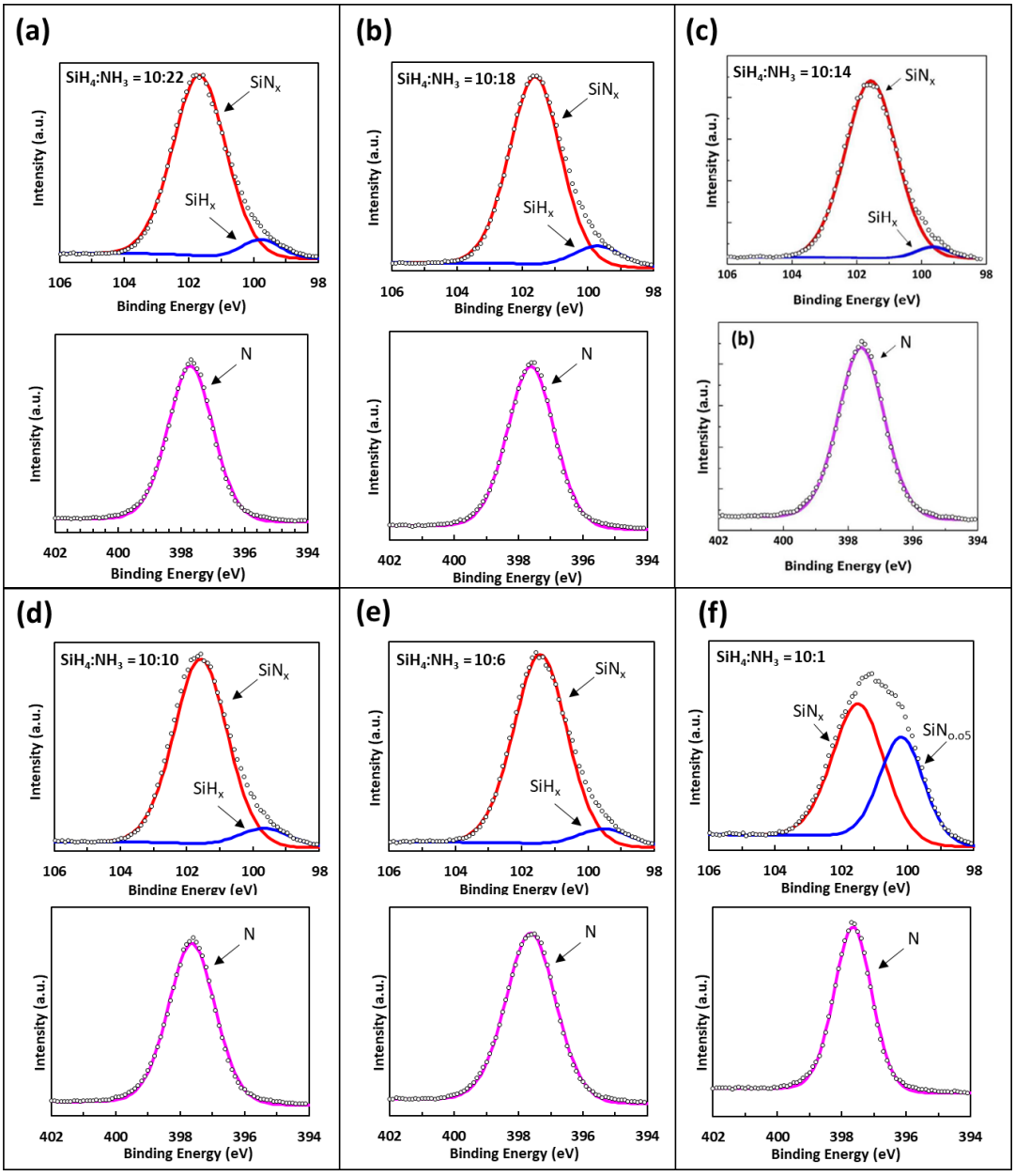

Figure 4.7: XPS data on the Si2p peak of PECVD silicon nitride, showing that the Si-N peak was dominant with a small presence of Si-H in the bulk of the sample (upper plot). XPS data also reveals the N1s peak (lower plot). The SiH_4:NH_3 ratios are as follows: (a) 10:22, (b) 10:18, (c) 10:14 (reference), (d) 10:10, (e) 10:6, and (f) 10:1.

In the case of the sample, which had SiH_4:NH_3 ratio of 10:1, the chemical composition was found to be a combination of two different SiN_x films: 62% of 1:1.615 and 38% of 1:0.05.[122]

Table 4.1: XPS data on the chemical composition, and the atomic percentage of PECVD SiN_x with SiH4:NH3 ratios of 10:22, 10:18, 10:14 (reference), 10:10, 10:6, and 10:1.

SiH_4:NH_3	Element	at. %	Phases	B.E. (eV)
10:22	Si	44.56	SiN_x (72.2%), SiH_x (27.8%)	101.56 (SiN_x), 99.65 (SiH_x)
	O	3.12		
	N	48.09		
10:18	Si	47.42	SiN_x (75.4%), SiH_x (24.6%)	101.56 (SiN_x), 99.65 (SiH_x)
	O	3.66		
	N	48.92		
10:14 (ref.)	Si	44.56	SiN_x (95.6%), SiH_x (4.4%)	101.56 (SiN_x), 99.65 (SiH_x)
	O	3.12		
	N	52.32		
10:10	Si	48.20	SiN_x (91.2%), SiH_x (8.8%)	101.56 (SiN_x), 99.65 (SiH_x)
	O	3.46		
	N	48.34		
10:6	Si	48.22	SiN_x (91.2%), SiH_x (8.8%)	101.56 (SiN_x), 99.65 (SiH_x)
	O	3.50		
	N	48.28		
10:1	Si	48.14	SiN_x (62.25%), $SiN_{0.05}$ (37.75%)	101.56 (SiN_x), 100.11 ($SiN_{0.05}$)
	O	3.47		
	N	48.39		

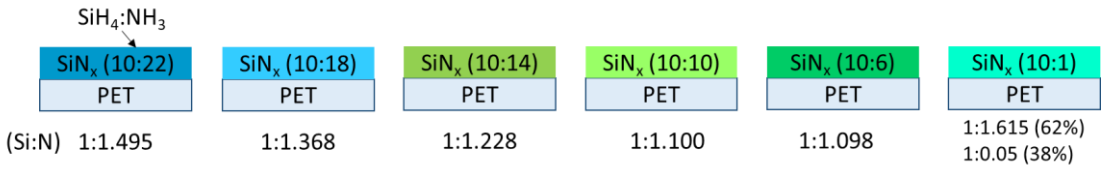

Figure 4.8: Schematics of the PECVD SiN_x samples, fabricated by SiH_4:NH_3 ratios of 10:22, 10:18, 10:14, 10:10, 10:6, and 10:1, with the Si:N found to be 1:1.495, 1:1.368, 1:1.228, 1:1.100, 1:098, and 62% of 1:1.615 and 38% of 1:0.05, respectively.

To plot *v*-*G* curves, each component value of the driving force *G* (see Eq. 1.) should be obtained. First, the film's COS, ε_c, and residual strain, ε_{res}, were measured using an in-situ optical microscopy tensile test. All samples of the COS and residual strain were found to be 0.95 ± 0.05 % and -0.15 ± 0.02 %, respectively, which are equal to those that were determined in the reference sample (except slightly larger standard deviation of COS for the 10:1 ratio of SiH_4:NH_3, *i.e.*, 0.95 ± 0.10 %). The elastic modulus of the film was measured using nanoindentation (Hysitron triboindenter) equipped with a diamond Berkovich tip and displacement resolution of <1nm. A depth of ~300 nm was indented in a 1 μm thick SiN_x film that had been deposited on a Si-wafer. Table 4.2 shows the elastic modulus that was achieved for each sample within the same range (~120 GPa) except the 10:1 ratio of SiH_4:NH_3. For all samples but the 10:1 ratio of SiH_4:NH_3 (Z = 13 ± 3.0) and the 10:6 ratio of SiH_4:NH_3 (Z = 11.2 ± 2.1), the dimensionless energy release rate Z was calculated to be 11.8 ± 2.2. Thickness of the film was measured with an ellipsometer (Wollam M2000 ellipsometer) (see Table 4.2). Thickness started to increase when the flow rates of the ammonia (NH_3) gas pump were set to 10, 6, and 1 sccm, which were all less than the reference sample's NH_3 gas pump flow rate of 14 sccm. This indicates that there

were deposition rates of ~10 nm·min^{-1} for the SiH_4:NH_3 sample ratios of 10:22 and 10:18, which was the same as the reference sample's deposition rate, and 11, 12, and 15 nm·min^{-1} for the SiH_4:NH_3 sample ratios of 10:10, 10:6, and 10:1, respectively. The refractive index of the SiN_x films were also measured at 632.8 nm. As a result, the driving forces at COS (*i.e.* the critical energy release rate, G_c, and thus fracture energy, Γ) were calculated to be 24.1 ± 5.1, 24.5 ± 5.2, 27.6 ± 5.8, 26.0 ± 5.6, and 51.7 ± 15.4 J·m^{-2} for the SiH_4:NH_3 sample ratios of 10:22, 10:18, 10:10, 10:6, and 10:1, respectively. A G_c value of 25.2 ± 5.4 J·m^{-2} was determined in the reference sample.

Table 4.2: The thickness, refractive index, and modulus of elasticity for PECVD SiN_x samples, fabricated by SiH_4:NH_3 ratios of 10:22, 10:18, 10:14, 10:10, 10:6, and 10:1.

SiH_4:NH_3	10:22	10:18	10:14 (ref.)	10:10	10:6	10:1
h (nm)	247 ± 0.6	255 ± 0.9	254 ± 1.0	278 ± 0.8	303 ± 1.0	366 ± 0.3
n @ 632.8nm	1.75	1.77	1.77	1.81	1.87	2.15
E (GPa)	121 ± 4.1	119 ± 3.8	123 ± 5.8	123 ± 3.1	112 ± 5.3	159 ± 26

4.2.2 Quantification of Environmentally Assisted Cracking in PECVD SiN_x Films with Variations in Stoichiometry

The external load assisted channel crack growth technique (section 2.2.2) was applied to quickly obtain the *v*-G curves for the SiH_4:NH_3 sample ratios of 10:6, 10:10, 10:18, and 10:22. Then, these *v*-G curves were compared with those from the reference sample (the SiH_4:NH_3 ratio of 10:14), previously quantified (see chapter 2). Because its properties deviated significantly from the referenced PECVD SiN_x films (see Table 4.2), the SiH_4:NH_3 sample ratio of 10:1 was excluded from measurements of the crack growth

rate. Figure 4.9 shows that the crack growth rates of the sample ratios between 10:6 and 10:22 (empty symbols) were bounded by the standard deviation of the reference sample (solid square symbols). In addition, thresholds for G_{th} were found to be 4.6 ~ 5.3 J·m^{-2}. These values came from the threshold strain, ε_{th}, of 0.5%, which was measured for all samples with a resolution of 0.025%, illustrating the indistinguishable differences between the threshold for all samples.

A two-stage reaction may occur in the PECVD system consisting of the silane (SiH_4) and ammonia (NH_3) gas mixture as the source of Si and N: 1) $SiH_4 + 4NH_3 \rightarrow Si(NH_2)_4 + 4H_2$ (by plasma), and 2) $3Si(NH_2)_4 + 12H_2 \rightarrow Si_3N_4 + 8NH_3$ (by heat).[123] The lower temperature films (deposited at 110 °C) used in this study are believed to contain some fraction of hydrogen from incomplete dissociation of $Si(NH_2)_4$ during stage two. Thus, Si bonded to hydrogen were detected with variations from 4.4 to 27.8% (Table 4.1). These

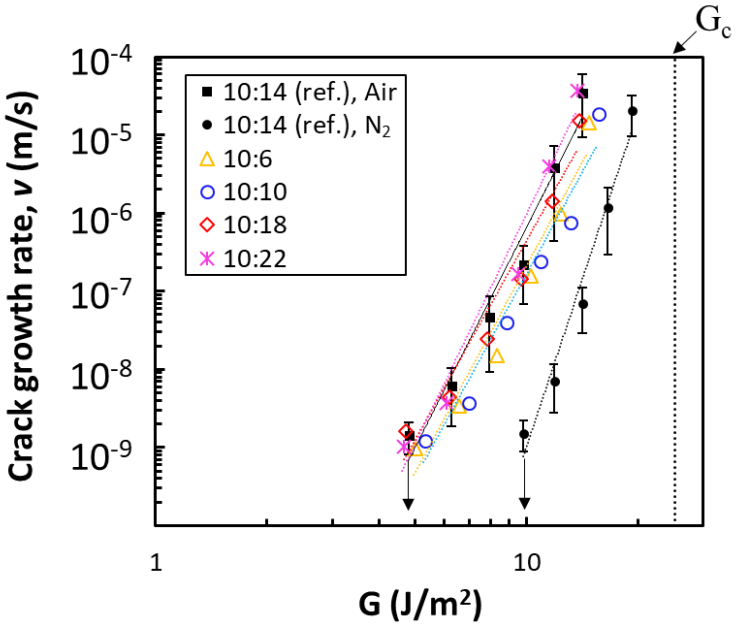

Figure 4.9: *v*-G curves of the 10:6, 10:10, 10:18, and 10:22 ratios for the SiH_4:NH_3 samples (empty symbols), which were measured in air, and the reference sample (10:14 ratio of SiH_4:NH_3) (solid symbols), measured both in air and nitrogen. All samples were measured at 25 °C.

variations may not be enough to change the most energy-favored spot for bond breaking described as the EAC mechanism in section 2.3, Figure 2.10. Also, density changes from the reference sample could be calculated by applying the linear relationship between density and the Si:N ratio presented by Huang *et al.*[78] Note that a less than 10% change in density was calculated (*i.e.* 3.3 - 2.8 Mg/m^3 for 1:1.098 - 1:1.495 of Si:N) from reference (*i.e.* 3.1 Mg/m^3 for 1:1.228 of Si:N). Therefore, all are expected to follow the EAC mechanism described in section 2.3, containing the same energy-favored spots for bond breaking between Si and N (see Figure 2.12 (d)).

4.3 Summary and Conclusions

In section 4.1, ALD Al_2O_3 capping layers were used on PECVD SiN_x barrier films in order to illustrate alteration in EAC behavior. While crack growth rates were not greatly reduced, thresholds of driving force G_{th} were increased as a result of reduced EAC effects due to the capping layer. In a parametric study, the results show that a high fracture energy, low elastic modulus capping layer can cause a transition of the failure mode to cracking only in SiN_x layer. With the help of this capping layer, we can expect protection from EAC degradation during mechanical loading.

Section 4.2 accessed the stoichiometry effect on EAC in PECVD SiN_x barrier films, which resulted in insignificant differences in the subcritical crack growth rates of v. This experiment was performed on Si:N ratios that ranged from 1:1.098 to 1:1.495 in PECVD SiN_x films that were characterized by XPS. Density changes of less than 10% and variations of Si bonded to hydrogen from 4.4 to 27.8% were calculated accordingly. In this range of PECVD SiN_x samples, the EAC by continuous reactions at the same level of

energy favored spots for bond breaking (section 2.3) is predicted, leading to similar crack growth rates.

CHAPTER 5. OPTIMIZING CRACK ONSET STRAIN FOR SiN_x / CYTOP NANOLAMINATE FILMS

5.1 Nanolaminates using alternative SiN_x inorganic layer and CYTOP organic layer

The packaging of flexible electronics provides unique challenges that are not typically seen in the development of conventional electronic devices. These devices must maintain device functionality which may be electronic or optoelectronic, while also limiting degradation under mechanical deformation and exposure to various environments. For devices such as flexible or foldable organic light-emitting diodes,[124] thin film solar cells,[125-126] thin-film transistors,[127] organic memories[128] and sensors,[129] barrier films are utilized in order to limit the exposure to environmental water vapor and oxygen which are known to reduce lifetime and reliability.[130-132] Barrier coatings, which often contain inorganic films, must withstand applied strains without forming cracks. Substrates for flexible electronics devices are often polymers which leads to an increase in the driving force for crack propagation.[61, 63] This is a result of the fact that the mechanical constraint to crack opening displacement is substantially reduced when the substrate changes from stiff to compliant materials, with everything else being equal.

As mentioned in the beginning of chapter 1, the maximum possible applied strains in the brittle thin barriers are restricted to be a few percent (1~3%)[2, 38]. Although these brittle barriers cannot be applied to highly stretchable devices requiring tens of percent strain, a few percent can be sufficient for bendable / foldable devices. However, reducing

the radius of curvature in such applications quickly runs into the strain to failure limits of the brittle layers in these barriers. Thus, even a 1 % change of the maximum possible applied strains can make a significant difference in increasing the mechanical stability of barrier coatings used in flexible and foldable electronics.

Therefore, the aim of this study is to utilize a high fracture toughness organic layer in a multilayer architecture to maximize the COS, guided by numerical analyses. To realize this, PECVD SiN_x was used as an inorganic layer and spin-coated CYTOP as an organic layer. PECVD SiN_x has been used as nanolaminates with other ALD metal oxides or organic layers to reduce WVTR[29, 133]. CYTOP is an amorphous fluoro-polymer used as dielectric layer in state-of-the-art organic thin-film transistors with high reliability,[134] and has been also used in barrier coatings with inorganic layers that display long-term environmental stability.[29] The thickness can be easily controlled and its high transmittance across the ultraviolet and visible spectral ranges is well documented.

5.1.1 Nanolaminates Fabrication

To form the barrier samples, heat-stabilized 125 μm thick PET (Dupont Teijin Films Melinex ST505) substrates were laser-cut prior to deposition to a size of 5 mm by 50 mm. Then, 250 nm PECVD SiN_x (Unaxis PECVD system with radio frequency (rf) parallel plate configuration) films were deposited on the PET at a temperature of 110 °C, pressure of 1 Torr, 20 W rf plasma and a rate of 10 nm/min. The amorphous fluoropolymer CYTOP (CTL-809M, Asahi Glass Company) was mixed with the solvent CT-SOLV180 and stirred for one hour at room temperature. The spin-coated polymer films were cured at 100 °C for 15 minutes. CYTOP films with six different thicknesses ranging from 33 to 880

nm were produced by varying the mixing ratio of the CYTOP and the solvent, and spinning rate. The thickness of the CYTOP films was determined by spin-coating the films on silicon wafer and measured using spectroscopic ellipsometry (Woollam M2000 Ellipsometer). Following the spin-coating of CYTOP, the substrates were transported to the PECVD chamber for SiN_x film deposition.

5.1.2 Modeling Setup for Multilayer Thin Film

To calculate the driving force *G* in nanolaminates, the modeling method created by Long *et al*. was used,[56] described in section 1.2.1. The COS, ε_c, can be determined after obtaining the dimensionless energy release rate, Z, from finite element results:

$$\varepsilon_c = \sqrt{\frac{\Gamma}{E_i^* h_i Z}} \tag{14}$$

where E_i^* and h_i are the plane strain elastic modulus and thickness of the inorganic film, respectively. Here, for composite films, Γ is the average fracture energy, which can be defined depending on which layers are subjected to crack propagation as:

$$\Gamma = (\Gamma_o h_{oc} + \Gamma_i h_{ic})/(h_{oc} + h_{ic}) \tag{15}$$

where Γ_i and Γ_o are fracture energy of the inorganic SiN_x layers and the organic CYTOP layers, respectively; h_{ic} and h_{oc} are the total thickness of cracked inorganic layers and cracked organic layers, respectively. Identical dimensions with tested specimens for experimentation were applied in the model geometry (see Figure 5.1).

The experimental mechanical parameters outlined by the previous work[2, 135] were used. Young's modulus and Poisson's ratio were taken to be E_o = 1.5 GPa, ν = 0.42 for the

CYTOP layer, as provided by the manufacturer, E_i = 123 GPa, ν = 0.253 for the SiN_x layer, and E_s = 4.07 GPa, ν = 0.3 for the PET substrate. The modulus of the SiN_x film E_i was measured by indenting a depth of 200 - 300 nm of a 1 μm thick PECVD SiN_x on a Si-wafer using nanoindentation (Hysitron triboindenter). The properties of the PET substrate was measured using uniaxial tensile testing. The residual stress of the SiN_x film was measured to be σ_f = -185 MPa[2]. The residual stress of the CYTOP films was assumed to be zero.[29, 136] The impact on Z (and therefore G), coming from a result of the residual stress of the films and their thicknesses, was implemented to calculate COS for each case.

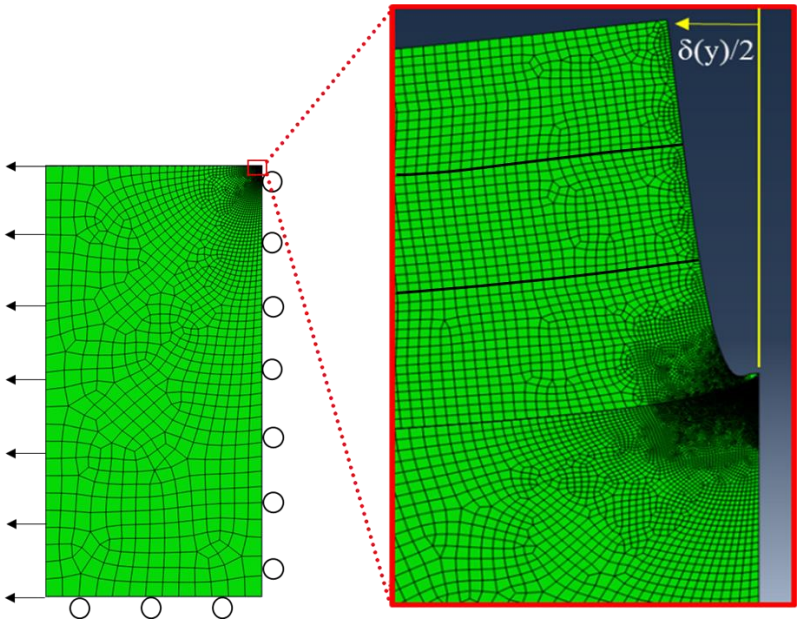

Figure 5.1: (a) Example of finite element model consisting of a 3-layer structure with an all-through crack.

5.1.3 Crack Onset Strain Measurement

In-situ laser confocal microscopy (Olympus LEXT, OLS4100) was used to observe the channel cracks on the surface of nanolaminate films using a microtensile testing stage (Linkam Scientific Instruments, TST350). The detailed experimental procedure is

described in the previous work[1-2, 135]. Tests were performed in laboratory air at room temperature. The cracks were captured in the magnified area of 125 × 125 μm as shown in Figure 5.2. Depth profiling was further performed for a specific specimen to clarify the failure mode of channel cracking. A magnified area of 32 × 32 μm was used to focus on one channel crack at specific value of applied strain. The parameters of micro-topographies were registered using a 3D laser measuring microscope with scanning mode "XYZ fine scan + Color", an image size of 1024 × 1024 pixels with an 8× zoom. The measuring time was variable and lasted for a few minutes.

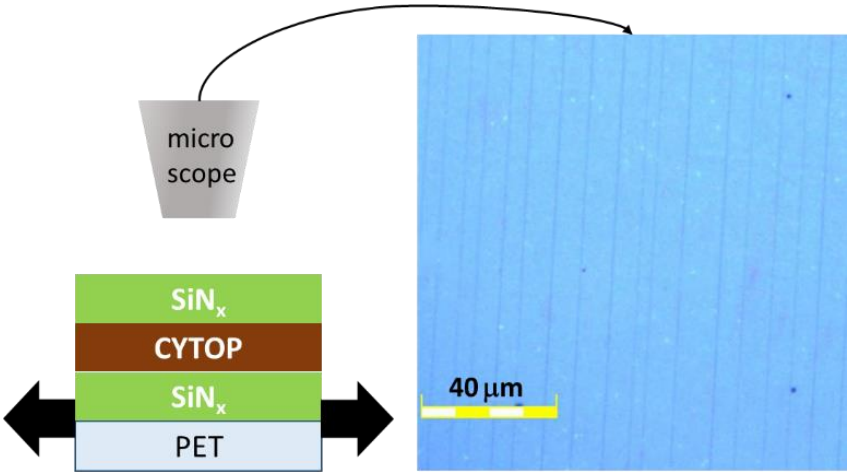

Figure 5.2: Schematic (not drawn to scale) of the experimental set up with a representative optical image of channel cracks in a nanolaminate on PET.

5.2 Quantification of Mechanical Properties and Failures

5.2.1 Fracture Energy Calculation for Organic Layer

One of the key material properties to increase the nanolaminate's COS is Γ_o that needs to be much larger than Γ_i = 25.2 ± 1.26 J·m^{-2} [2] (otherwise, the nanolaminates have lower COS values). However, accurate measurement of large Γ_o values for thin layers may

be challenging using the above numerical modeling scheme that relies on linear elasticity. For thin layers and large Γ_o values, the COS of that inorganic layer on PET would exceed 10 %, which would prevent the calculation of G using Eq. 8. To circumvent this issue, a simple 2-layer nanolaminate structure was used on PET consisting of a 250-nm-thick SiN_x layer and CYTOP on top with varying thicknesses to decrease the combined fracture energy (see Eq. 15). If the CYTOP layer is thin enough compared to SiN_x, the COS of that bilayer is still small enough, (such that G can be calculated using Eq. 8 assuming linear elasticity), and a function of the CYTOP thickness. Therefore, using this technique, even large Γ_o values can be obtained by fitting the numerical results to the experimental data. To do so, the COS for a single dyad of SiN_x/CYTOP on PET was modeled as a function of CYTOP layer thickness (for h_i = 250 nm) and Γ_o. The three possible failure modes (cracking of CYTOP only, SiN_x only, and of both layers together (all-through crack)) were evaluated. In the case of cracking only in the CYTOP layer, the COS was calculated to be over 60%, and therefore excluded in Figure 5.3 (the COS is the lowest values among the three failure modes). Figure 5.3 shows the predicted COS values as a function of h_o/h_i, over the range of 0-0.4, for two different Γ_o values (80 and 100 $J \cdot m^{-2}$). The modeling results indicate that the dominant failure mode starts with an all-through crack for h_o/h_i between 0 and 0.25-0.3 (depending of Γ_o), and switches into a cracking only in the SiN_x layer for larger h_o/h_i values. Figure 5.3 also shows the experimental COS values of the bilayers for h_i = 250 nm and h_o = 0, 25 and 50 nm. The COS values increase from 0.95 ± 0.02 to 1.2 ± 0.03 % with increasing h_o which is consistent with the predicted all-through cracking failure mode for low h_o / h_i ratios. The fit of the numerical results to the experiments yields $\Gamma_o = 90 \pm 10\ J \cdot m^{-2}$

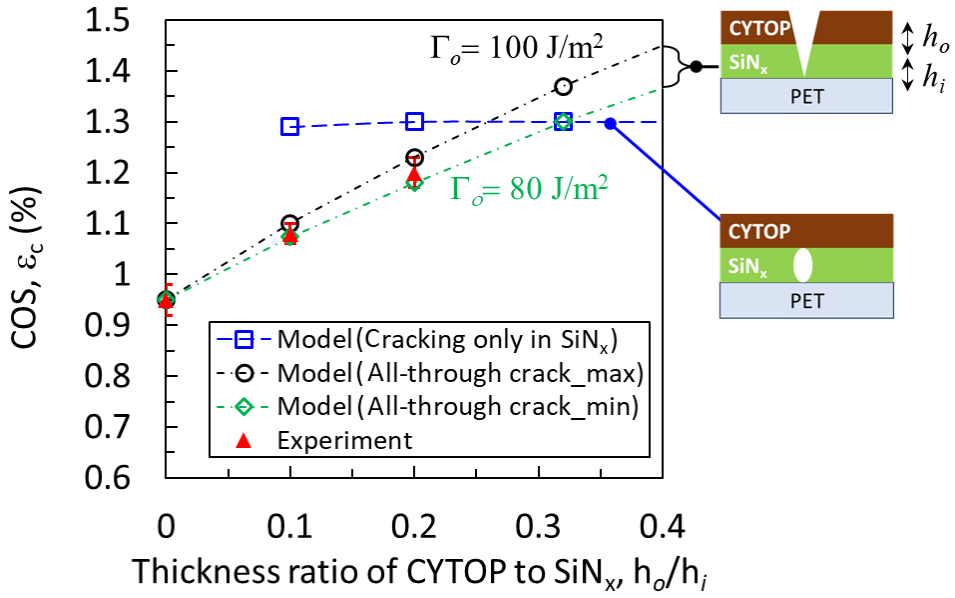

Figure 5.3: Experimental and numerically calculated crack onset strain (COS) as a function of thickness ratio of CYTOP, h_o, to SiN_x, h_i = 250 nm. Models show COS for two different cracking modes: all-through crack (schematic on the upper right side, not drawn to scale) and crack only in SiN_x layer (figure on the lower right side, not drawn to scale). Lower (80 J·m^{-2}) and upper (100 J·m^{-2}) bounds of the fracture energy of CYTOP organic layer, Γ_o, were obtained by fitting the modeling curves to the experimental results

5.2.2 Optimized Crack Onset Strain

Knowing Γ_o and Γ_i, the COS was numerically predicted (based only on the two failure modes that had the lowest COS values, as shown in Figure 5.4) for a tri-layer structure (CYTOP in between two SiN_x layers; see schematic in Figure 5.4) on PET, with h_i = 30 nm (*i.e.*, total SiN_x thickness is 60 nm) and h_o ranging from 33 to 450 nm, and compared to the experimental results. The experimental results are in very good agreement with the numerical predictions, following the predicted trend in COS values that initially increase with increasing h_o (dominant failure mode is all-through crack) then decrease for larger h_o values ($h_o/h_i > 1.15$; dominant failure mode is cracking of the top SiN_x layer only). Importantly enough, these results are the first experimental confirmation of a 50 % increase

in COS value by careful optimization, from 1.7 ± 0.08 % (for a 60 nm SiN_x film with no CYTOP) to 2.5 ± 0.08 % for two 30 nm SiN_x layers separated by 33 nm of CYTOP. The maximal increase in COS occurs for $h_o/h_i = 1.15$.

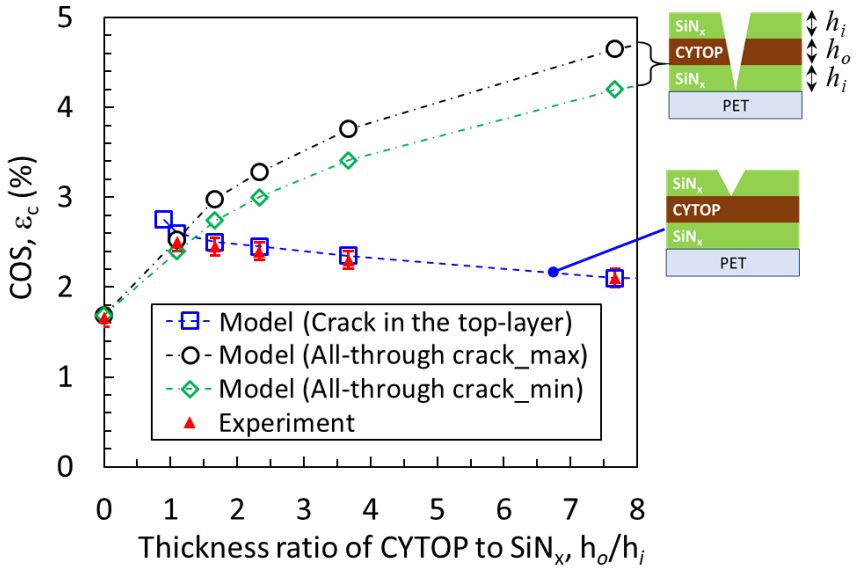

Figure 5.4: Experimental and numerically calculated COS as a function of thickness ratio of CYTOP, h_o, to SiN_x, h_i = 30 nm. Models show COS for two different cracking modes: all-through crack (schematic on the upper right side, not drawn to scale), using both lower and upper bounds for Γ_0 (80 and 100 J·m^{-2}, respectively) and crack only in the top SiN_x layer (schematic on the lower right side, not drawn to scale).

5.2.3 Depth Profiling of Failure Mode of Channel Cracking

To confirm that the failure mode of the experiments matched the predictions, depth profiling using laser scanning confocal microscopy was applied. Figure 5.5 shows the depth profiling results of the specimen structures of 50 nm CYTOP / 250 nm SiN_x on PET substrate. As shown in Figure 5.3, numerical modeling predicts a COS of 1.2 % corresponding to the all-through crack failure mode. In-situ depth profiling tensile tests showed channel crack depths of 275 ± 23 nm with a 1.2 % increase in applied strain. Also, Figure 5.6 shows the depth profiling results on the specimen structure of 60 nm SiN_x on

PET substrate, 30 nm SiN_x / 50 nm CYTOP / 30 nm SiN_x on PET substrate, and 30 nm SiN_x / 110 nm CYTOP / 30 nm SiN_x on PET substrate. Numerical modeling predicts a COS corresponding to the SiN_x top-layer crack failure mode for both 3-layer nanolaminates. In-situ depth profiling tensile tests showed channel crack depths of 59 ± 5 nm, 26 ± 3 nm, and 28 ± 4 nm for 60 nm SiN_x on PET substrate; 30 nm SiN_x / 50 nm CYTOP / 30 nm SiN_x on PET substrate; and 30 nm SiN_x / 110 nm CYTOP / 30 nm SiN_x on PET substrate, respectively; each depth is an average of 20-25 measurements. These results confirm the accuracy of the theoretical predictions. When the top-layers of 3-layer structures crack, reduced crack spacings (and thus increased interactions with other cracks) do not create all-through cracks but rather make already present cracks grow (see Figure 5.6 (b), (c)). Note that COS of all-through crack in Figure 5.4 comes from a pristine surface; if there are already cracked layers, greater applied strain is required to create all-through cracks.

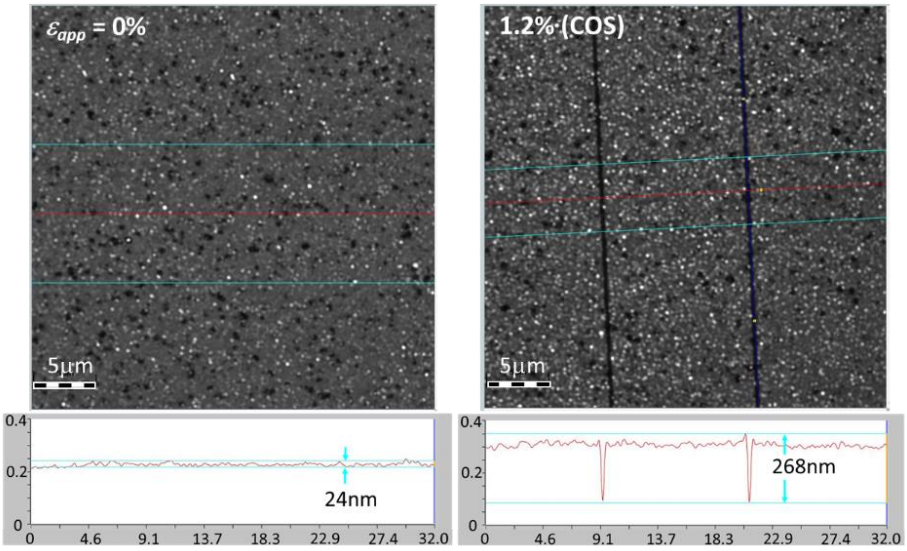

Figure 5.5: Depth profiling images revealing surface roughness and depth of the channel crack in 50 nm CYTOP / 250 nm SiN_x on 125 μm thick PET at the applied strains of 0 % and 1.2 %, respectively.

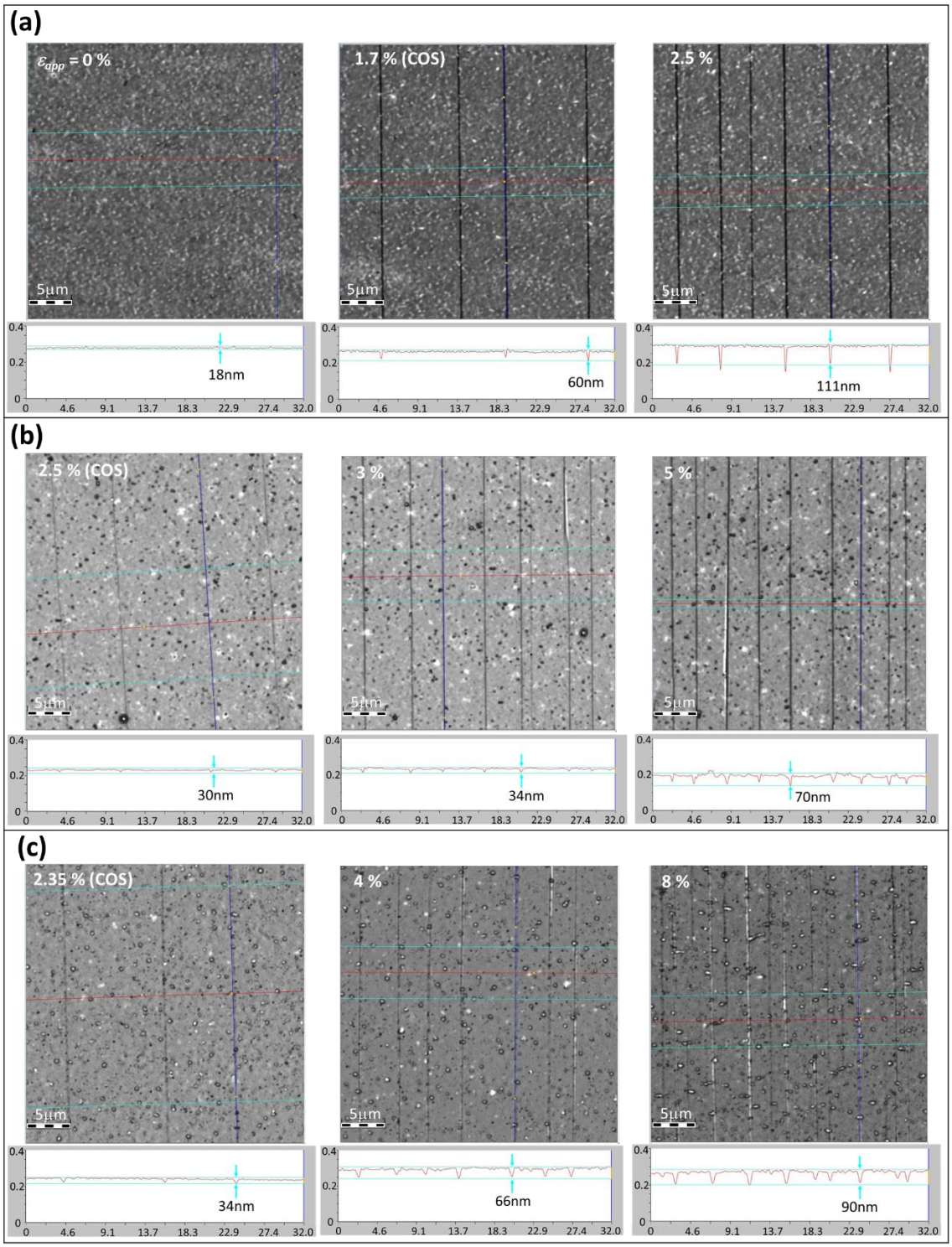

Figure 5.6: Depth profiling images revealing depth of the channel crack (and therefore cracking mode) in (a) 60 nm SiN_x on PET substrate, (b) 30 nm SiN_x / 50 nm CYTOP / 30 nm SiN_x on PET substrate, and (c) 30 nm SiN_x / 110 nm CYTOP / 30 nm SiN_x on PET substrate. Applied strains are indicated on the images.

5.2.4 *Optimized COS for Both Chemical and Mechanical Stability*

Using this theoretical model, the maximum COS values for 3-layer and 5-layer structures were computed and compared to a single layer of SiN_x, as a function of total SiN_x thickness ranging from 50 to 500 nm. Figure 5.7 shows that the optimized COS values for the 3-layer and 5-layer structures also follow the $h^{-0.5}$ trend (with h the total SiN_x thickness) that is known to dictate COS for single layers (see Eq. 1 and 7), albeit at larger values. The maximum increase in COS is 45 - 47 % for the 3-layer structure and 71 - 73 % for the 5-layer structure, which occurs for an optimized CYTOP-to-SiN_x thickness of 1.15, regardless of the thickness. The small drop in COS improvement with increasing thickness (see Figure 5.7), from 47 to 45 % for 3 layers, and from 73 to 71 % for 5 layers, is likely related to the finite thickness effect of the substrate, providing slightly lower amount of constraint.[55-56, 62]

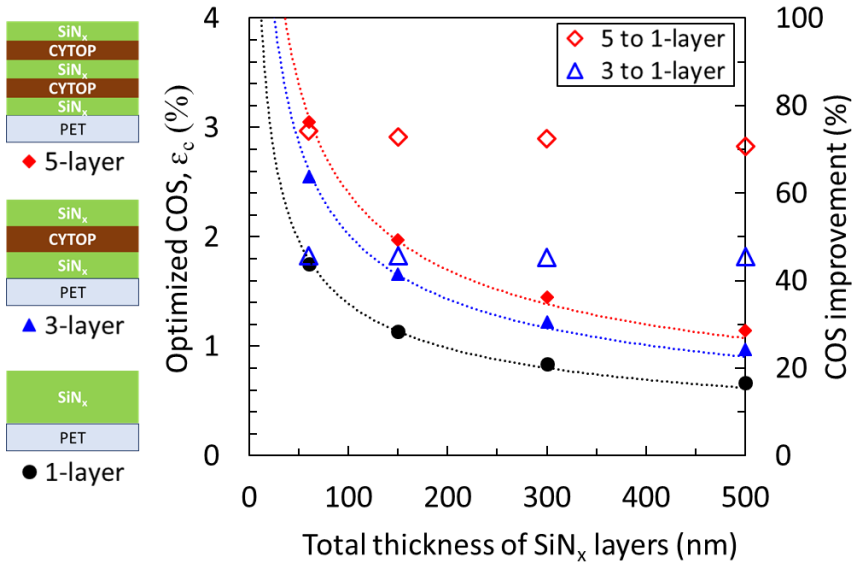

Figure 5.7: Largest predicted COS values for 3-layer and 5-layer nanolaminates (see schematics) versus single layer of SiN_x, as a function of total SiN_x thickness. Lines are fits to $h^{-1/2}$ power equation. Right axis provides relative improvement in COS with respect to single SiN_x layer.

The information shown in Figure 5.7 is crucial for the design of nanolaminate barriers that satisfy both mechanical and chemical requirements for proper functioning of the devices. From a mechanical perspective, thinner total stacks of the inorganic layer and larger number of layers provide larger COS values. However, the total thickness of the inorganic layer must be large enough to keep the minimum required WVTR in case of degradation due to humidity. In addition, the thickness of each individual inorganic layer must also be larger than the critical thickness below which the WVTR degrades abruptly, providing upper limits to the number of possible layers for a given total thickness. The existence of critical thickness has been explained by defect dominated gas diffusion via pin holes below the critical thickness.[24, 35-36] For example, in the case of ALD alumina inorganic films, the critical thickness was found to be 15 nm at 38°C in Ca test measurement to maintain WVTR below 10^{-4} $g \cdot m^{-2} \cdot day^{-1}$,[34] and is expected to be less than 100 nm for PECVD grown SiN_x [29]. Furthermore, substrate plasticity should also be considered at applied strains exceeding the substrate yield strain (~2.5 % for PET).[2] Other possibilities of failure modes, including delamination, can also occur at high applied strain, which has not been considered in this work.

5.3 Summary and Conclusions

Nanolaminates using alternating inorganic and organic layers have the potential to provide ultrabarrier films possessing both high COS and high resistance to gas permeation. Previous modeling highlighted the possibility to achieve an optimized design (depending on thickness and material properties (elastic modulus, fracture energy), producing the

highest possible value of COS. In this study, it is experimentally shown that the optimization can be achieved using SiN_x/CYTOP laminates when guided by theoretical predictions. Nanolaminates using SiN_x inorganic films and CYTOP organic films were fabricated. The fracture energy of the CYTOP layer was found to be 90 ± 10 $J \cdot m^{-2}$, thanks to a combination of modeling and COS measurements of bilayers made of SiN_x and CYTOP. A 47 % increase in COS (from 1.6 to 2.5 %) was experimentally measured and is consistent with the numerical predictions, as a result of the thickness ratio optimization for a 3-layer structure consisting of two 30-nm-thick SiN_x layers and one 33-nm-thick CYTOP layer. The numerical results also showed that a 47 % and 73 % increase of COS can be obtained in 3-layer and 5-layer structure (three inorganic and two organic layers) from a single layer, respectively, as the thickness ratio of CYTOP to SiN_x layer is at the optimized value, *i.e.* 1.15. The same procedure can be applied to all inorganic / organic multilayered films to find the optimized COS, including the measurement of high fracture energy of organic layers, enabling the design of mechanically robust permeation barriers for flexible electronics.

CHAPTER 6. CONCLUSIONS

6.1 Summary of Contributions

Thin inorganic barrier films are used in flexible electronics to ensure chemical reliability by protecting the functional layer of the device from oxygen and moisture permeation. Due to inorganic materials' brittle nature, the mechanical failures of the barrier films under mechanical loading, such as stretching, bending, and folding, has proven to be of crucial importance for the reliable functioning of flexible devices. In this research, the primary mechanical failure, channel cracking, under applied strain was the main focus.

The body of this work can be divided into two parts: subcritical crack growth behavior and optimization of COS. Both parts used PECVD SiN_x as exemplary thin film materials. One reason is due to its EAC behavior, which has not been quantified prior to this work, along with its fast and easy fabrication procedures and the many other advantages that were mentioned in the beginning of Chapter 2. More importantly, PECVD SiN_x has been extensively used in flexible electronics.

To quantify the reliability of thin film materials, an *in-situ* microscopy tensile test was applied with various loading and environmental conditions. COS, density of cracks, stress relaxation, residual strain, and stress-strain curves were obtained. More importantly, images of crack-tip were captured over time to measure the crack growth rate and thus *v*-*G* curves and long-term crack growth rate behaviors were achievable. Different *v*-*G* curve properties (*i.e.*, the exponent, *n*, of the power equation and the driving force range of subcritical crack growth region) and density of cracks in humid air and in dry nitrogen were

highlighted in the EAC in SiN_x. The testing process was further developed to quickly obtain the subcritical crack growth properties simply by using a single specimen. This testing technique is applicable to any thin film materials that are undergoing EAC under the assumption of the minimal stress relaxation effect of polymer substrates on driving force change. Both activation energy and activation volume were also calculated by measuring crack growth properties at different temperatures in air. The values were in the comparable range with the simulation results; thus, a thermodynamic favorable reaction mechanism of water molecules with hydrogen-passivated SiN_x barrier films is likely to be responsible for the observed EAC.

Long-term crack growth rate behaviors of PECVD SiN_x barrier films were quantified, which are involved with substrate cracking and adjacent crack spacing, effecting on driving force of propagating channel crack. While EAC in SiN_x has been previously demonstrated, with constant crack growth rates over short periods of time (<1 hour) during which no substrate damage was observed, long-term experiments reveal a regime where cracking also develops in the polymer substrate. This time-dependent local cracking of the polymer underneath the channel crack is expected based on creep rupture or static fatigue. The combined *in-situ* microscopy and finite element modeling results highlight the combined effects of neighboring cracks and substrate cracking on the crack growth rate evolution in the film. In most cases, the subcritical crack growth rates decrease over time by up to two orders of magnitude until steady-state rates are reached. For SiN_x on PI, crack growth rates were found to be more stable over time due to the lack of crack growth in the substrate as compared to SiN_x on PET. These results provide a guideline to

effectively improving the long-term reliability of flexible barriers by a substrate possessing high strength which limits substrate damage.

In an attempt to minimize the EAC in SiN_x, two additional studies were conducted: ALD capping layer and stoichiometry change. Neither showed visible differences in the results. However, the ALD capping layer showed a 30-50% increase in the driving force threshold, G_{th}. The higher threshold values to observe EAC is possibly the result of the capping layer effect on steric hindrance of the environmental species. An effective capping layer should remain uncracked during the cracking of the underlying SiN_x. A parametric study showed that it was not possible with alumina; instead a high fracture energy, low elastic modulus (*e.g.*, organic material) capping layer can cause a failure mode transition to cracking only in SiN_x layer, presumably expected to protect SiN_x from EAC degradation.

Lastly, COS optimization was experimentally achieved using SiN_x/CYTOP nanolaminates. The fracture energy of the CYTOP layer was able to be found, thanks to the combination of modeling and COS measurements of bilayers made of SiN_x and CYTOP. This fracture energy calculation method can be used to easily obtain high fracture energy contained films. A 47 % increase in COS (from 1.6 to 2.5 %) was experimentally measured and is consistent with the numerical predictions, as a result of the thickness ratio optimization for a 3-layer structure consisting of two 30-nm-thick SiN_x layers and one 33-nm-thick CYTOP layer. The numerical results also showed that a 47% and 73% increase of COS can be obtained in 3-layer and 5-layer structure (three inorganic and two organic layers) from a single layer, respectively, as the thickness ratio of CYTOP to SiN_x layer is at the optimized value, *i.e.* 1.15. The same procedure can be applied to all inorganic / organic multilayered films to find the optimized COS, including the measurement of high

fracture energy of organic layers, enabling the design of mechanically robust permeation barriers for flexible electronics.

6.2 Recommendations for Future Work

The present study provided several insights into the characterization of the mechanical reliability of thin films. However, during the course of this study, several avenues for further research were revealed. The following are some recommendations to create advanced thin barrier films:

- Reducing the elastic mismatch with the thin film that is deposited on top of the substrate is the key to increasing the COS. This can be done by the wise selection of materials, such as a high modulus substrate or a substrate that contains an interlayer with a modulus gradient. This will provide limited substrate cracking and thus improve the mechanical reliability. It will be interesting to observe the difference (the level and quickness of the drop in the crack growth rate) in long-term crack growth rate behavior when environmental conditions change for substrate-cracking-free specimens.

- High-fracture energy that is contained in the CYTOP organic thin films helps create high-COS nanolaminates, as shown in Chapter 5. This can also be used as a capping layer of thin film materials that are undergoing EAC, presumably expected to protect from EAC degradation during mechanical loading. As shown in section 4.1, high-fracture energy that is contained in an organic capping layer instead of an ALD

inorganic capping layer can give a window of a dominant failure mode as cracking only in the SiN_x layer.

- With the help of developed testing methods (*i.e.*, the external-load assisted channel crack growth technique and the high fracture energy calculation method, which is accomplished by lowering the average fracture energy using low-fracture energy materials), it would be helpful to characterize all currently existing thin film materials and to have a map that presents its properties, including COS, EAC (*v*-*G* curve), and fracture energy Γ, arranged in the proper order for guiding future selection.

These recommendations comprise further study options for characterizing the mechanical reliability of thin barrier film materials. Future studies should aim to create the strongest (mechanically) thin barrier films for flexible electronics applications.

REFERENCES

1. Kim, K.; Graham, S.; Pierron, O., Note: A single specimen channel crack growth technique applied to brittle thin films on polymer substrates. *Review of Scientific Instruments* **2017,** *88* (3), 036102.

2. Kim, K.; Luo, H.; Singh, A. K.; Zhu, T.; Graham, S.; Pierron, O. N., Environmentally Assisted Cracking in Silicon Nitride Barrier Films on Poly (ethylene terephthalate) Substrates. *ACS applied materials & interfaces* **2016,** *8* (40), 27169-27178.

3. Ok, K.-H.; Kim, J.; Park, S.-R.; Kim, Y.; Lee, C.-J.; Hong, S.-J.; Kwak, M.-G.; Kim, N.; Han, C. J.; Kim, J.-W., Ultra-thin and smooth transparent electrode for flexible and leakage-free organic light-emitting diodes. *Scientific reports* **2015,** *5*.

4. Bae, M. S.; Park, C.; Shin, D.; Lee, S. M.; Yun, I., Effects of mechanical stresses on the reliability of low-temperature polycrystalline silicon thin film transistors for foldable displays. *Solid-State Electronics* **2017,** *133*, 1-5.

5. Choi, G. M.; Jin, J.; Shin, D.; Kim, Y. H.; Ko, J. H.; Im, H. G.; Jang, J.; Jang, D.; Bae, B. S., Flexible Hard Coating: Glass-Like Wear Resistant, Yet Plastic-Like Compliant, Transparent Protective Coating for Foldable Displays. *Advanced Materials* **2017,** *29* (19).

6. Yoon, J.; Sung, H.; Lee, G.; Cho, W.; Ahn, N.; Jung, H. S.; Choi, M., Superflexible, high-efficiency perovskite solar cells utilizing graphene electrodes: towards future foldable power sources. *Energy & Environmental Science* **2017,** *10* (1), 337-345.

7. Kim, I.; Woo, K.; Zhong, Z.; Lee, E.; Kang, D.; Jeong, S.; Choi, Y.-M.; Jang, Y.; Kwon, S.; Moon, J., Selective Light-Induced Patterning of Carbon Nanotube/Silver

Nanoparticle Composite To Produce Extremely Flexible Conductive Electrodes. *ACS applied materials & interfaces* **2017,** *9* (7), 6163-6170.

8. Yu, G.; Gao, J.; Hummelen, J. C.; Wudl, F.; Heeger, A. J., Polymer photovoltaic cells: enhanced efficiencies via a network of internal donor-acceptor heterojunctions. *Science* **1995,** *270* (5243), 1789-1791.

9. Brabec, C. J.; Sariciftci, N. S.; Hummelen, J. C., Plastic solar cells. *Advanced functional materials* **2001,** *11* (1), 15-26.

10. Forrest, S. R., The path to ubiquitous and low-cost organic electronic appliances on plastic. *Nature* **2004,** *428* (6986), 911.

11. Burroughes, J.; Jones, C.; Friend, R., New semiconductor device physics in polymer diodes and transistors. *Nature* **1988,** *335* (6186), 137.

12. Brabec, C. J., Organic photovoltaics: technology and market. *Solar energy materials and solar cells* **2004,** *83* (2-3), 273-292.

13. Brabec, C.; Scherf, U.; Dyakonov, V., *Organic photovoltaics: materials, device physics, and manufacturing technologies*. John Wiley & Sons: 2011.

14. Lewis, J., Material challenge for flexible organic devices. *Materials Today* **2006,** *9* (4), 38-45.

15. Leterrier, Y., Durability of nanosized oxygen-barrier coatings on polymers. *Progress in Materials Science* **2003,** *48* (1), 1-55.

16. McKeen, L. W., *Permeability properties of plastics and elastomers*. William Andrew: 2016.

17. Lueder, E., Passive and active matrix liquid crystal displays with plastic substrates. *Proc. Electrochem. Soc* **1999,** *98*, 336-354.

18. Jamieson, E.; Windle, A., Structure and oxygen-barrier properties of metallized polymer film. *Journal of Materials Science* **1983,** *18* (1), 64-80.

19. Henry, B.; Dinelli, F.; Zhao, K.-Y.; Grovenor, C.; Kolosov, O.; Briggs, G. A. D.; Roberts, A.; Kumar, R.; Howson, R., A microstructural study of transparent metal oxide gas barrier films. *Thin Solid Films* **1999,** *355*, 500-505.

20. Park, S.-H. K.; Oh, J.; Hwang, C.-S.; Lee, J.-I.; Yang, Y. S.; Chu, H. Y., Ultrathin film encapsulation of an OLED by ALD. *Electrochemical and solid-state letters* **2005,** *8* (2), H21-H23.

21. Kim, N.; Yoo, S.; Potscavage, W.; Domercq, B.; Kippelen, B.; Graham, S. In *Fabrication and Characterization of SiOx/Parylene and SiNx/Parylene Thin Film Encapsulation Layers*, ASME 2007 InterPACK Conference collocated with the ASME/JSME 2007 Thermal Engineering Heat Transfer Summer Conference, American Society of Mechanical Engineers: 2007; pp 933-938.

22. Lewis, J. S.; Weaver, M. S., Thin-film permeation-barrier technology for flexible organic light-emitting devices. *IEEE Journal of selected topics in quantum electronics* **2004,** *10* (1), 45-57.

23. Dennler, G.; Lungenschmied, C.; Neugebauer, H.; Sariciftci, N. S.; Latreche, M.; Czeremuszkin, G.; Wertheimer, M. R., A new encapsulation solution for flexible organic solar cells. *Thin Solid Films* **2006,** *511*, 349-353.

24. da Silva Sobrinho, A.; Czeremuszkin, G.; Latreche, M.; Wertheimer, M., Defect-permeation correlation for ultrathin transparent barrier coatings on polymers. *Journal of Vacuum Science & Technology A: Vacuum, Surfaces, and Films* **2000,** *18* (1), 149-157.

25. da Silva Sobrinho, A.; Latreche, M.; Czeremuszkin, G.; Klemberg-Sapieha, J.; Wertheimer, M., Transparent barrier coatings on polyethylene terephthalate by single-and dual-frequency plasma-enhanced chemical vapor deposition. *Journal of Vacuum Science & Technology A: Vacuum, Surfaces, and Films* **1998,** *16* (6), 3190-3198.

26. George, S. M., Atomic layer deposition: an overview. *Chemical reviews* **2009,** *110* (1), 111-131.

27. Parsons, G. N.; George, S. M.; Knez, M., Progress and future directions for atomic layer deposition and ALD-based chemistry. *Mrs Bulletin* **2011,** *36* (11), 865-871.

28. Hoivik, N. D.; Elam, J. W.; Linderman, R. J.; Bright, V. M.; George, S. M.; Lee, Y., Atomic layer deposited protective coatings for micro-electromechanical systems. *Sensors and Actuators A: Physical* **2003,** *103* (1-2), 100-108.

29. Bulusu, A.; Singh, A.; Wang, C. Y.; Dindar, A.; Fuentes-Hernandez, C.; Kim, H.; Cullen, D.; Kippelen, B.; Graham, S., Engineering the mechanical properties of ultrabarrier films grown by atomic layer deposition for the encapsulation of printed electronics. *Journal of Applied Physics* **2015,** *118* (8), 085501.

30. Andringa, A. M.; Perrotta, A.; de Peuter, K.; Knoops, H. C.; Kessels, W. M.; Creatore, M., Low-Temperature Plasma-Assisted Atomic Layer Deposition of Silicon Nitride Moisture Permeation Barrier Layers. *ACS applied materials & interfaces* **2015,** *7* (40), 22525-32.

31. van Assche, F. J.; Unnikrishnan, S.; Michels, J. J.; van Mol, A. M.; van de Weijer, P.; van de Sanden, M. C.; Creatore, M., On the intrinsic moisture permeation rate of remote microwave plasma-deposited silicon nitride layers. *Thin Solid Films* **2014,** *558*, 54-61.

32. Zhang, S.; Xue, W.; Yu, Z., Moisture barrier evaluation of SiOx/SiNx stacks on polyimide substrates using electrical calcium test. *Thin Solid Films* **2015,** *580*, 101-105.

33. Seo, S.-W.; Jung, E.; Lim, C.; Chae, H.; Cho, S. M., Moisture permeation through ultrathin TiO2 films grown by atomic layer deposition. *Applied Physics Express* **2012,** *5* (3), 035701.

34. Carcia, P.; McLean, R.; Reilly, M., Permeation measurements and modeling of highly defective Al 2 O 3 thin films grown by atomic layer deposition on polymers. *Applied physics letters* **2010,** *97* (22), 221901.

35. Meyer, J.; Schmidt, H.; Kowalsky, W.; Riedl, T.; Kahn, A., The origin of low water vapor transmission rates through Al 2 O 3/ZrO 2 nanolaminate gas-diffusion barriers grown by atomic layer deposition. *Applied Physics Letters* **2010,** *96* (24), 117.

36. Dameron, A. A.; Davidson, S. D.; Burton, B. B.; Carcia, P. F.; McLean, R. S.; George, S. M., Gas diffusion barriers on polymers using multilayers fabricated by Al2O3 and rapid SiO2 atomic layer deposition. *The Journal of Physical Chemistry C* **2008,** *112* (12), 4573-4580.

37. Groner, M.; George, S.; McLean, R.; Carcia, P., Gas diffusion barriers on polymers using Al 2 O 3 atomic layer deposition. *Applied Physics Letters* **2006,** *88* (5), 051907.

38. Jen, S.-H.; Bertrand, J. A.; George, S. M., Critical tensile and compressive strains for cracking of Al2O3 films grown by atomic layer deposition. *Journal of Applied Physics* **2011,** *109* (8), 084305.

39. Hutchinson, J. W.; Suo, Z., Mixed mode cracking in layered materials. *Advances in applied mechanics* **1992,** *29* (63), 191.

40. Jen, S.-H.; Lee, B. H.; George, S. M.; McLean, R. S.; Carcia, P. F., Critical tensile strain and water vapor transmission rate for nanolaminate films grown using Al2O3 atomic layer deposition and alucone molecular layer deposition. *Applied Physics Letters* **2012,** *101* (23), 234103.

41. Miller, D. C.; Foster, R. R.; Zhang, Y.; Jen, S.-H.; Bertrand, J. A.; Lu, Z.; Seghete, D.; O'Patchen, J. L.; Yang, R.; Lee, Y.-C.; George, S. M.; Dunn, M. L., The mechanical robustness of atomic-layer- and molecular-layer-deposited coatings on polymer substrates. *Journal of Applied Physics* **2009,** *105* (9), 093527.

42. Andersons, J.; Modniks, J.; Leterrier, Y.; Tornare, G.; Dumont, P.; Månson, J. A. E., Evaluation of toughness by finite fracture mechanics from crack onset strain of brittle coatings on polymers. *Theoretical and Applied Fracture Mechanics* **2008,** *49* (2), 151-157.

43. Leterrier, Y., Durability of Nanosized Oxygen-barrier Coatings on Polymers. *Prog. Mater. Sci.* **2003,** *48* (1), 1-55.

44. Huang, R. P., J. H.; Suo, Z., Loss of Constraint on Fracture in Thin Film Structures due to Creep. *Acta Mater.* **2002,** *50* (16), 4137-4148.

45. Liang, J. H., R.; Prevost, J. H.; Suo, Z., Thin Film Cracking Modulated by Underlayer Creep. *Exp. Mech.* **2003,** *43* (3), 269-279.

46. Lin, Y.; Tsui, T. Y.; Vlassak, J. J., Water diffusion and fracture in organosilicate glass film stacks. *Acta Materialia* **2007,** *55* (7), 2455-2464.

47. Lane, M. W. S., J. M.; Dauskardt, R. H., Envrionmental Effect on Interfacial Adhesion. *Microelectron. Reliab.* **2001,** *41* (9-10), 1615-1624.

48. Lane, M. W.; Liu, X. H.; Shaw, T. M., Environmental Effects on Cracking and Delamination of Dielectric Films. *IEEE Transactions on Device and Materials Reliability* **2004,** *4* (2), 142-147.

49. Vellinga, W. P.; De Hosson, J. T. M.; Bouten, P. C. P., Effect of relative humidity on crack propagation in barrier films for flexible electronics. *Journal of Applied Physics* **2012,** *112* (8), 083520.

50. Guan, Q.; Laven, J.; Bouten, P. C. P.; de With, G., Subcritical crack growth in SiNx thin-film barriers studied by electro-mechanical two-point bending. *Journal of Applied Physics* **2013,** *113* (21), 213512.

51. Birringer, R. P.; Shaviv, R.; Besser, P. R.; Dauskardt, R. H., Environmentally assisted debonding of copper/barrier interfaces. *Acta Materialia* **2012,** *60* (5), 2219-2228.

52. Douville, N. J.; Li, Z.; Takayama, S.; Thouless, M. D., Fracture of metal coated elastomers. *Soft Matter* **2011,** *7* (14), 6493.

53. Thouless, M. D.; Li, Z.; Douville, N. J.; Takayama, S., Periodic cracking of films supported on compliant substrates. *Journal of the mechanics and physics of solids* **2011,** *59* (9), 1927-1937.

54. Tada, H., Paris, P.C., Irwin, G.R., The Stress Analysis of Cracks Handbook, third ed. . *The American Society of Mechanical Engineers* **2000**.

55. Cordero, N.; Yoon, J.; Suo, Z., Channel cracks in a hermetic coating consisting of organic and inorganic layers. *Applied Physics Letters* **2007,** *90* (11), 111910.

56. Long, R.; Dunn, M. L., Channel cracks in atomic-layer and molecular-layer deposited multilayer thin film coatings. *Journal of Applied Physics* **2014,** *115* (23), 233514.

57. Affinito, J.; Gross, M.; Coronado, C.; Graff, G.; Greenwell, I.; Martin, P., A new method for fabricating transparent barrier layers. *Thin Solid Films* **1996,** *290*, 63-67.

58. Weaver, M.; Michalski, L.; Rajan, K.; Rothman, M.; Silvernail, J.; Brown, J. J.; Burrows, P. E.; Graff, G. L.; Gross, M. E.; Martin, P. M., Organic light-emitting devices with extended operating lifetimes on plastic substrates. *Applied Physics Letters* **2002,** *81* (16), 2929-2931.

59. Chwang, A. B.; Rothman, M. A.; Mao, S. Y.; Hewitt, R. H.; Weaver, M. S.; Silvernail, J. A.; Rajan, K.; Hack, M.; Brown, J. J.; Chu, X., Thin film encapsulated flexible organic electroluminescent displays. *Applied Physics Letters* **2003,** *83* (3), 413-415.

60. Beuth, J., Cracking of thin bonded films in residual tension. *International Journal of Solids and Structures* **1992,** *29* (13), 1657-1675.

61. Vlassak, J. J., Channel cracking in thin films on substrates of finite thickness. *International Journal of Fracture* **2003,** *119* (4), 299-323.

62. Huang, R.; Prévost, J. H.; Huang, Z. Y.; Suo, Z., Channel-cracking of thin films with the extended finite element method. *Engineering Fracture Mechanics* **2003,** *70* (18), 2513-2526.

63. Tsui, T. Y.; McKerrow, A. J.; Vlassak, J. J., Constraint Effects on Thin Film Channel Cracking Behavior. *Journal of Materials Research* **2011,** *20* (09), 2266-2273.

64. Anderson, T. L., *Fracture mechanics: fundamentals and applications*. CRC press: 2017.

65. Mei, H.; Pang, Y.; Huang, R., Influence of interfacial delamination on channel cracking of elastic thin films. *International Journal of Fracture* **2008,** *148* (4), 331-342.

66. Bhatnagar, A.; Hoffman, M. J.; Dauskardt, R. H., Fracture and Subcritical Crack-Growth Behavior of Y-Si-Al-O-N Glasses and Si3N4 Ceramics. *Journal of the American Ceramic Society* **2000,** *83* (3), 585-596.

67. Lawn, B., *Fracture of brittle solids*. Cambridge university press: 1993.

68. Freiman, S. W.; Wiederhorn, S. M.; Mecholsky Jr, J. J., Environmentally enhanced fracture of glass: a historical perspective. *Journal of the American Ceramic Society* **2009,** *92* (7), 1371-1382.

69. Wiederhorn, S.; Fuller, E. R.; Thomson, R., Micromechanisms of crack growth in ceramics and glasses in corrosive environments. *Metal science* **1980,** *14* (8-9), 450-458.

70. ABAQUS/Standard 6.13, U. s. M., SIMULIA, Providence, RI. **2010**.

71. Li, F. M.; Unnikrishnan, S.; van de Weijer, P.; van Assche, F.; Shen, J.; Ellis, T.; Manders, W.; Akkerman, H.; Bouten, P.; van Mol, T. In *18.3: Flexible Barrier Technology for Enabling Rollable AMOLED Displays and Upscaling Flexible OLED Lighting*, SID Symposium Digest of Technical Papers, Wiley Online Library: 2013; pp 199-202.

72. Majee, S.; Geffroy, B.; Bonnassieux, Y.; Bourée, J.-E., Interface effects on the moisture barrier properties of SiNx/PMMA/SiNx hybrid structure. *Surface and Coatings Technology* **2014,** *254*, 429-432.

73. Rochat, G.; Fayet, P., Characterization of mechanical properties of ultra-thin oxide coatings on polymers by uniaxial fragmentation tests. *Journal of Adhesion Science and Technology* **2012,** *26* (20-21), 2381-2392.

74. Wuu, D.; Lo, W.; Chiang, C.; Lin, H.; Chang, L.; Horng, R.; Huang, C.; Gao, Y., Water and oxygen permeation of silicon nitride films prepared by plasma-enhanced chemical vapor deposition. *Surface and Coatings Technology* **2005,** *198* (1-3), 114-117.

75. Keuning, W.; Van de Weijer, P.; Lifka, H.; Kessels, W.; Creatore, M., Cathode encapsulation of organic light emitting diodes by atomic layer deposited Al2O3 films and Al2O3/a-SiNx: H stacks. *Journal of Vacuum Science & Technology A: Vacuum, Surfaces, and Films* **2012,** *30* (1), 01A131.

76. Martyniuk, M. P.; Antoszewski, J.; Musca, C. A.; Dell, J. M.; Faraone, L. In *Determination of residual stress in low-temperature PECVD silicon nitride thin films*, Microelectronics, MEMS, and Nanotechnology, International Society for Optics and Photonics: 2004; pp 451-462.

77. Huang, H.; Winchester, K.; Liu, Y.; Hu, X. Z.; Musca, C. A.; Dell, J. M.; Faraone, L., Determination of mechanical properties of PECVD silicon nitride thin films for tunable MEMS Fabry–Pérot optical filters. *Journal of Micromechanics and Microengineering* **2005,** *15* (3), 608-614.

78. Huang, H.; Winchester, K. J.; Suvorova, A.; Lawn, B. R.; Liu, Y.; Hu, X. Z.; Dell, J. M.; Faraone, L., Effect of deposition conditions on mechanical properties of low-temperature PECVD silicon nitride films. *Materials Science and Engineering: A* **2006,** *435-436*, 453-459.

79. Lane, M. W.; Liu, X. H.; Shaw, T. M., Environmental effects on cracking and delamination of dielectric films. *Device and Materials Reliability, IEEE Transactions on* **2004,** *4* (2), 142-147.

80. Lane, M.; Snodgrass, J.; Dauskardt, R., Environmental effects on interfacial adhesion. *Microelectronics Reliability* **2001,** *41* (9), 1615-1624.

81. Li, H.; Tsui, T. Y.; Vlassak, J. J., Water diffusion and fracture behavior in nanoporous low-k dielectric film stacks. *Journal of Applied Physics* **2009,** *106* (3), 033503.

82. Ishihara, S.; McEvily, A. J.; Goshima, T., Effect of atmospheric humidity on the fatigue crack propagation behavior of short cracks in silicon nitride. *Journal of the American Ceramic Society* **2000,** *83* (3), 571-577.

83. Matoy, K.; Schönherr, H.; Detzel, T.; Schöberl, T.; Pippan, R.; Motz, C.; Dehm, G., A comparative micro-cantilever study of the mechanical behavior of silicon based passivation films. *Thin Solid Films* **2009,** *518* (1), 247-256.

84. Freund, L. B.; Suresh, S., *Thin film materials : stress, defect formation, and surface evolution*. Cambridge University Press: Cambridge, [England] ;, 2003.

85. Kim, T.-S., Adhesion Measurement Methods for Thin Films in Microelectronics. *Journal of Welding and Joining* **2012,** *30* (3), 15-20.

86. Cook, R. F.; Liniger, E. G., Stress-corrosion cracking of low-dielectric-constant spin-on-glass thin films. *J. Electrochem. Soc.* **1999,** *146* (12), 4439-4448.

87. Toivola, Y.; Thurn, J.; Cook, R. F., Structural, electrical, and mechanical properties development during curing of low-k hydrogen silsesquioxane films. *J. Electrochem. Soc.* **2002,** *149* (3), F9-F17.

88. Tsui, T. Y.; McKerrow, A. J.; Vlassak, J. J., Constraint effects on thin film channel cracking behavior. *Journal of Materials Research* **2005,** *20* (9), 2266-2273.

89. Rolston, N.; Watson, B. L.; Bailie, C. D.; McGehee, M. D.; Bastos, J. P.; Gehlhaar, R.; Kim, J.-E.; Vak, D.; Mallajosyula, A. T.; Gupta, G.; Mohite, A. D.; Dauskardt, R. H., Mechanical integrity of solution-processed perovskite solar cells. *Extreme Mechanics Letters*.

90. Tsui, T. Y.; Griffin, A. J.; Fields, R.; Jacques, J. M.; McKerrow, A. J.; Vlassak, J. J., The effect of elastic modulus on channel crack propagation in organosilicate glass films. *Thin Solid Films* **2006,** *515* (4), 2257-2261.

91. Liu, X. H.; Shaw, T. M.; Lane, M. W.; Rosenberg, R. R.; Lane, S. L.; Doyle, J. P.; Restaino, D.; Vogt, S. F.; Edelstein, D. C.; Ieee, *Channel cracking in low-k films on patterned multi-layers*. Ieee: New York, 2004; p 93-95.

92. Favache, A.; Libralesso, L.; Jacques, P. J.; Raskin, J. P.; Bailly, C.; Nysten, B.; Pardoen, T., Fracture toughness measurement of ultra-thin hard films deposited on a polymer interlayer. *Thin Solid Films* **2014,** *550*, 464-471.

93. King, S. W.; Gradner, J. A., Intrinsic stress fracture energy measurements for PECVD thin films in the SiO(x)C(y)N(z):H system. *Microelectronics Reliability* **2009,** *49* (7), 721-726.

94. Matoy, K.; Schonherr, H.; Detzel, T.; Schoberl, T.; Pippan, R.; Motz, C.; Dehm, G., A comparative micro-cantilever study of the mechanical behavior of silicon based passivation films. *Thin Solid Films* **2009,** *518* (1), 247-256.

95. Michalske, T. A.; Freiman, S. W., A molecular mechanism for stress corrosion in vitreous silica. *J. Am. Ceram. Soc.* **1983,** *66* (4), 284-288.

96. Wiederhorn, S. M.; Freiman, S. W.; Fuller, E. R.; Simmons, C. J., EFFECTS OF WATER AND OTHER DIELECTRICS ON CRACK-GROWTH. *J. Mater. Sci.* **1982,** *17* (12), 3460-3478.

97. Wiederhorn, S. M.; Fuller, E. R.; Thomson, R., MICROMECHANISMS OF CRACK-GROWTH IN CERAMICS AND GLASSES IN CORROSIVE ENVIRONMENTS. *Metal Science* **1980,** *14* (8-9), 450-458.

98. Dauskardt, R.; Lane, M.; Ma, Q.; Krishna, N., Adhesion and debonding of multi-layer thin film structures. *Engin. Fract. Mech.* **1998,** *61* (1), 141-162.

99. Hu, M. S.; Evans, A. G., THE CRACKING AND DECOHESION OF THIN-FILMS ON DUCTILE SUBSTRATES. *Acta Metal.* **1989,** *37* (3), 917-925.

100. Huang, R.; Prevost, J. H.; Suo, Z., Loss of constraint on fracture in thin film structures due to creep. *Acta Materialia* **2002,** *50* (16), 4137-4148.

101. Liang, J.; Huang, R.; Prevost, J. H.; Suo, Z., Thin film cracking modulated by underlayer creep. *Exper. Mech.* **2003,** *43* (3), 269-279.

102. Liang, J.; Zhang, Z.; Prevost, J. H.; Suo, Z., Time-dependent crack behavior in an integrated structure. *Int. J. Fract.* **2004,** *125* (3-4), 335-348.

103. Hutchinson, J. W.; Suo, Z., Mixed mode cracking in layered materials. *Advances in Applied Mechanics* **1992,** *29*, 63-191.

104. Ye, T.; Suo, Z.; Evans, A. G., Thin film cracking and the roles of substrate and interface. *Int. J. Sol. Struct.* **1992,** *29* (21), 2639-2648.

105. Beuth, J. L. J., Cracking of thin bonded films in residual tension. *Int. J. Sol. Struct.* **1992,** *29* (13), 1657-1675.

106. Michalske, T. A.; Bunker, B., Slow fracture model based on strained silicate structures. *Journal of Applied Physics* **1984,** *56* (10), 2686-2693.

107. Laarz, E.; Zhmud, B. V.; Bergström, L., Dissolution and deagglomeration of silicon nitride in aqueous medium. *Journal of the American Ceramic Society* **2000,** *83* (10), 2394-400.

108. Wiederhorn, S.; Bolz, L., Stress corrosion and static fatigue of glass. *Journal of the American Ceramic Society* **1970,** *53* (10), 543-548.

109. Rice, J., Thermodynamics of the quasi-static growth of Griffith cracks. *Journal of the Mechanics and Physics of Solids* **1978,** *26* (2), 61-78.

110. Lawn, B.; Wilshaw, T. R., *Fracture of brittle solids*. Cambridge university press: 1993.

111. Hillig, W., Surfaces, stress-dependent surface reactions and strength. *High strength materials* **1965**, 682-705.

112. Wiederhorn, S. M.; Freiman, S. W.; Fuller, E. R.; Simmons, C., Effects of water and other dielectrics on crack growth. *Journal of Materials Science* **1982,** *17* (12), 3460-3478.

113. Thouless, M., Crack spacing in brittle films on elastic substrates. *Journal of the American Ceramic Society* **1990,** *73* (7), 2144-2146.

114. Delannay, F.; Warren, P., On crack interaction and crack density in strain-induced cracking of brittle films on ductile substrates. *Acta metallurgica et materialia* **1991,** *39* (6), 1061-1072.

115. Kang, D.; Pikhitsa, P. V.; Choi, Y. W.; Lee, C.; Shin, S. S.; Piao, L.; Park, B.; Suh, K.-Y.; Kim, T.-i.; Choi, M., Ultrasensitive mechanical crack-based sensor inspired by the spider sensory system. *Nature* **2014,** *516* (7530), 222.

116. Wright, D. C., *Environmental stress cracking of plastics*. iSmithers Rapra Publishing: 1996.

117. Herrmann, C. F.; DelRio, F. W.; Miller, D. C.; George, S. M.; Bright, V. M.; Ebel, J. L.; Strawser, R. E.; Cortez, R.; Leedy, K. D., Alternative dielectric films for rf MEMS capacitive switches deposited using atomic layer deposited Al2O3/ZnO alloys. *Sensors and Actuators A: Physical* **2007,** *135* (1), 262-272.

118. Ylivaara, O. M.; Liu, X.; Kilpi, L.; Lyytinen, J.; Schneider, D.; Laitinen, M.; Julin, J.; Ali, S.; Sintonen, S.; Berdova, M., Aluminum oxide from trimethylaluminum and water by atomic layer deposition: The temperature dependence of residual stress, elastic modulus, hardness and adhesion. *Thin Solid Films* **2014,** *552*, 124-135.

119. Kim, N.; Potscavage, W.; Kippelen, B.; Yoo, S.; Domercq, B.; Graham, S. In *Fabrication and characterization of SiOx/Parylene and SiNx/Parylene thin film encapsulation layers*, ASME Electronic and Photonics Packaging Division, July 8, 2007 - July 12, 2007, Vancouver, BC, United states, American Society of Mechanical Engineers: Vancouver, BC, United states, 2007; pp 933-938.

120. Lee, J. Y.-M.; Sooriakumar, K.; Dange, M. M., The preparation, characterization and application of plasma-enhanced chemically vapour deposited silicon nitride films deposited at low temperatures. *Thin Solid Films* **1991,** *203* (2), 275-287.

121. Juang, C.; Chang, J.; Hwang, R., Properties of very low temperature plasma deposited silicon nitride films. *Journal of Vacuum Science & Technology B: Microelectronics and Nanometer Structures Processing, Measurement, and Phenomena* **1992,** *10* (3), 1221-1223.

122. Ingo, G.; Paparazzo, E.; Bagnarelli, O.; Zacchetti, N., XPS studies on cerium, zirconium and yttrium valence states in plasma-sprayed coatings. *Surface and Interface Analysis* **1990,** *16* (1-12), 515-519.

123. Smith, D. L.; Alimonda, A. S.; Chen, C. C.; Ready, S. E.; Wacker, B., Mechanism of SiN x H y Deposition from NH 3-SiH4 Plasma. *Journal of the Electrochemical Society* **1990,** *137* (2), 614-623.

124. Xu, W.; Zhao, J.; Qian, L.; Han, X.; Wu, L.; Wu, W.; Song, M.; Zhou, L.; Su, W.; Wang, C.; Nie, S.; Cui, Z., Sorting of large-diameter semiconducting carbon nanotube and printed flexible driving circuit for organic light emitting diode (OLED). *Nanoscale* **2014,** *6* (3), 1589-1595.

125. Tong, J.; Xiong, S.; Zhou, Y.; Mao, L.; Min, X.; Li, Z.; Jiang, F.; Meng, W.; Qin, F.; Liu, T.; Ge, R.; Fuentes-Hernandez, C.; Kippelen, B.; Zhou, Y., Flexible all-solution-processed all-plastic multijunction solar cells for powering electronic devices. *Materials Horizons* **2016,** *3* (5), 452-459.

126. Docampo, P.; Ball, J. M.; Darwich, M.; Eperon, G. E.; Snaith, H. J., Efficient organometal trihalide perovskite planar-heterojunction solar cells on flexible polymer substrates. *Nat Commun* **2013,** *4*.

127. Yi, H. T.; Payne, M. M.; Anthony, J. E.; Podzorov, V., Ultra-flexible solution-processed organic field-effect transistors. *Nature Communications* **2012,** *3*, 1259.

128. Lee, S.; Seong, H.; Im, S. G.; Moon, H.; Yoo, S., Organic flash memory on various flexible substrates for foldable and disposable electronics. *Nature Communications* **2017,** *8* (1), 725.

129. Khan, Y.; Ostfeld, A. E.; Lochner, C. M.; Pierre, A.; Arias, A. C., Monitoring of Vital Signs with Flexible and Wearable Medical Devices. *Adv. Mater.* **2016,** *28* (22), 4373-4395.

130. Baumert, E.; Pierron, O., Fatigue properties of atomic-layer-deposited alumina ultra-barriers and their implications for the reliability of flexible organic electronics. *Applied Physics Letters* **2012,** *101* (25), 251901.

131. Ok, K.-H.; Kim, J.; Park, S.-R.; Kim, Y.; Lee, C.-J.; Hong, S.-J.; Kwak, M.-G.; Kim, N.; Han, C. J.; Kim, J.-W., Ultra-thin and smooth transparent electrode for flexible and leakage-free organic light-emitting diodes. *Scientific reports* **2015,** *5*, 9464.

132. Hwang, D. K.; Fuentes-Hernandez, C.; Fenoll, M.; Yun, M.; Park, J.; Shim, J. W.; Knauer, K.; Dindar, A.; Kim, H.; Kim, Y., Systematic Reliability Study of Top-Gate p-and n-channel Organic Field-Effect Transistors. *ACS Appl. Mater. Inter.* **2014,** *6* (5), 3378-3386.

133. Carcia, P.; McLean, R.; Groner, M.; Dameron, A.; George, S., Gas diffusion ultrabarriers on polymer substrates using Al 2 O 3 atomic layer deposition and SiN plasma-enhanced chemical vapor deposition. *Journal of Applied Physics* **2009,** *106* (2), 023533.

134. Jia, X.; Fuentes-Hernandez, C.; Wang, C.-Y.; Park, Y.; Kippelen, B., Stable organic thin-film transistors. *Science Advances* **2018,** *4* (1), eaao1705.

135. Kim, K.; Luo, H.; Zhu, T.; Pierron, O. N.; Graham, S., Influence of Polymer Substrate Damage on the Time Dependent Cracking of SiN x Barrier Films. *Scientific reports* **2018,** *8* (1), 4560.

136. Fong, N. R.; Berini, P.; Tait, R. N., Mechanical properties of thin free-standing CYTOP membranes. *Journal of Microelectromechanical Systems* **2010,** *19* (3), 700-705.